Design, Fabrication, Modeling, and Optimization of Origami-inspired Soft Pneumatic Actuators

Design, Fabrication, Modeling, and Optimization of Origami-inspired Soft Pneumatic Actuators

By

Abdelrahman Zaghloul, B.Sc., M.Sc.

A Thesis

Submitted to the School of Graduate Studies

In Partial Fulfillment of the Requirements

For the Degree

Doctor of Philosophy

McMaster University

February 2021

Doctor of Philosophy (2021)

McMaster University

(Mechanical Engineering)

Hamilton, Ontario

TITLE: Design, Fabrication, Modeling, and Optimization of Origami-inspired Soft Pneumatic Actuators

AUTHOR: Abdelrahman Zaghloul, B.Sc., M.Sc.

SUPERVISOR: Dr. Gary M. Bone, Professor

NUMBER OF PAGES: xviii, 98

Lay Abstract

Soft pneumatic actuators are lighter than conventional rigid pneumatic actuators and are safer for applications involving physical contact with users or fragile objects. The design, modelling, fabrication, and optimization of origami-inspired soft pneumatic actuators (OSPA) are investigated. A novel fabrication method that is rapid, cost-effective, and more systematic than prior OSPA fabrication methods is proposed. A nonlinear model is developed and shown to predict the OSPA's output force with a 5.7% maximum error. An extensive series of tests are performed on OSPA prototypes. The accordion pattern OSPA can lift more than 124 times its own weight, and had no decrease in performance after 150,000 contraction/extension cycles with a payload of 2 kg. This durability is superior to existing OSPA. Lastly, a model-based approach for optimizing the OSPA design is presented and validated experimentally. The proposed fabrication, modelling and optimization approaches can be easily adapted to other OSPA designs.

Abstract

Soft pneumatic actuators produce more energy output per unit mass than conventional rigid pneumatic actuators and are safer for applications involving physical contact with users or fragile objects. The design, modelling, fabrication, and optimization of origami-inspired soft pneumatic actuators (OSPA) are investigated in this thesis. A novel fabrication method employing heat shrinkable polymers conforming to reusable 3D printed molds is proposed. It is rapid, cost-effective, and more systematic than prior OSPA fabrication methods. A nonlinear finite-element analysis (FEA) model for an OSPA based on the accordion crease pattern is developed for predicting the actuator's folding behavior and blocked force. The model includes a nonlinear hyperelastic model of the heat shrink material’s behaviour (obtained empirically) and nonlinear frictional contacts. It is validated with experimental results and is shown to predict the blocked force with a 5.7% maximum error. Prototypes of two OSPA designs (accordion and Yoshimura patterns) are fabricated. Isometric, isobaric, isotonic, and cyclic fatigue tests are performed on the accordion pattern OSPA. The tests demonstrate that it can lift more than 124 times its own weight, and had no decrease in performance after 150,000 contraction/extension cycles with a payload of 2 kg. This durability is superior to existing OSPA. Lastly, a FEA model-based design optimization approach is proposed. A multi-objective genetic algorithm (MOGA) is used to find the origami design parameters that maximize the accordion pattern OSPA's work output. The optimized design is validated experimentally. Although this research focuses on the accordion pattern OSPA, the proposed fabrication, modelling and optimization approaches can be easily adapted to other OSPA designs. In addition to linear force and motion, these actuators can be combined to produce different motions, e.g., a pair of actuators can be connected by a cable to a pulley in an agonist-antagonist arrangement to produce a bidirectional rotary actuator.

Acknowledgment

My sincere gratitude goes to my supervisor Prof. Gary M. Bone, for his continuous support, his patience, encouragement, and guidance throughout the course of my PhD. Dr. Bone selflessly and patiently helped me in many different ways. My graduate studies have allowed me to learn a lot and gain skills across a wide variety of topics.

Special thanks are due to my supervisory committee members, Dr. P. Ravi Selvaganapathy and Dr. Cheryl Quenneville, for their valuable comments and suggestions.

I am thankful for the help and support provided by the wonderful technical staff in the Mechanical Engineering Machine Shop, specifically Michael Lee and Mark Mackenzie. I would like to thank Thode Library Makerspace staff for giving me the chance to get more experience with 3D printing that helped me much during my research.

My gratitude extends to all my friends and colleagues whom I met during my journey at McMaster University for their moral supports and helpful discussions.

At last, but by no means the least, I want to give a big thank you from the bottom of my heart to my parents, my lovely wife, my kids, and my sisters for their love, spiritual support, and prayers as I completed this research.

Contents

Lay Abstract ……………………………………………………………………..iv

Abstract………………………………………………………………………………v

Acknowledgment……………………………………………………………………vi

Contents……………………………………………………………………………..vii

List of Figures……………………………………………………………………….xii

List of Tables………………………………………………………………………..xvi

Abbreviations………………………………………………………………………xvii

Nomenclature………………………………………………………………………xviii

Chapter 1. Introduction……………………………………………………….....1

1.1 Preface 1

1.2 Objective and Organization 3

Chapter 2. Literature review………………………………………………………5

2.1 Introduction 5

2.2 A Design of Origami-Inspired Actuators 5

2.3 Fabrication Methods for OSPA.. 6

  2.3.1 Elastomer casting 6

  2.3.2 Folding and gluing/taping.. 8

  2.3.3 3D printing 10

2.4 Modelling of Origami-inspired Soft Pneumatic Actuators 13

2.5 Design Optimization of Soft Pneumatic Actuators....................... 15

2.6 Conclusions.. 17

Chapter 3 Novel fabrication method for OSPA……………………………………18
3.1 Introduction 18
3.2 Actuator and Mold Design 18
    3.2.1 Actuator geometry 20
    3.2.2 Mold design 22
    3.2.3 Design of end caps and support ribs 24
    3.2.4 Heat-shrink material selection... 25
3.3 Fabrication Method 27
3.4 Design and Fabrication of OSPA Prototypes for Testing 29
3.5 Soft-ended Actuator 31
3.6 Modified Fabrication Method for Creating Small-diameter Actuators 32
3.7 Conclusion 35
Chapter 4. Modeling, simulation, and validation of OSPA using FEA……………37
4.1 Introduction 37
4.2 Material Modeling 37
    4.2.1 Introduction 37
    4.2.2 Tensile testing... 38
    4.2.3 Hyperelastic material model... 41
4.3 Importing the CAD model and Selecting Suitable Mesh Settings 42
4.4 Contact definitions.. 45
4.5 FEA modelling for prediction of deformation and blocked force 45
4.6 Validation of the FEA model. 50
4.7 Conclusions... 53

Chapter 5. Experimental testing and OSPA characterization……………………..54

5.1 Introduction 54

5.2 Hardware and software development.. 54

5.3. Isometric and isobaric testing 59

5.3.1 Blocked force measurement of accordion pattern OSPA.................. 59

5.3.2 Blocked force measurement of Yoshimura pattern OSPA 60

5.4 Isotonic testing 62

5.5 Hysteresis 64

5.6 Fatigue testing... 65

5.7 Consistency testing 66

5.8 Scalability 68

5.9 Comparison of the OSPA Prototypes with Related Pneumatic Actuators 69

5.10 Conclusions.. 73

Chapter 6. Design Optimization and Validation of Accordion OSPA……………..75

6.1 Introduction 75

6.2 Optimization Workflow.. 75

6.3 Accordion Pattern Geometric Parameters and Constraints......................... 76

6.4 Two-part FEA Simulation Procedure 78

6.5 Optimization 79

6.5.1 Optimization problem definition.. 79

6.5.2 Optimization details 80

6.6 Optimization Result Verification and Validation.. 84

6.7 Conclusions.. 86

Chapter 7. Conclusions……………………………………………………………..88

7.1 Summary 88

7.2 Achievements 89

7.3 Actuator limitations 92

7.4 Recommendations for future work 92

References………………………………………………………………………...94

List of Figures

Figure 2.1 The essential elements of an origami crease pattern. (a) 2D accordion crease pattern [5]. (b) An accordion pattern in its folded and glued/taped state. .. 6

Figure 2.2 Origami patterns (left) that can be used to create cylindrical shapes (right). (a) Accordion pattern [6]**.** (b) Kresling pattern [6]. (c) Miura pattern [7]. (d) Yoshimura pattern [8]. (e) Tachi-Miura pattern [6]. (f) Miura-ori pattern [9].......... 7

Figure 2.3 (a) The fabrication steps for an OSPA based on paper-elastomer composites. (b) An origami actuator fabricated with this method extended under the effect of two different pressures [1]. 8

Figure 2.4 The fabrication steps for assembling a soft bending module with origami paper shell [10]. 9

Figure 2.5 Fabrication steps for the vacuum-powered origami-inspired actuator vacuum from [11]. 9

Figure 2.6 Actuator design and fabrication proposed in [12]. Upper left: Principle of operation. Lower left: Three sizes of actuator prototypes. Right: Fabrication steps. 11

Figure 2.7 OSPA fabricated by 3D printing in [3]. (a) Extension type actuator made by SLS. (b) Contraction type actuator made by FDM. 11

Figure 2.8 A prototype of origami-inspired flexible pneumatic actuator manufactured using multi-material 3D printing [14]. 12

Figure 2.9 (a) Exploded view of the rotary OSPA design. (b) Prototype made from 3D printed TPU and other materials [15]. 13

Figure 3.1 Designs for OSPA using different patterns. (a) Accordion pattern. (b) Yoshimura pattern. 19

Figure 3.2 First design OSPA with no internal support. (a) The unpressurized OSPA with a 3.3 kg payload attached. (b) Instead of contracting and lifting the payload, the OSPA collapsed when a vacuum pressure was applied. 20

Figure 3.3 The geometric parameters of an OSPA based on accordion pattern (a) Top sectional view. (b) Isometric view. 21

Figure 3.4 Removal steps for the seven-piece accordion pattern mold. (a) CAD model of the assembled mold. (b) Remove the middle part first. (c) Push the two yellow side pieces together, then pull them out. (d) Remove the four green side pieces by sliding and pulling one at a time. 23

Figure 3.5 Removal steps for the seven-piece Yoshimura pattern mold. (a) CAD model of the assembled mold. (b) Remove the middle part first. (c) Slide each blue side piece over, then pull it out. (d) Remove the four red and green side pieces by sliding and pulling one at a time. 23

Figure 3.6 End cap designs. (a) Top end cap for accordion pattern OSPA. (b) Top end cap for Yoshimura pattern OSPA. (c) Bottom end cap design that is not pattern specific.. 24

Figure 3.7 Designs for the internal support ribs. (a) For accordion pattern OSPA. (b) For Yoshimura pattern OSPA... 25

Figure 3.8 The OSPA fabrication method. 29

Figure 3.9 The accordion pattern OSPA used for testing. (a) Isometric view. (b) Two fabricated prototypes.. 30

Figure 3.10 Soft-ended OSPA prototype. (a) Contracted using a pressure of -55 kPa. (b) Extended using a pressure of 160 kPa. The soft end can be seen pressing against the rigid metal surface on the right. 32

Figure 3.11 3D CAD models of the modified mold, support ribs and end caps. (a) Stacked PVA mold with ABS support ribs. The PVA half-height units are shown in gray, and ABS parts show are shown in green, red and blue. (b) The PVA half-height units. (c) ABS support rib. (d) Modified top end cap. (e) Bottom end cap. 33

Figure 3.12 (a) Dissolvable PVA mold parts and support ribs. (b) A two-bellow accordion actuator fabricated with the modified method. 35

Figure 4.1 Dimensions of uniaxial tensile test dumbbell-shaped specimen (all units in mm) [26].. 39

Figure 4.2 Steps to prepare a dumbbell-shaped specimen from the fully shrunk heat-shrink.. 39

Figure 4.3 (a) Dumbbell test specimens cut from unshrunk polyolefin heat shrink. (b) Dumbbell test specimens cut from fully shrunk polyolefin heat shrink. (c) The specimens were stretched using a Shimadzu tensile test machine with a loading rate of 500 mm/min. 40

Figure 4.4 Averaged stress-strain curves obtained from the tensile tests for ten dumbbell-shaped specimens (five unshrunk and five fully shrunk). The standard errors are indicated by the shaded areas. 41

Figure 4.5 Modified CAD model used for FEA simulation. (a) Bottom end cap without the sawtooth grooves. (b) Top end cap without the sawtooth grooves and air inlet hole. (c) Simplified support rib. 42

Figure 4.6 (a) The imported full 3D CAD model. (b) Quarter symmetry CAD model. 43

Figure 4.7 Two element types were used to mesh the model. Tetrahedral elements with ten nodes (SOLID187) were used for the end caps and support ribs. Shell elements (SHELL181) for the OSPA accordion pattern walls. 44

Figure 4.8 Contact definition between the different parts of the accordion pattern OSPA. (a) Bonded contact between the top end cap and the accordion pattern wall. (b) Frictional contact between the outer surfaces of the wall. (c) Frictional contact between two successive support ribs. (d) Frictional contact between the inner surfaces of the wall. (e) Bonded contact between the bottom end cap and the accordion pattern wall. (f) Frictional contact between the wall inner surface and the top and bottom surfaces of a support rib. 46

Figure 4.9 The boundary conditions for FEA of accordion pattern OSPA to predict the deformation are fixed support of the bottom end cap and a loading condition as negative pressure normal to the internal walls. 47

Figure 4.10 The deformed (folded) model of OSPA under the effect of internal vacuum pressure. 47

Figure 4.11 Predicted stress and strain distributions due to folding. (a) von Mises equivalent stress in Pa. (b) von Mises equivalent strain. 48

Figure 4.12 Predicted stress and strain distributions due to the blocked force with an internal pressure of -40 kPa. (a) von Mises equivalent strain. (b) von Mises equivalent stress in Pa. 49

Figure 4.13 The white arrow shows the direction of the blocked force generated by the OSPA under the effect of internal vacuum pressure. 49

Figure 4.14 The boundary conditions for the two-step FEA simulation. (a) First step boundary conditions fixed support of the bottom end cap and a fixed displacement of the top end cap. (b) Second step boundary conditions fixed support of the bottom end cap, fixed displacement of the top end cap and loading condition as negative pressure normal to the internal walls. 51

Figure 4.15 Comparison of the partially folded shapes of the accordion pattern OSPA. (a) FEA prediction. (b) Experimental result. 52

Figure 4.16 Comparison of the blocked forces predicted by FEA to the experimental results for displacements of 0, 20 and 40 mm. 52

Figure 5.1 Measurement setup built for the isometric and isobaric testing. (a) Schematic (b) CAD model. 55

Figure 5.2 Measurement setup built for the isometric and isobaric testing. (a) CAD model. (b) the actual measurement setup. 56

Figure 5.3 CAD model of the measurement setup built for the isotonic contraction and cyclic fatigue testing. 58

Figure 5.4 Experimental results for the accordion pattern OSPA.(a) Isometric plots of force vs. pressure. (b) Isobaric plots of force vs. displacement. 60

Figure 5.5 (a) Main geometric parameters of the Yoshimura pattern OSPA design. (b) Yoshimura pattern OSPA prototype used for testing. 61

Figure 5.6 Experimental results for the Yoshimura pattern OSPA. (a) Isometric plots of force vs. pressure. (b) Isobaric plots of force vs. displacement. 62

Figure 5.7 (a) Isotonic contraction of the accordion pattern OSPA with a payload of 2 kg. (b) Isotonic contraction with a payload of 8.6 kg. 63

Figure 5.8. Isotonic contraction test results for the accordion pattern OSPA. (a) Contraction ratio vs. pressure for upwards motions with payloads of 2.0, 3.3, 4.0, 5.3, 6.5, 7.7 and 8.6 kg. 64

Figure 5.9 Contraction ratio vs. pressure for upwards and downwards motions with 2.0, 5.3 and 8.6 kg payloads, demonstrating the actuator's hysteresis.............. 65

Figure 5.10 Results from the vertical cyclic fatigue test with 2 kg payload. Pressure and displacement vs. time for the first and last 5 cycles of the 150,000 cycles test. 66

Figure 5.11 The accordion pattern OSPA used for testing. Two fabricated prototypes. 67

Figure 5.12. Blocked force vs. pressure results obtained from isometric tests performed with the 2nd prototype of the accordion pattern OSPA. 67

Figure 5.13 Accordion pattern OSPAs scaled fabricated from different diameter heat-shrink tubing. 68

Figure 5.14 Testing the D = 101.6 mm accordion pattern OSPA lifting different payloads. 69

Figure 6.1 The effect of increasing the d_{ratio} value beyond 2.4. (a) Actual actuator with $d_{ratio} > 2.4$. (b) FEA simulation for the same case. 78

Figure 6.2 Two-part FEA workflow. 79

Figure 6.3 The effect of varying the actuator thickness on the output work while the other variables are fixed at the optimum point. Note: The vertical axis shows ¼ of the work due to the quarter symmetry model used with the FEA.................... 83

Figure 6.4 The effect of varying the actuator diameter ratio on the output work while the other variables are fixed at the optimum point. Note: The vertical axis shows ¼ of the work due to the quarter symmetry model used with the FEA..... 83

Figure 6.5 The effect of varying actuator folding angle on the output work while the other variables are fixed at the optimum point. Note: The vertical axis shows ¼ of the work due to the quarter symmetry model used with the FEA....................... 84

List of Tables

Table 3.1 Commercial heat-shrink tubing candidates for OSPA[1] 27

Table 5.1 Comparison of the OSPA with related pneumatic actuators in terms of performance metrics and cost. 72

Table 6.1 The selected 3D CAD parameters of the accordion actuator and their ranges.. 77

Table 6.2 Design points generated by the LHS DOE and the corresponding maximum strain and ¼ work values computed by the FEA simulation procedure. 82

Table 6.3 Output work values generated from FEA simulation and experimental testing of the three-unit accordion pattern OSPAs... 86

Abbreviations

ABS: Acrylonitrile butadiene styrene

ASTM: American society for testing and materials

CAD: Computer-aided design

DAQ: Data Acquisition System

DOE: Design of experiment

FDM: Fused deposition modeling

FEA: Finite element analysis

LHS: Latin Hypercube Sampling

MOGA: Multi-objective Genetic Algorithm

OSPA: Origami semi-soft pneumatic actuator

PLA: Polylactic acid

PVA: Polyvinyl alcohol

RS: Response surface

SLS: Selective laser sintering

TPU: Thermoplastic polyurethane

WTV: Work to mass

WTM: Work to volume

Nomenclature

a : The longest side length (bases) of trapezoidal shape accordion base unit.

b : The side length (legs) of trapezoidal shape accordion base unit.

c : The shortest side length (bases)of trapezoidal shape accordion base unit.

C_{10}, C_{01} and D_1 : Hyperelastic material parameters.

d : The interior diameter.

D : The exterior diameter.

d_{ratio} : The ratio between the output and inner diameter.

F_{out} : The reaction force.

n :The number of units.

t : The actuator thickness.

W : The output work.

X_{opt} : Accordion base unit.

y_{out} : The actuator displacement.

α : The initial folding angle of the accordion pattern.

$\varepsilon_{vonMises}$: The von Mises strain.

Chapter 1. Introduction

1.1 Preface

Conventional robots are made from rigid materials such as aluminum and steel. Their links are connected by rotary joints that are driven by electric motors. Their precisely manufactured rigid components make them capable of performing very precise movements, but also makes them expensive. Furthermore, they require additional sensors and software in order to interact safely with people. This further adds to the cost and does not provide inherent safety if either the sensors or software fails. For example, the state-of-the-art JACO assistive arm by KINOVA [1] costs around $50K.

In contrast with the traditional approach to robot design, researchers have recently been focusing on developing robots with soft bodies. Their use of soft materials makes them inherently capable of interacting safely with humans. They can also be manufactured using inexpensive materials and equipment. Research on so-called “soft robots” has rapidly grown due to their potential to solve problems that cannot be easily solved by the traditional rigid robots. Although they are not suitable for applications requiring precise motion control, soft robots have applications in many areas, including: medicine [2], assistive devices [3][4], and exploring unstructured environments [5][6]. They also provide different ways to perform traditional robot functions, such as grasping [7] or locomotion [8][9].

Soft actuators are the main source of soft robots’ motion. Several actuation methods have been investigated for this type of actuator, including: tendon-driven [10], shape memory alloys [11], twisted-coiled actuators [12], electro-active polymers [13], hydraulic actuation [14] or pneumatic actuation [15]. Each of these actuation methods suffer from certain limitations. Tendon-driven systems are limited by tendon routing, and the use of electric motors that are rigid and relatively heavy. Electro-active polymers require voltages greater than 1kV. Shape memory alloys have limited strains which limit the actuator's range of motion. Twisted-coiled artificial muscle actuators have good strain and stress characteristics but have a slow response time since they are thermally activated. The major drawback of soft hydraulic actuators is the requirement for a hydraulic power source which tend to be large and bulky [16]. The power supply for a pneumatic actuator is simpler since no fluid reservoir or return lines are needed, and its components are much less expensive since the pressures used in pneumatics are much smaller than in hydraulics. Most soft actuators employed in soft robots, and elsewhere, are pneumatically powered as it can provide robust and compact actuators, with low inertia and low stiffness.

Origami is a Japanese art and science that guides the fabrication of 3D paper structures by folding flat sheets [17]. Origami has many desirable characteristics such as: low material volume and mass; scalability; reduced assembly; ease of miniaturization; and part number reduction [18]. As a result, there are many origami-inspired engineering applications ranging from large-scale deployable aerospace structures [19] to small-scale biomedical devices [20]; mechanical metamaterials [21]; and DNA machines [22]. In the field of soft robots, the integration of origami characteristics results in origami-inspired designs that have "built-in compliance because of the geometry of the folds and the creases in the material, and they are semi-soft, that is, they exhibit the properties of both rigid and soft robots" [23].

According to the source of motion, soft actuators may be classified into three main categories. The first category is fiber-reinforced pneumatic actuators e.g. McKibben muscles [24]. They use an elastic internal bladder and a braided fiber shell to generate contraction when the pressure is increased. Their main advantage is they generate a very large force. However, they suffer from the following limitations: short contractile stroke, nonlinear relationship between blocked force and stroke, and significant radial expansion [25]. Note that blocked force is defined as the force produced by an actuator when its length is constrained (i.e., isometric condition). The second category is bending actuators. These generate a bending motion when pressurized by constraining one side of the actuator (typically by changing the material thickness or using materials with different properties), e.g. PneuNets [26]. Unfortunately, this category of actuators suffers from the "ballooning effect," which may lead to rupturing due to material failure [27], or limit the application of this type of soft actuators due to volume limitations [28]. When the actuator consists of flat panels connected by compliant hinge joints, it belongs to the third category we will call “origami-inspired soft pneumatic actuators” (OSPA) [29]. OSPA possess the advantages of pneumatic actuators combined with the advantages of origami. This actuator category addresses the limitations of McKibben muscles and bending actuators by having constant cross-section during motion and a high contraction ratio; and eliminating the ballooning effect due to their natural folding behavior.

1.2 Objective and Organization

OSPA will be investigated in this research due to their desirable characteristics mentioned above, and their potential to be practical soft actuators suitable for real-life applications. This thesis explores the design, fabrication, modeling, and optimization of OSPA. The research objectives are to:

- Develop a novel, cost-effective, systematic, and consistent fabrication method for OSPA.
- Develop and validate an effective modeling and simulation method for OSPA.
- Optimize and validate the design of linear OSPA.

This thesis is organized into seven chapters, including this introductory chapter. Chapter 2 summarizes the most relevant literature in the areas of:

fabrication methods, modeling, simulation, and design optimization. Chapter 3 presents the actuator and mold design, a detailed explanation of the novel fabrication method, and a modified version of the fabrication method for creating small-diameter actuators. Chapter 4 describes the modelling of the OSPA's hyperelastic material, the development of a detailed finite element analysis (FEA) model of an OSPA based on the accordion crease pattern, and the validation of the model through experiments. Chapter 5 presents the experimental testing and characterization of the OSPA prototypes. Two test setups are designed and fabricated to measure the output force over a range of air pressures, the effect of the payload on the contraction ratio, and the service life through cyclic testing under load. After that, the ability of the fabrication method to produce actuators with consistent performance, and the method's scalability, are evaluated. Chapter 6 discusses the design optimization of the geometric parameters of an accordion pattern OSPA. The model-based optimization results are validated by testing an OSPA fabricated with the optimized parameters. Finally, in Chapter 7, the research conclusions and achievements are summarized, and suggestions are made for future work.

Chapter 2. Literature review

2.1 Introduction

The study of soft actuators is a very active research field. The most relevant publications related to soft pneumatic actuators, and OSPA in particular, will be reviewed in this chapter. Section 2.2 presents an overview of soft pneumatic actuators. Section 2.3 reviews the existing fabrication methods for OSPA. Section 2.4 discusses the relevant work related to the design optimization of OSPA. Finally, Section 2.5 concludes the chapter.

2.2 A Design of Origami-Inspired Actuators

An origami design is defined by its crease pattern. A crease is a fold which can either be convex (also called a “mountain fold”) or concave (also called a “valley fold”). The creases meet at vertices and are separated by flat panels. For example, the accordion crease pattern is illustrated in Figure 2.1a. After folding the creases and connecting the two axial sides of the pattern (by gluing or taping), the 3D folded accordion shape is generated as shown in Figure 2.1b.

Several origami patterns can be used to form a cylindrical shape, as shown in Figure 2.2. Some of these may be used to form an OSPA. The pattern's selection depends on many factors like the change in the internal cross-section during folding, the simplicity, application, and visibility of fabricating the pattern. The shapes made using the accordion and Yoshimura patterns maintain a constant cross-section during folding which makes sealing the ends easy. The Yoshimura paper was used for the OSPAs presented in [1] and [2]. The ends of the cylindrical shapes made from the Tachi–Miura and Miura-ori patterns change their internal cross-section during the folding process, making sealing the ends difficult. Even so, the Miura-ori pattern was used to create the OSPA in [3] and [4].

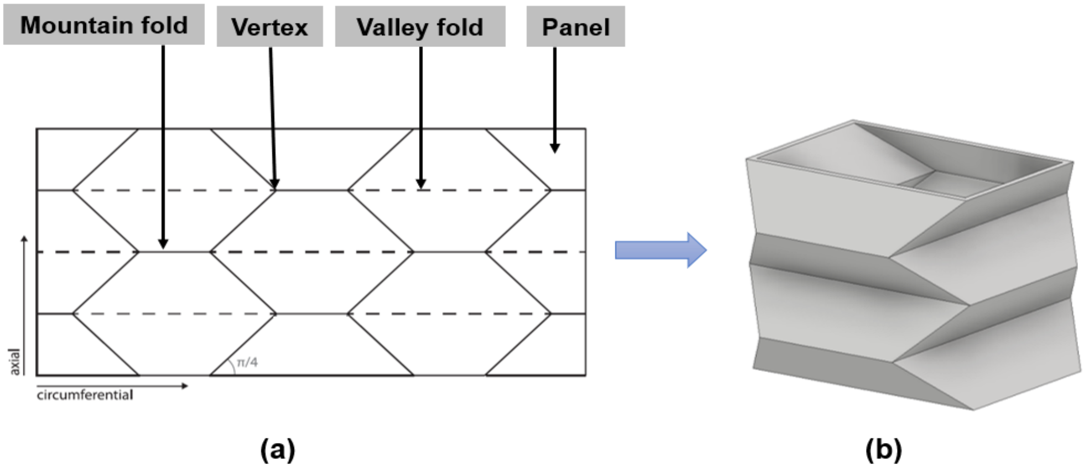

Figure 2.1 The essential elements of an origami crease pattern. (a) 2D accordion crease pattern [5]. (b) An accordion pattern in its folded and glued/taped state.

2.3 Fabrication Methods for OSPA

Fabrication methods for OSPA are very limited and have not fully matured. Only three distinct OSPA fabrication methods have been reported in the literature. These three methods are: elastomer casting, folding and gluing/taping, and 3D printing. These techniques will be illustrated in detail in the next sections.

2.3.1 Elastomer casting

Martinez et al. [1] was the first paper to fabricate OSPA by casting elastomer coated paper composites. The fabrication process steps are illustrated in Figure 2.3a. They fabricated several paper-elastomer OSPA prototypes, including an extension actuator based on the Yoshimura pattern, as illustrated in Figure 2.3b. The molds were made by 3D printing. Their method has also been adopted by other researchers in [2] and [4]. It is easy to use but is time-consuming due to the number of steps involved and the elastomer curing process. As with all pneumatic actuators, the output force of an OSPA is dependent on the operating pressure. The weakness of the paper-elastomer material limited the maximum operating pressures used in [1], [2], and [4] to 30, 20, and 10 kPa, respectively. Furthermore, in [1] only 50 unloaded pressurization/depressurization cycles were used to test the actuator for fatigue failure. No fatigue test results were reported in [2] or [4]. The fatigue life of this material is untested beyond 50 cycles.

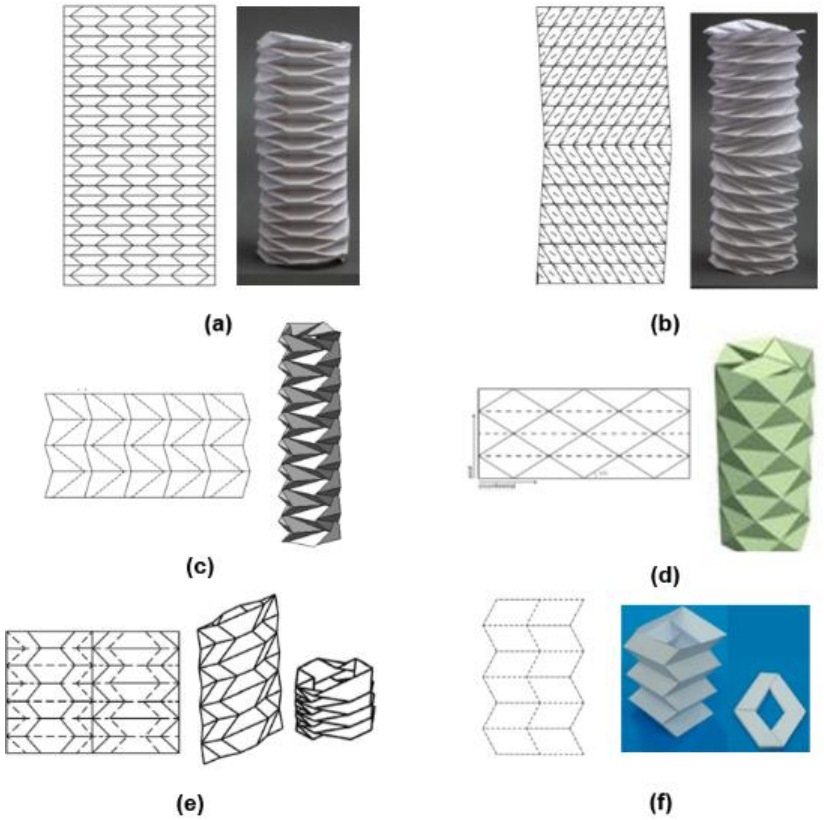

Figure 2.2 Origami patterns (left) that can be used to create cylindrical shapes (right). (a) Accordion pattern [6]**.** (b) Kresling pattern [6]. (c) Miura pattern [7]. (d) Yoshimura pattern [8]. (e) Tachi-Miura pattern [6]. (f) Miura-ori pattern [9].

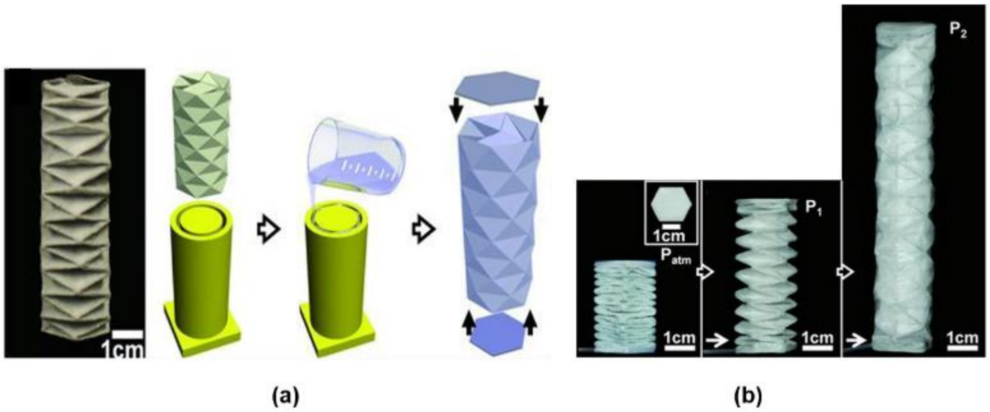

Figure 2.3 (a) The fabrication steps for an OSPA based on paper-elastomer composites. (b) An origami actuator fabricated with this method extended under the effect of two different pressures [1].

2.3.2 Folding and gluing/taping

Paez et al. [10] presented a novel soft pneumatic bending actuator enclosed by a origami shell made by folding and gluing paper using the accordion crease pattern as illustrated in Figure 2.4. With the aid of the origami shell, the actuator could sustain higher inflation pressures, deliver larger torques and generate the targeted motion trajectory. However, the sliding friction and wear between the internal bending actuator and the outer shell will reduces the actuator’s efficiency and shorten its service life. They did not test the actuator's service life beyond 1,000 unloaded contraction/extension cycles.

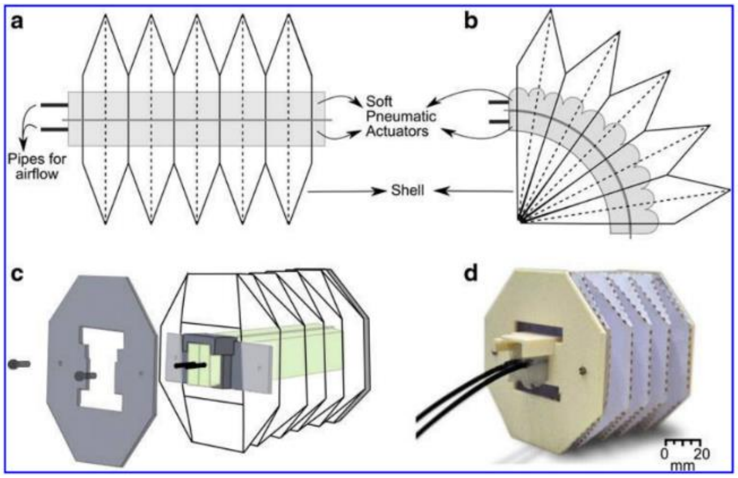

Figure 2.4 The fabrication steps for assembling a soft bending module with origami paper shell [10].

Lee et al. [11] proposed a novel vacuum-powered origami-inspired actuator. source. Their method uses a folded sheet of polyvinyl chloride that is wrapped around rigid, triangular, evenly spaced, transversal reinforcements, and top and bottom endplates. The fabrication is mostly done manually as shown in Figure 2.5. When vacuum pressure is applied the reinforcements control the collapse of the sheet which leads to the actuator contracting. The sheet and other components are held together using tape. They included tests with a vacuum pressure of -83 kPa. This method is limited to one origami pattern, and it is likely that the tape would start failing after a small number of cycles. No fatigue test results were included.

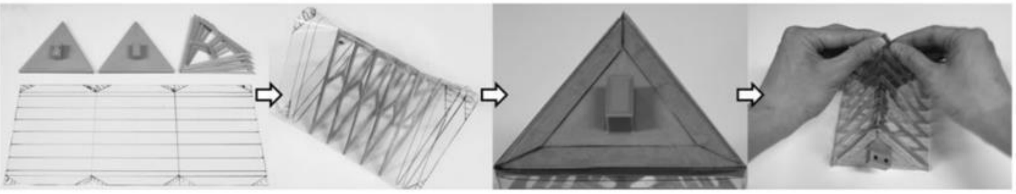

Figure 2.5 Fabrication steps for the vacuum-powered origami-inspired actuator vacuum from [11].

2.3.3 3D printing

Li et al. [12] proposed another design for a soft pneumatic actuator where parts of the actuator were 3D printed. Their design was inspired by the cold gas-pressure folding idea presented in [13]. The actuator consists of a compressible skeleton (which may, or may not, be origami-inspired) enclosed by an airtight flexible skin. The application of vacuum pressure causes the actuator to contract. The principle of operation, fabrication steps and three actuator prototypes are shown in Figure 2.6. The skeletons were 3D printed from various polymers. Failure by buckling of the skeleton, or by the sliding friction and wear that occurs between the skeleton and skin, are the main disadvantages of this design. The service life of a linear actuator with a nylon “zigzag” skeleton and skin made from nylon fabric was tested in the vertical plane with a 1 kg load. The actuator completed 30,000 vacuum pressurization/depressurization cycles without failing.

Sane et al. [3] designed two actuators, one for extension and one for contraction, based on the Muira-ori crease pattern. Each actuator was entirely made by 3D printing. The extension actuator was made of polyether block amide on a selective laser sintering (SLS) machine, while the contraction actuator was made of thermoplastic polyurethane (TPU) on a fused deposition modeling (FDM) printer. Their actuators are shown in Figure 2.7. Their results suggest that the actuators were not very strong. The middle picture in Figure 2.7b shows that the fabricated panels of the contraction actuator were significantly bent at a pressure of only 17 kPa, and they used a maximum pressure of only 34.5 kPa with both actuators. Finally, they did not perform any fatigue tests on the actuators.

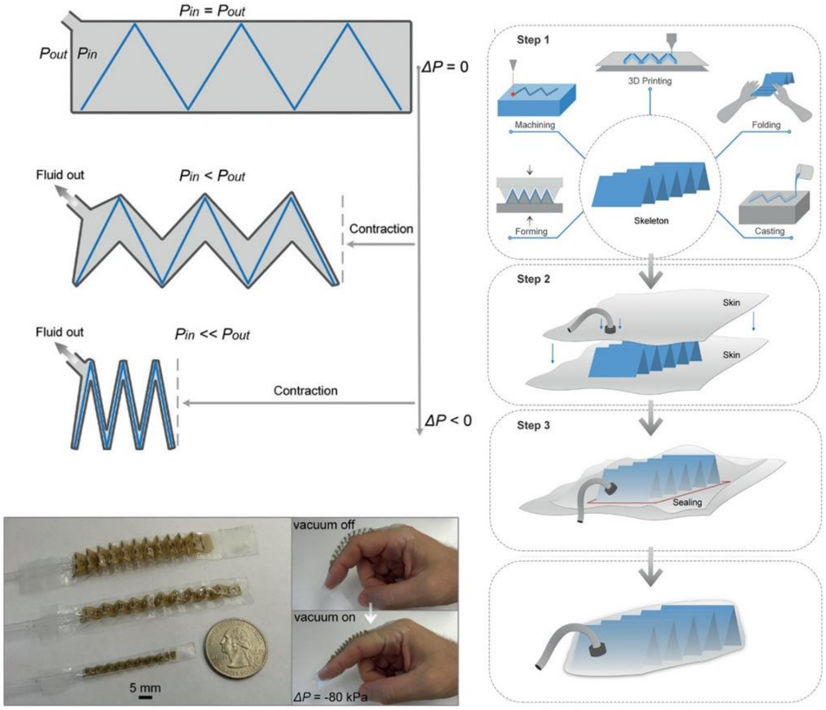

Figure 2.6 Actuator design and fabrication proposed in [12]. Upper left: Principle of operation. Lower left: Three sizes of actuator prototypes. Right: Fabrication steps.

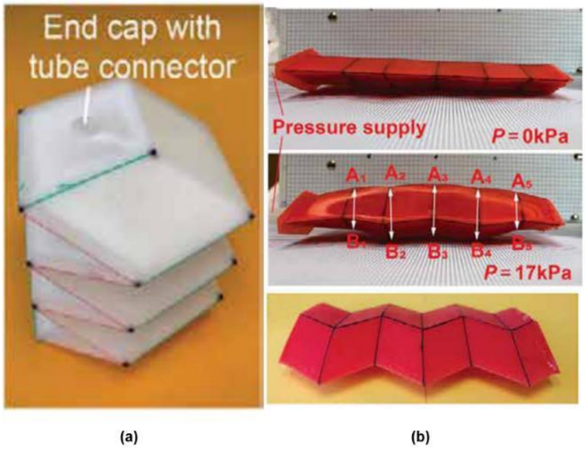

Figure 2.7 OSPA fabricated by 3D printing in [3]. (a) Extension type actuator made by SLS. (b) Contraction type actuator made by FDM.

Multi-material 3D printing has also been used to produce OSPA. Schmitt et al. [14] proposed a new OSPA design that can produce high forces over short displacements. They manufactured two prototypes using a Stratasys Connex 350 SLS multi-material printer. The hinges were printed using a “rubber-like” elastomer (TangoBlackplus FLX 980) while the panels were printed using a rigid polymer (VeroWhiteplus RGD 835) as illustrated in Figure 2.8. The best prototype produced a force of 40 N at a pressure of 24.5 kPa. No tests were performed at higher pressures. The prototype failed after 30 cycles during an unloaded cyclic pressurization/depressurization test. Another disadvantage of this work is the requirement to use an expensive 3D printer.

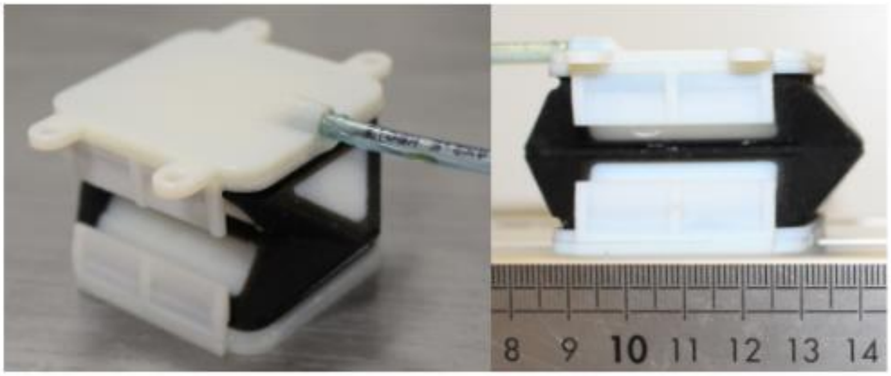

Figure 2.8 A prototype of origami-inspired flexible pneumatic actuator manufactured using multi-material 3D printing [14].

Yi et al. [15] presented the design, modelling and testing of a 3D printed OSPA for rotary motion. The pneumatic chambers were fabricated from flexible TPU using a delta type FDM 3D printer as illustrated in Figure 2.9. The wall thickness was selected to be 1.3 mm to minimize leakage. The paper does not describe the challenges involved in removing the inner supporting material and this materials effect on the actuator's performance, even though this issue has been reported in other research using the same fabrication method [16]. The results of a 10,000 cycle unloaded fatigue test (with a 1 Hz, 17 degree amplitude, sinusoidal trajectory) show only minor changes in the output response.

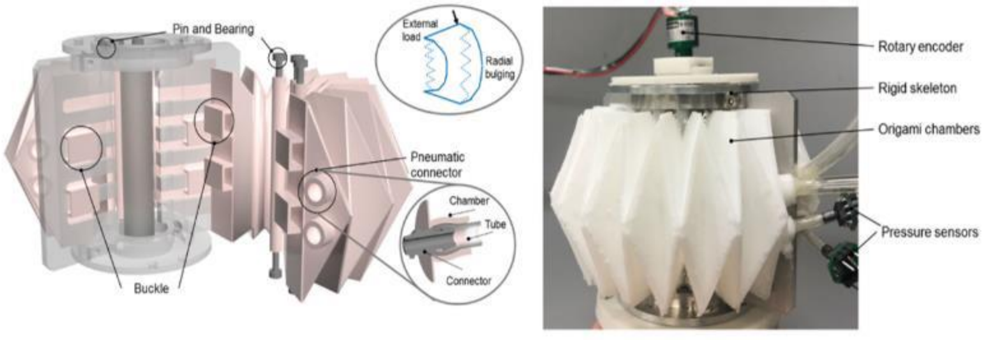

(a) (b)

Figure 2.9 (a) Exploded view of the rotary OSPA design. (b) Prototype made from 3D printed TPU and other materials [15].

2.4 Modelling of Origami-inspired Soft Pneumatic Actuators

The physics of origami structures is often characterised by the nonlinear coupling of the folding of the hinges and the deformations of the panels. In order to characterize the structural behavior of origami, many methods have been developed that may be grouped into three main categories [17]: (1) Analytical solutions which are obtained empirically by studying the behavior of a small part of the pattern, (2) A bar and hinge method where panel in-plane deformations are restrained using bars elements while bending of panels and folds is modeled using rotational hinges, and (3) Numerical methods, particularly finite element analysis (FEA), where the system is discretized in a detailed fashion. The main limitation of the analytical methods from the 1st category is they are only suitable for a specific pattern and cannot be generalized to other origami patterns. The bar and hinge method (2nd category) can be generalized but is unrealistic. For example, it neglects the flexible panels' in-plane deformations. The FEA approach (3rd category) often provides the highest accuracy; however, it tends to be computationally expensive. In this section, we will review how these different methods have been used for modeling OSPAs.

Sane et al. [18], modelled the free stroke and blocked force performance of 3D printed OSPA using simplified analytical models and FEA. They developed simplified analytical models by assuming zero panel thickness and ideal end caps. Rigid-folding kinematics was then used to investigate the effect of end caps and material thickness on the actuator stroke length and pattern deformations. The blocked force was analyzed using an equivalent truss-frame model. They adopted a comprehensive nonlinear FEA simulation as their 2nd approach. The mechanical properties of the actuators' material were modelled by fitting tensile test results with a Mooney-Rivlin five parameter hyperelastic material model. Comparing the results of the two approaches demonstrates the FEA simulation's ability to capture the influence of the stiffness of thick panels and realistic end caps on the actuator's performance, which the analytical models could not capture.

Lee et al.[11] developed a quasistatic analytical model of their actuator based on the pouch motor model. Their model could reasonably predict the actuator's behaviour in most cases. However, the proposed model can work only for the specific material and the simplified triangular origami design used in this paper. Moreover, two different formulas were used to calculate the blocked force depending on the actuator's contraction ratio. This confirms the limitation of analytical models to only an actuator’s specific design and construction.

Yi et al. [15] presented a simplified analytical model of their rotary OSPA based on the kinematic equations relating the actuator's rotation angle to the geometric parameters of the origami pattern. The cylindrical shape was used to simplify the inflated origami chamber. The model considered the origami actuator's inherent stiffness, which depends on the chamber's material and the origami structure. The actuator's inherent stiffness was calibrated empirically, which again confirms the analytical models' limitations to a particular OSPA pattern and material.

2.5 Design Optimization of Soft Pneumatic Actuators

Design optimization is commonly used in the design of traditional actuators such as DC motors. The geometry must be optimized to get the best performance in terms of power, torque, efficiency, and/or size, etc. Even though the design optimization of soft pneumatic actuators is known to be important, it remains an underexplored topic in the literature [19].

Moseley et al. [20] was the first paper to present a model-based design optimization solution for soft pneumatic actuators belonging to the bending category (defined in Section 1.1). Their solution was based on an FEA model and used constrained optimization by linear approximation. A global optimization basin hopping algorithm was also implemented to find the new starting points for finding the global optimum. They implemented hyperelastic and viscoelastic material models of a soft silicone material. The effect of the number of chambers on displacement and the blocked force were studied. Two case studies were presented, and the optimization results were experimentally validated. The disadvantage of their solution is the computation time required. For example, solving the first case study required three days on a 16-core computer.

Runge et al. [21] presented a method for the design optimization of pneumatic soft bending actuators using a genetic algorithm. Their method combines FEA and gradient-free optimization. The objective was to minimize the radius of curvature and the ballooning effect of the pneumatic actuator. Comparing the initial and final designs, the actuator's achievable bending angle was significantly increased. At the same time, the amount of ballooning was kept low.

They first created a parametric 3D model in Abaqus of a soft robot module. They then optimized the model parameters using a genetic algorithm in Matlab. In each step of the optimization process, a nonlinear FEA model is created and simulated in ABAQUS. One of the proposed method's main weaknesses is that the FEA model must be run at each iteration, so the complexity of the FEA model will significantly affect the optimization time. Moreover, the validation of the optimization process through experimental testing was presented. Finally, the computational time took around 200 hours on a 16-core computer.

Dämmer et al.[22] presented a multi-material 3D printed pneumatic bellows actuator design strategy involving FEA-based shape optimization. The main optimization objective was strain minimization. The optimization routine was achieved by connecting Matlab and Abaqus using python scripts. A gradient-based Matlab optimization function with default settings was chosen to implement bounds and secondary constraints. They validated the optimization results through experimental testing. Unfortunately, they did not mention any details about the computing resource used for the optimization. Moreover, using gradient-based optimization algorithms cannot guarantee a globally optimum solution with highly nonlinear problems like this shape optimization.

The only design optimization research on OSPA was reported by Sane et al. [3]. As discussed in Section 2.3 and 2.4, they 3D printed a contraction OSPA from TPU and developed an FEA model of it using Ansys. The design optimization objectives were to maximize the actuator's normalized blocked force and free stroke while constraining the maximum stress predicted by FEA to be less than half of the ultimate tensile strength of TPU. They solved this multi-objective optimization problems using the non-dominated sorting genetic algorithm II included in the modeFRONTIER software package, Ansys and Matlab. They provided no information about the computing resources or time required to perform the optimization. They also did not validate the optimized design experimentally.

Finally, choosing one half of the ultimate tensile strength is risky since the actuator may fail at a lower stress due to plastic deformation.

2.6 Conclusions

Research on soft pneumatic actuators, and OSPA in particular, is still in its early phase and several challenges remain unaddressed. Regarding the fabrication methods, the elastomer casting technique suffers from the material's weakness (which limits the operating pressure) and has a long fabrication time due to the approximately 1 hour curing time of the elastomer. The folding and gluing/taping method relies on the user's manual dexterity so achieving repeatable results is difficult. Fabrication by 3D printing is more automated and repeatable, but has yet to produce a durable OSPA, and typically requires an expensive 3D printer. Regarding modelling of OSPA behaviour, the analytical solutions are only suitable for a specific pattern and cannot be generalized. The bar and hinge method can be generalized but is unrealistic. The FEA approach typically provides the highest accuracy but is computationally expensive. Finally, only one paper has appeared on OSPA design optimization. Unfortunately, the benefits of the proposed approach are unclear since the authors did not discuss the computational challenges or validate their optimization results experimentally.

Chapter 3 Novel fabrication method for OSPA

3.1 Introduction

As discussed in the previous chapter, the existing OSPA fabrication methods are either slow, rely on the user's manual dexterity (which makes achieving consistent results difficult) and/or have yet to produce a durable actuator. In this chapter, a novel fabrication method of OSPA is proposed that addresses these limitations. Our method uses commercially available heat-shrink tubing for the flexible section of the actuator. We thermally form the tubing around a rigid mold to create the folded origami-inspired shape. After the mold is removed, rigid support ribs are manually inserted, and end caps are attached by thermal forming to complete the actuator. In the following section, we present the main design parameters of the selected origami pattern, followed by a description of the actuator and mold design process. Next, the selection of the heat-shrink material is discussed. After that, the steps of the fabrication method are presented, followed by the fabrication of two prototypes and the fabrication of a soft-ended actuator. Finally, a modified fabrication method for creating small-diameter actuators is proposed and demonstrated by fabricating a prototype.

3.2 Actuator and Mold Design

Two of our designs for OSPA are shown in Figure 3.1. Each design consists of top and bottom end caps (shown in blue and orange, respectively), and the flexible origami-inspired section that will be made by thermal forming of heat-shrink tubing (shown in grey). We chose to fabricate OSPA based on the accordion and Yoshimura patterns since they can produce a larger stroke than other patterns [6] and their ends have constant cross-section so they can be easily attached to the end caps and simplify the sealing process.

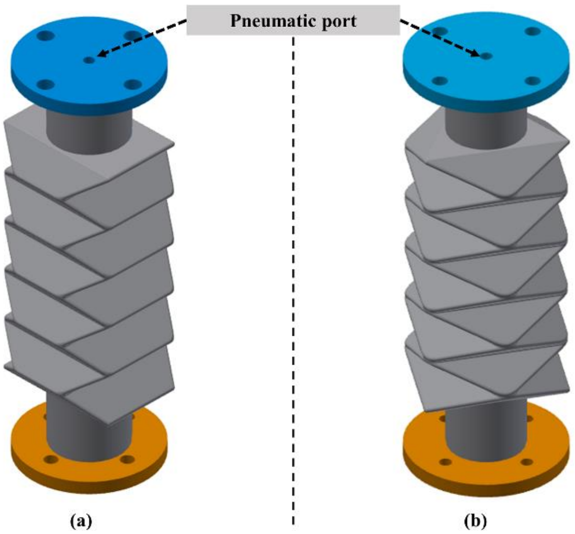

Figure 3.1 Designs for OSPA using different patterns. (a) Accordion pattern. (b) Yoshimura pattern.

After it was discovered that the initial prototypes collapsed when a vacuum pressure of only -15 kPa was applied during the isometric test. It also collapsed while trying to lift a 3.3 kg payload as shown in Figure 3.2. We added internal support ribs (not shown in Figure. 1) to strengthen the actuators. Another design approach for preventing the actuator walls from collapsing is to use heat-shrink tubing with thicker walls. We did not pursue this approach since thicker walls will increase the actuator's longitudinal stiffness. This has the disadvantages of reducing the actuator's force output (since more of the pneumatic pressure will be used to fold the hinges) and reducing its range of motion. Besides, the sealing process becomes so challenging with the increase of the thickness of the actuator. The geometric parameters of the actuator, the designs of the reusable molds, end caps, and support ribs will be presented in the proceeding subsections.

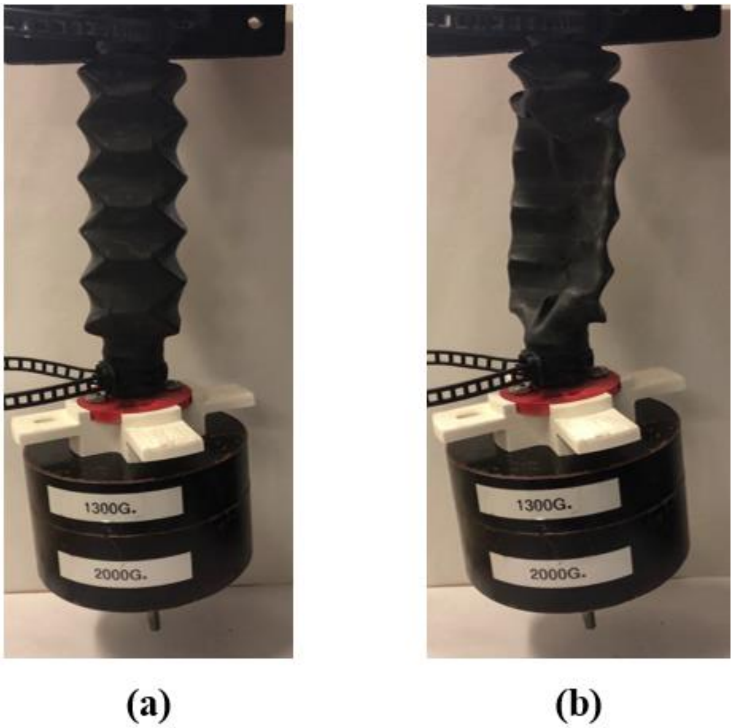

Figure 3.2 First design OSPA with no internal support. (a) The unpressurized OSPA with a 3.3 kg payload attached. (b) Instead of contracting and lifting the payload, the OSPA collapsed when a vacuum pressure was applied.

3.2.1 Actuator geometry

The performance of the OSPA is dependent on the geometric parameters of the origami pattern selected for the actuator. We will focus on the accordion pattern since the equations for its geometry are well known. The basic geometry of the accordion origami pattern consists of a set of repeated base polygons arranged in an alternating pattern to form repeated units; each unit includes eight polygons. The base unit of the accordion pattern has the shape of a trapezoid with side lengths a, b, and c as shown in Figure 3.3a. Equations (3.1) - (3.4) from [1] are used to define the relationships between the accordion base unit parameters. The trapezoidal unit parameters are written in terms the inner and outer diameters of two circles enclosing the actuator in the folded state as shown in Figure 3.3b.

$$\varphi = 45° \tag{3.1}$$

$$a = \sqrt{D^2 - d^2} \tag{3.2}$$

$$b = D\,sin\left(sin^{-1}\left(\frac{a}{D}\right) - \varphi\right) \tag{3.3}$$

$$c = a - 2b\,cos\,(\varphi) \tag{3.4}$$

Where: d is the interior diameter and D is the exterior diameter

Moreover, the effect of different parameters on the performance of the accordion-based OSPA, including: the number of units n, the initial folding angle of the accordion pattern α, the actuator thickness t, and the ratio between outer and the inner diameter diameters $d_{ratio} = D/d$ will be studied in detail and optimized in Chapter 6.

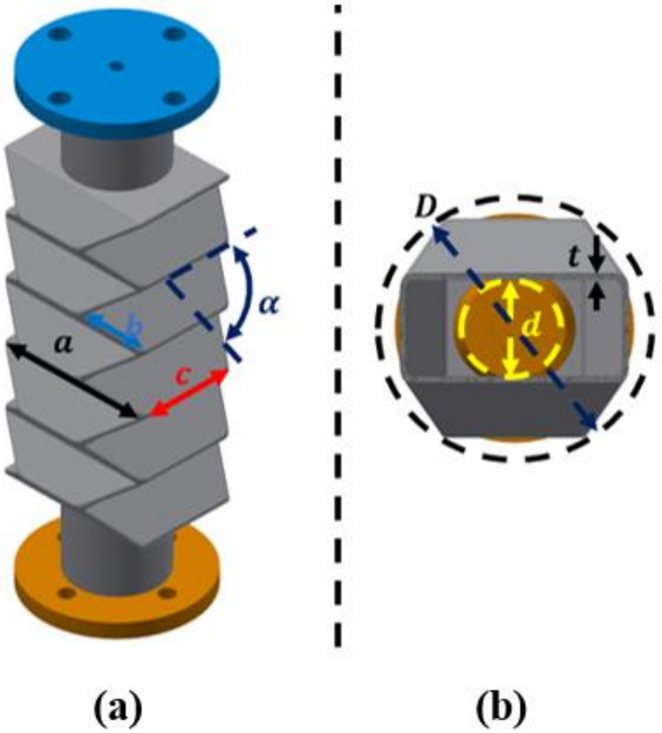

Figure 3.3 The geometric parameters of an OSPA based on accordion pattern (a) Top sectional view. (b) Isometric view.

3.2.2 Mold design

Since the actuator's origami-inspired shape is formed tightly around the mold, to prevent damaging the actuator when removing the mold requires either using a multi-piece mold or destroying the mold. We chose the more difficult option of designing a multi-piece mold since it allows one mold to be reused to fabricate many actuators. This reduces the time spent manufacturing molds and is better for the environment. We also designed the molds to be easily manufactured (e.g. using a common FDM 3D printer).

The main challenges of the mold design process are: the cross-section of each piece of the mold must be smaller than the smallest cross-section of the actuator, the pieces must be designed to stay properly aligned during the thermal forming operation, a viable sequence of removal steps must be developed, and the numbers of pieces should be kept small to avoid complexity. The molds for the actuators based on the accordion and Yoshimura patterns (shown in Figure 3.1) will be used to illustrate two designs that meet these requirements. Each mold consists of seven pieces and is designed such that the removal of the center part facilitates the removal of individual side pieces. The mold designs and removal steps for these actuators are shown in Figure 3.4 and Figure 3.5, respectively. They are shown assembled in their aligned state in part (a) of each Figure. The removal steps are shown in parts (b) to (d) of each Figure.

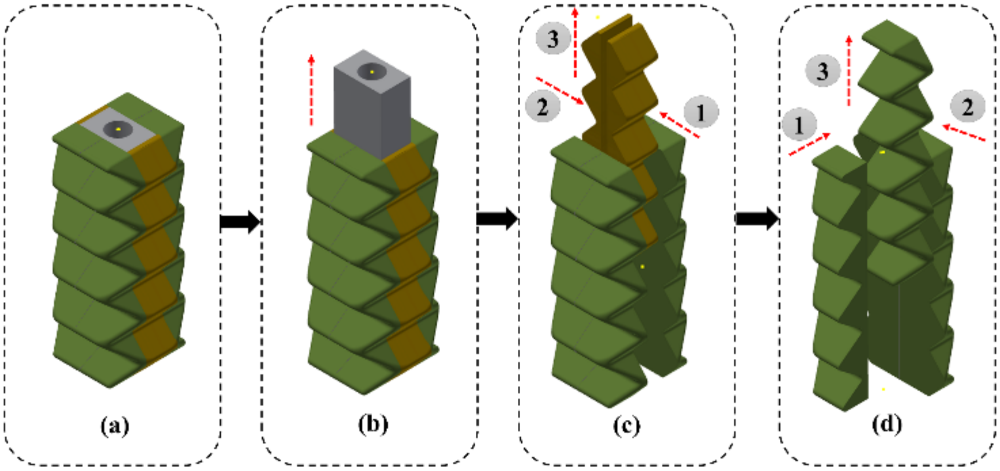

Figure 3.4 Removal steps for the seven-piece accordion pattern mold. (a) CAD model of the assembled mold. (b) Remove the middle part first. (c) Push the two yellow side pieces together, then pull them out. (d) Remove the four green side pieces by sliding and pulling one at a time.

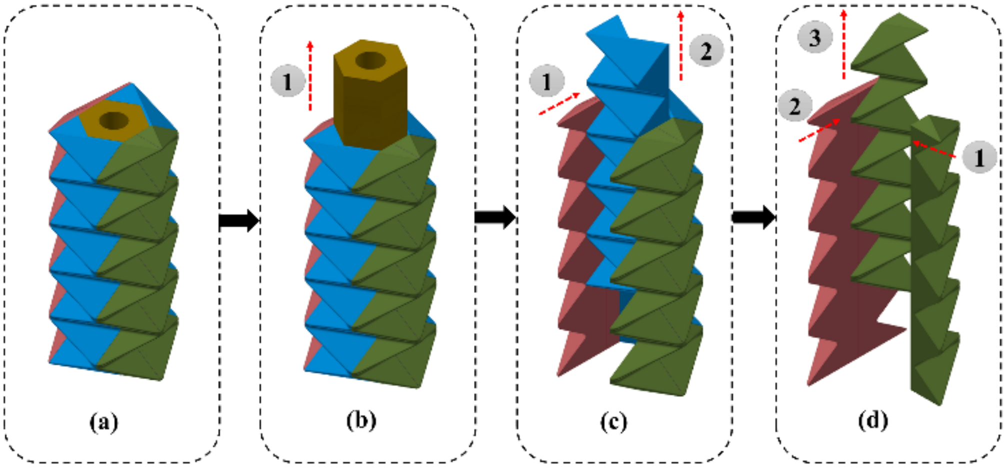

Figure 3.5 Removal steps for the seven-piece Yoshimura pattern mold. (a) CAD model of the assembled mold. (b) Remove the middle part first. (c) Slide each blue side piece over, then pull it out. (d) Remove the four red and green side pieces by sliding and pulling one at a time.

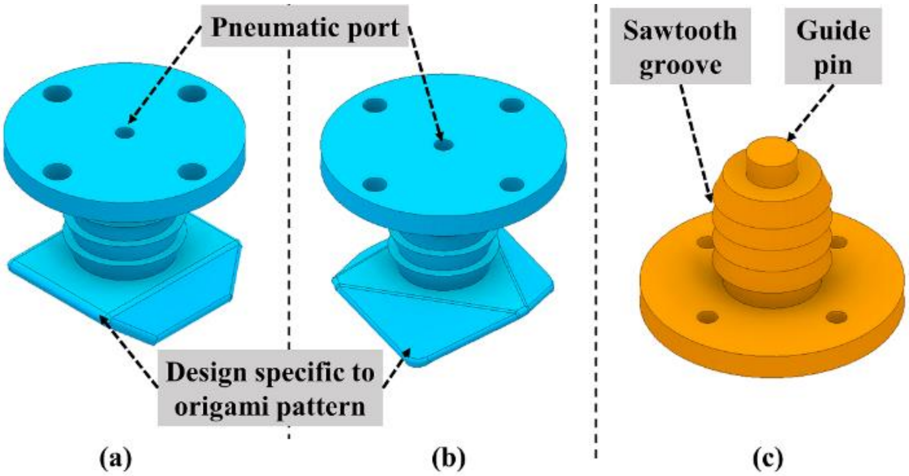

Figure 3.6 End cap designs. (a) Top end cap for accordion pattern OSPA. (b) Top end cap for Yoshimura pattern OSPA. (c) Bottom end cap design that is not pattern specific

3.2.3 Design of end caps and support ribs

The designs for the end caps are shown in Figure 3.6. Each features a circumferential groove with a sawtooth pattern that facilitates sealing between the tubing and cap. The bottom end caps include a guide pin that mates with a hole in the mold to ensure alignment of the mold and cap. The top end caps include a section that transitions from the specific origami pattern to the grooved circular section of the cap. This transition section is used to align the top end cap with the lower section of the actuator as will be explained further in the fabrication section. The extra support it provides also makes the actuator stronger.

The internal support ribs are used to allow the actuator to operate at higher vacuum pressures. They also have the downside of reducing the contraction due to their thickness. The rib designs for the OSPA based on the accordion and Yoshimura patterns are shown in Figure 3.7. They have a radiused edge to reduce stress concentrations at the actuator's hinges and have a lightweight design. The bottom end rib includes a hole that mates with a guide pin on the bottom end cap to provide alignment.

3.2.4 Heat-shrink material selection

Commercial heat-shrink tubing is the essential element of our fabrication method. We tested six commercially available brands of heat-shrink tubing. Commercial heat-shrink tubing is the essential element of our fabrication method. The tubing is made from a material that recovers its original smaller surface area when it is heated to its "full recovery temperature". For OSPA fabrication and performance the most relevant heat-shrink material properties are: tensile strength, ultimate elongation, shrink ratio and full recovery temperature. A higher tensile strength tubing should allow the OSPA to withstand higher pressures and output larger forces without failing. Tubing with larger values for ultimate elongation should be able to conform to the mold better during fabrication and should also provide a greater range of motion when the OSPA is operating. The shrink ratio is

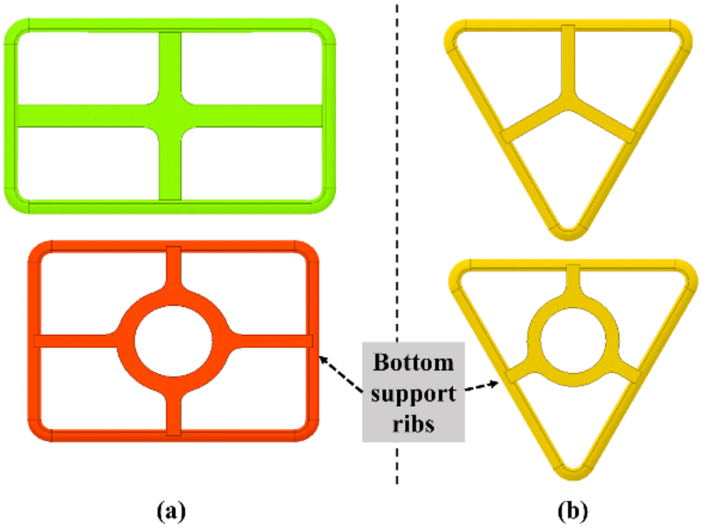

Figure 3.7 Designs for the internal support ribs. (a) For accordion pattern OSPA. (b) For Yoshimura pattern OSPA.

the ratio of the original (unshrunk) diameter to the recovered (shrunk) diameter. A larger shrink ratio should make the seals between the tubing and end caps tighter.

Finally, the full recovery temperature influences both the materials chosen for 3D printing the mold and end caps, and the process used for heating the tubing. It ranges from 60-350 °C. The most common 3D printing filament is polylactic acid (PLA), but it softens at too low a temperature (i.e., its glass transition temperature is around 60 °C) to be used with most heat-shrink materials. Furthermore, preliminary experiments showed that immersing the tubing in boiling liquid produced faster and more homogenous shrinking than other heating methods such as placing the tubing in an oven. Using boiling water is the most convenient choice so heat-shrink tubing with a full recovery temperature of 100 °C (or less) are desirable.

We tested six commercially available brands of heat-shrink tubing with the best combinations of these four properties. The details of these candidates are listed in Table 3.1. All had a 50.8 mm unshrunk diameter and were tested using the accordion pattern mold whose dimensions are given in Section 3.4. Boiling water was used to shrink candidates 3-5, while boiling ethylene glycol was used with candidates 1-2 and 6. Candidate 1 shrunk well at the mold, but split lengthwise at the bottom end cap. Candidates 2-4 did not fail by splitting. However, they did not fit tightly enough on the end caps to seal well. Candidates 5 and 6 shrunk well to the end caps and sealed well. We believe this is due to their larger values of shrink ratio. Candidate 5 has a greater tensile strength, larger ultimate elongation and is significantly less expensive than candidate 6 ($15.50 vs. $84.28 for a 1.22 m length from Digikey). As a result of this study, we selected the candidate 5 heat-shrink tubing (i.e., Qualtek Q2-F4X) for our OSPA fabrication method.

Table 3.1 Commercial heat-shrink tubing candidates for OSPA[1]

No.	Heat-shrink brand and part number	Tensile strength (MPa)	Ultimate elongation (%)	Full recovery temperature (°C)	Shrink ratio
1	Alpha Wire (F2212IN-CL105)	10.3	> 200	121	2:1
2	3M (FP301-2)	16.5	400	130	2:1
3	NTE Electronics (47-21248-BK)	13	400	> 90	2:1
4	TE Connectivity (VERSAFIT-2-0-SP)	10.3	> 200	> 90	2:1
5	Qualtek (Q2-F4X-2-01-QB48IN-5)	>14	> 600	100	4:1
6	Alpha Wire (FIT-421-2IN)	10.3	> 200	121	4:1

1. Material property values are from manufacturers' datasheets.

3.3 Fabrication Method

The steps of the proposed fabrication method are illustrated in Figure 3.8, and can be summarized as follows:

a) Create the computer-aided design (CAD) models for the multi-piece mold, end caps and internal support ribs and export them to stl files.

b) Load the stl files and 3D print the mold pieces and end caps out of acrylonitrile butadiene styrene (ABS). ABS is recommended since it is inexpensive, strong, and has a glass transition temperature of around 105 °C so it will not soften during the heat-shrinking steps. The support ribs can be printed out of PLA since they will not be exposed to heat. An inexpensive FDM 3D printer may be used.

c) Assemble the mold and bottom end cap and insert them inside the heat-shrink tubing. Use cellophane tape to temporarily hold the bottom end cap and tubing together.

d) Immerse the assembly gradually into boiling water until the top surface of the mold is level with the top of the water, then wait until the tubing acquires the shape of the mold (typically around 1 min). After the shrinking process is complete, remove the assembly from the boiling water and remove the cellophane tape.

e) Carefully remove the mold pieces from inside the actuator, starting with the middle part, followed by the side parts one at a time (as previously described in Section 3.2.2). Insert the support ribs, starting with the bottom support rib. The hole in the bottom support rib should be mated with the guide pin on the bottom end cap.

f) Insert the top end cap into the open end of the tubing until it mates with the shape formed in step (d). Next, immerse the assembly in boiling water until the tubing shrinks onto the end cap (requires around 30 sec). If necessary, cable ties or glue (e.g. Clear Gorilla Glue) can be used to achieve better sealing between the tubing and end caps.

Figure 3.8f shows a Yoshimura pattern OSPA that was successfully fabricated using this method. The method has also been used to fabricate the accordion pattern OSPA that is described further in the next section.

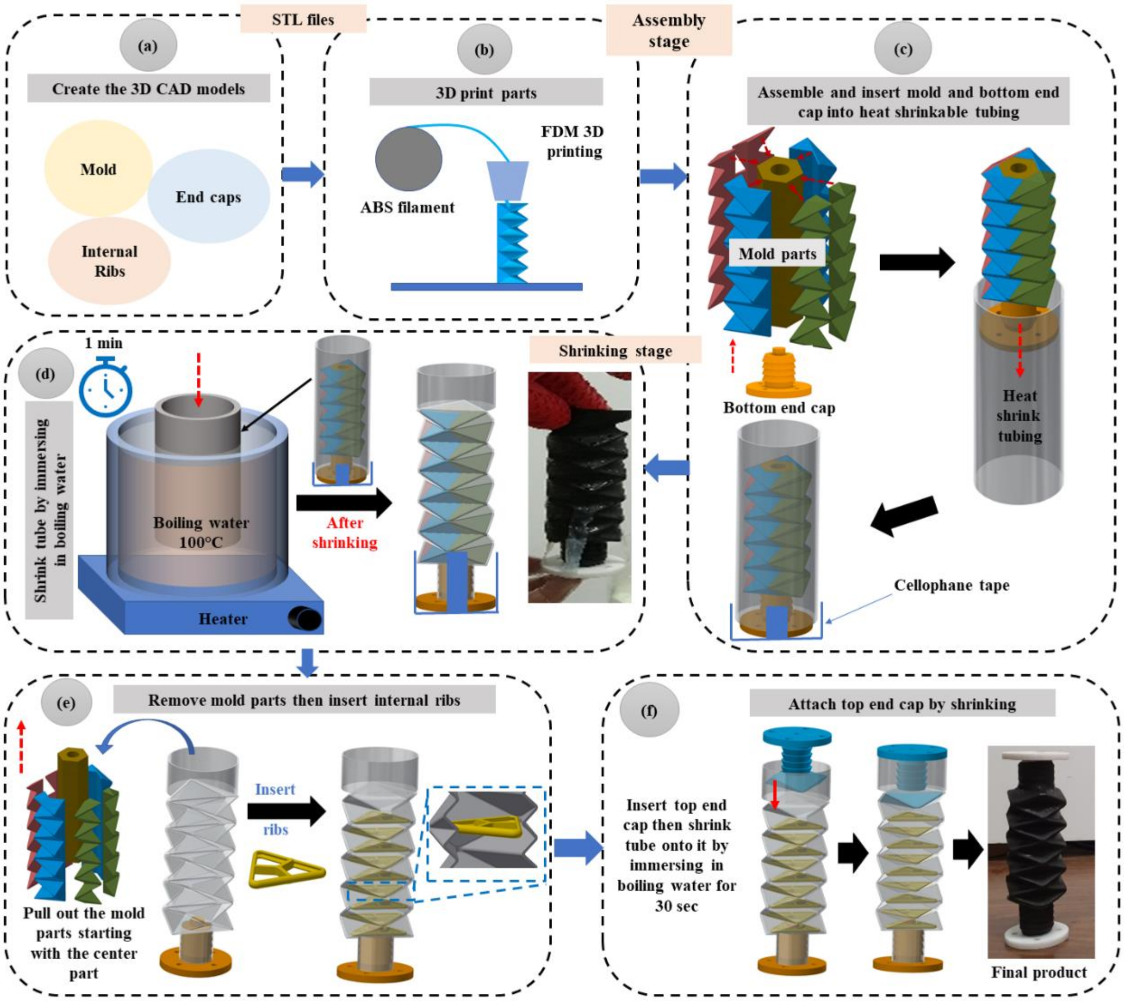

Figure 3.8 The OSPA fabrication method.

3.4 Design and Fabrication of OSPA Prototypes for Testing

The performance testing will be done on two accordion pattern OSPA prototypes. As shown in Figure 3.9a and 3.9b, the design of the origami portion of the actuator consists of a repeating base unit with a trapezoidal shape. Our design has the following dimensions: $\alpha = 1.33$ rad., $a = 46.5$ mm, $b = 18.5$ mm, $c = 20$ mm, $d = 20$ mm, $D = 50$ mm and $t = 1$ mm. As shown in Figure. 9a, its overall length (including the end caps) is $L = 140$ mm, and its effective length is $L_{eff} = 90$

mm. The internal support ribs use the design shown in Figure 3.7a and have an edge radius of 1.5 mm.

The two prototypes were fabricated using the method from Section 3.3. Each prototype used a 175 mm long piece of the heat-shrink tubing selected in Section 3.2.4 (Qualtek, Q2-F4X-2-01-QB48IN-5, 50.8 mm initial diameter).The mold, end caps and ribs were manufactured using an inexpensive FDM 3D printer (Prusa, i3 MK3S). The ribs were made from PLA with 100% infill. The other parts were made from ABS with 50% infill for mass reduction. To improve the sealing reliability, we clamped the heat-shrink tubing to the end caps using TPU flexible cable ties (HellermannTyton,115-07270). The mass of each fabricated actuator was only 73 g.

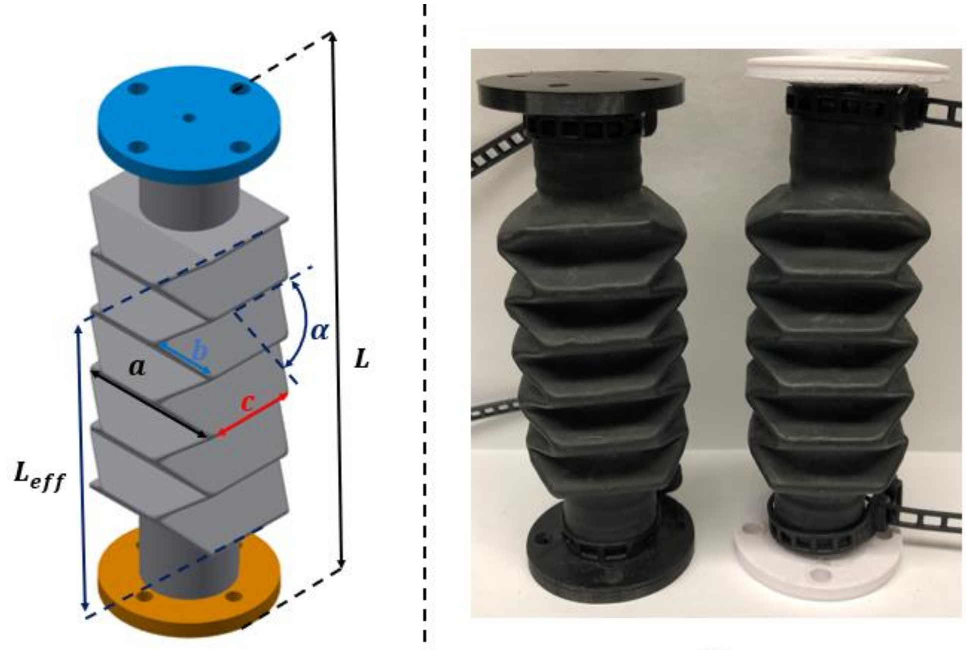

(a)

(b)

Figure 3.9 The accordion pattern OSPA used for testing. (a) Isometric view. (b) Two fabricated prototypes.

3.5 Soft-ended Actuator

We have shown designs and prototypes for applications requiring the OSPA to be rigidly attached at both ends. Other applications may require one or both ends to be flexible. To demonstrate that this is possible with our method, we have fabricated an OSPA with one soft end. The body of this soft-ended actuator was fabricated from a 38 mm diameter tube of Qualtek Q2-F4X heat-shrink. To increase its flexibility and range of motion this actuator does not use any internal support ribs. Its non-rigid end cap was manufactured from flexible TPU filament (NinjaTek NinjaFlex) on an inexpensive FDM 3D printer (Creality Ender-3 Pro). The challenge of creating an end cap that has a soft tip, but also seals well, was met by varying the infill percentage during printing. A 100% infill was used with the sawtooth-grooved section, while only a 20% infill was used for the 15 mm radius hemispherical tip.

The prototype is shown in Figure 3.10. Positive supply pressure can be used to extend the actuator and press the soft end against the surface of an object. Negative pressure can be used to contract the actuator and increase its range of motion. The actuator's original length is 110 mm. In Figure 3.10a, applying a pressure of -55 kPa causes the actuator to reduce its length to 80 mm. In Figure

10b, changing the pressure to160 kPa caused it to extend to a length of 135 mm and contact the rigid metal surface. A contact force of only 12 N was produced by the 5 mm deformation of the soft tip. Potential applications for soft-ended actuators similar to this prototype include clamping systems or grippers for holding fragile objects.

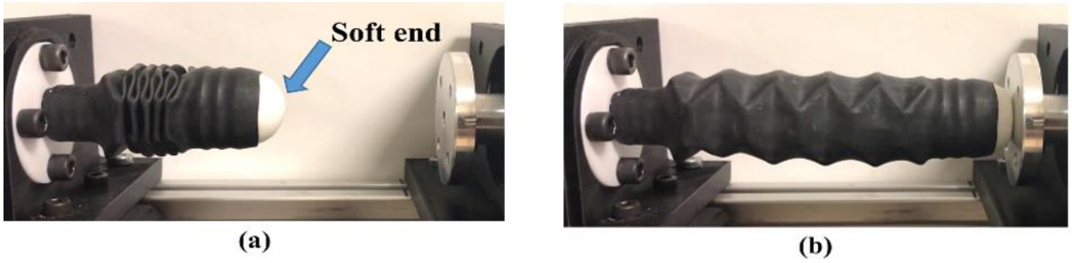

Figure 3.10 Soft-ended OSPA prototype. (a) Contracted using a pressure of -55 kPa. (b) Extended using a pressure of 160 kPa. The soft end can be seen pressing against the rigid metal surface on the right.

3.6 Modified Fabrication Method for Creating Small-diameter Actuators

There are many applications for small-diameter soft actuators, like actuating the fingers of a soft exoskeleton glove [23], actuating soft multi-module robots for minimally-invasive surgery [24], and pipe inspection using crawling soft robots [25]. The proposed fabrication method overcomes many of the limitations of previous fabrication methods due to its short fabrication time, cost efficiency, and the actuators' durability. However, there are some limitations of the proposed approach. In particular, fabricating OSPA with diameters less than 25 mm is very difficult. The main reason for this limitation is the difficulty of inserting the internal support ribs inside the small diameter actuator. To overcome this limitation, we propose modifying the current method by changing the mold's material from ABS to Polyvinyl Alcohol (PVA) which is a water-soluble plastic.

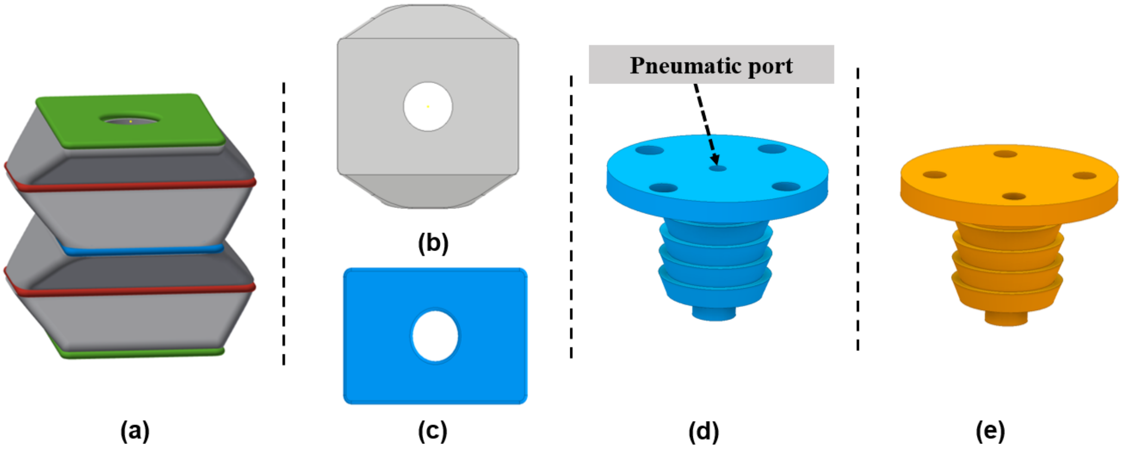

Figure 3.11 3D CAD models of the modified mold, support ribs and end caps. (a) Stacked PVA mold with ABS support ribs. The PVA half-height units are shown in gray, and ABS parts show are shown in green, red and blue. (b) The PVA half-height units. (c) ABS support rib. (d) Modified top end cap. (e) Bottom end cap.

The design of the dissolvable mold is based on dividing the initial mold into half-height units as shown in Figures 3.11a and 3.11b. The design of the support ribs is simplified as a thin rectangular plate with the hole in the middle as shown in Figure 3.11c. The main reason for this hole is it allows the parts to be aligned and allows water to reach all parts of the mold to facilitate the dissolving process. Moreover, the design top end cap has modified so it does not include the transition section as shown in Figure 3.11d. The transition section was removed since it shortens the range of motion and is unnecessary with this modified fabrication method.

The fabrication steps are:

a) 3D print the mold parts, support ribs and end caps.
b) Stack, align and glue together the mold pieces and support ribs to create one assembly. Any instant glue made of cyanoacrylate may be used.

c) After the glue has dried, insert the bottom end cap into the assembly, tape and slide the heat-shrink over the top as shown in Figure 3.8c. Use cellophane tape to temporarily hold the bottom end cap and tubing together.
d) Immerse in boiling water as shown in Figure 3.8d. This shrinks the tubing onto both the mold and bottom end cap.
e) Turn the actuator upside down (so the bottom end cap is at the top), and insert the top end. Use cellophane tape to temporarily hold the top end cap and tubing together.
f) Immerse in boiling water to shrink the tubing onto the top end cap.
g) Remove the pieces of cellophane tape.
h) Submerge the actuator in a warm water bath. The bath should be agitated if possible. Make sure the water flows through the pneumatic port to fill the inside of the mold. The mold should start to dissolve after 3 hours, but may require around 24 hours to completely dissolve.
i) Remove the actuator from the bath, and wash out its insides using running warm water.
j) Allow the actuator to dry.

To prove the feasibility of the modified fabricated method, a two-unit accordion-pattern OSPA has been fabricated. The mold parts were 3D printed from PVA filament using an inexpensive FDM 3D printer (Creality Ender-3 Pro). The end caps and support ribs (with a 1.5 mm thickness) were 3D printed from ABS using the same 3D printer. The infill density of the mold parts, end caps, and support ribs was 20%, 50% and 100%, respectively. The smaller infill densities were used for the mold and end caps to reduce the material usage, cost, and overall fabrication time. A 100% infill was used with the ribs to maximize their strength. The assembled and glued mold pieces and support ribs are shown in Figure 3.12a. The finished OPSA prototype is shown in Figure 3.12b. The

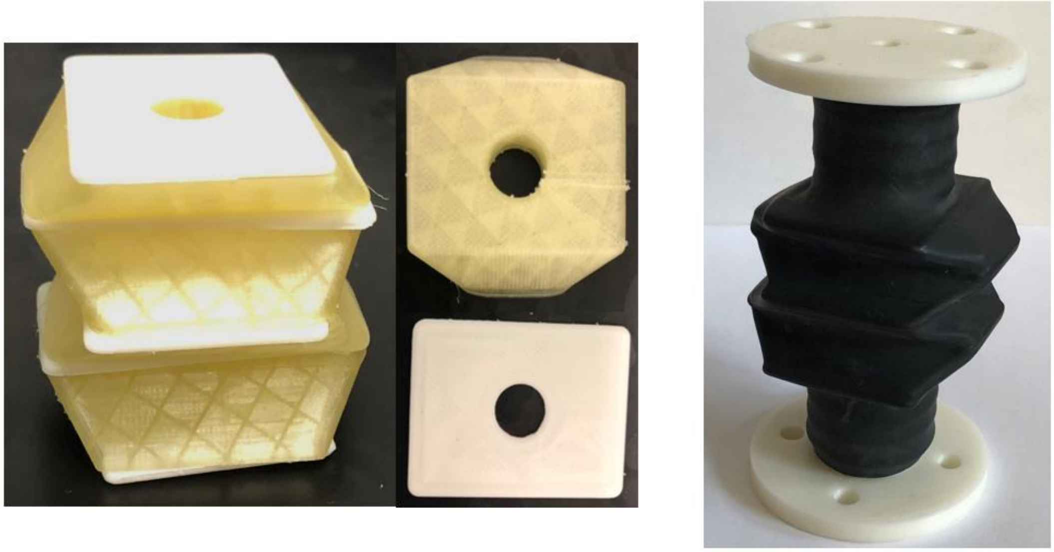

(a) (b)

Figure 3.12 (a) Dissolvable PVA mold parts and support ribs. (b) A two-bellow accordion actuator fabricated with the modified method.

prototype did not leak at pressures up to -80 kPa and could produce a maximum blocked force at zero displacement equal to around 110 N force.

3.7 Conclusions

The proposed method can fabricate an OSPA in less than 10 minutes using thermal forming of commonly available heat shrinkable tubing and a 3D printed reusable multi-piece mold. The OSPA prototypes can produce pushing forces by applying positive internal pressure or pulling forces by utilizing a vacuum (or negative pressure) pump. Using vacuum pressure as an actuation source has the advantage of safety since bursting will not occur if the material fails. The fabrication method does not require specialized equipment and can be used to fabricate actuators based on a wide range of origami patterns (including actuator designs that cannot be produced by folding). It can be used for fabricating actuators with different lengths and diameters using the broad range of commercially available heat-shrink tubing. For example, Qualtek sells Q2-4X heat-shrink tubing with unshrunk diameters ranging from 19 mm to 102 mm in lengths up to 1.2 m. These actuators will typically have rigid end caps used for mounting purposes. However, as demonstrated, it can also be used to fabricate actuators with soft ends. To address the fabrication method's limited ability to produce small diameter actuators, a modified fabrication method is proposed that replaces the reusable mold with a dissolvable PVA mold. In the next chapter, we will present a detailed finite element model for predicting the folding behavior and blocked force of the fabricated OSPAs. The blocked force, stroke, durability and consistency of OSPA prototypes will be investigated experimentally in Chapter 5.

Chapter 4. Modeling, simulation, and validation of OSPA using FEA

4.1 Introduction

Modeling and simulating the behavior of OSPA is a challenging problem. This is due to their complex geometry and the highly non-linear behavior of the materials they are made from. Some computationally inexpensive analytical modeling methods have been developed for origami-inspired actuators, but these are limited to an individual application or origami pattern. FEA is the most general and accurate approach for modeling and simulating soft pneumatic actuators. In this chapter, we describe the development of a complete FEA simulation for the accordion pattern OSPA. We begin by modelling the mechanical behavior of the OSPA's heat-shrink material through tensile testing. The FEA model details are then presented, including importing the CAD model, selecting suitable meshing elements, and defining the different contact types between the elements of the OSPA. Finally, the FEA model simulation results are validated through experimental testing.

4.2 Material Modeling

4.2.1 Introduction

A material model is a prerequisite for developing an analytical or numerical model of an OSPA's force output as a function of its displacement and the supply pressure. Since insufficient information on the material properties of polyolefin heat-shrink was available in the literature, or from the manufacturer, we modeled the mechanical behavior of the Qualtek Q2-F4X heat-shrink tubing empirically.

4.2.2 Tensile testing

One of the challenges in the material characterization process of the polyolefin heat shrink used in the fabrication of OSPA is caused by the thermal forming process. When the tubing takes on the shape of the OSPA during fabrication it is not fully shrunk (i.e., the Q2-F4X tubing does not shrink to ¼ of its unshrunk diameter) and the amount of shrinkage is not a constant. So, its material properties should lie between those of the unshrunk and fully shrunk tubing. This problem will be addressed by tensile testing samples of both unshrunk and fully shrunk tubing and averaging the results.

The tests were conducted according to ASTM Standard D412 (Test Method A) [26], as recommended by the tubing manufacturer Qualtek [27]. This required cutting the unshrunk and shrunk tubing into dumbbell-shaped specimens with the dimensions shown in Figure 4.1. Preparing the specimens from the 50.8 mm diameter unshrunk tube was straightforward, while preparing them from the fully shrunk tube required a procedure to be developed. First, a 150 mm length of tubing is cut off, cut lengthwise to make a rectangular curved piece, and submerged in boiling water (see Figure 4.2a). After it has been fully shrunk, the curved piece is taken out and flattened while it is still hot by pressing it between a stainless-steel plate and a flat table (see Figure 4.2b). Finally, it is cut to the dimensions into the required dumbbell shape (Figure 4.2c) using a laser cutter (Trotec speedy 400).

The tensile tests were performed on ten dumbbell-shaped specimens: five cut from an unshrunk tube and the other five cut from a fully shrunk tube shown in Figures 4.3a and 4.3b. The average measured thicknesses of the unshrunk and fully shrunk specimens were 0.8 mm and 1.3 mm, respectively. The specimens were stretched at a rate of 500 mm/min using an electromechanical universal testing machine (Shimadzu AGS-X Series 50 kN shown in Figure 4.3c).

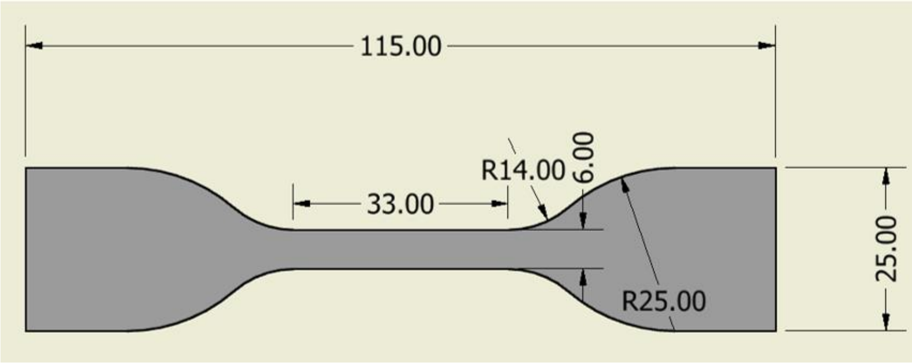

Figure 4.1 Dimensions of uniaxial tensile test dumbbell-shaped specimen (all units in mm) [26].

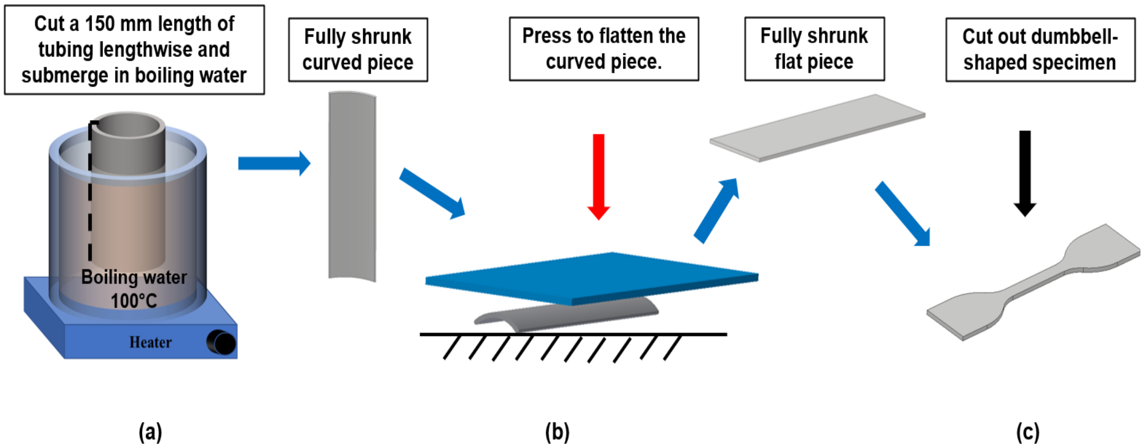

Figure 4.2 Steps to prepare a dumbbell-shaped specimen from the fully shrunk heat-shrink.

The averaged test data is plotted in Figure 4.4. The data exhibits the non-linear stress-strain behavior that is typical of polymers such as polyolefin. The data also illustrates a significant difference between the behavior of the unshrunk and fully shrunk specimens. The trends of the stress-strain curves indicate that the shrinking process makes the material stronger.

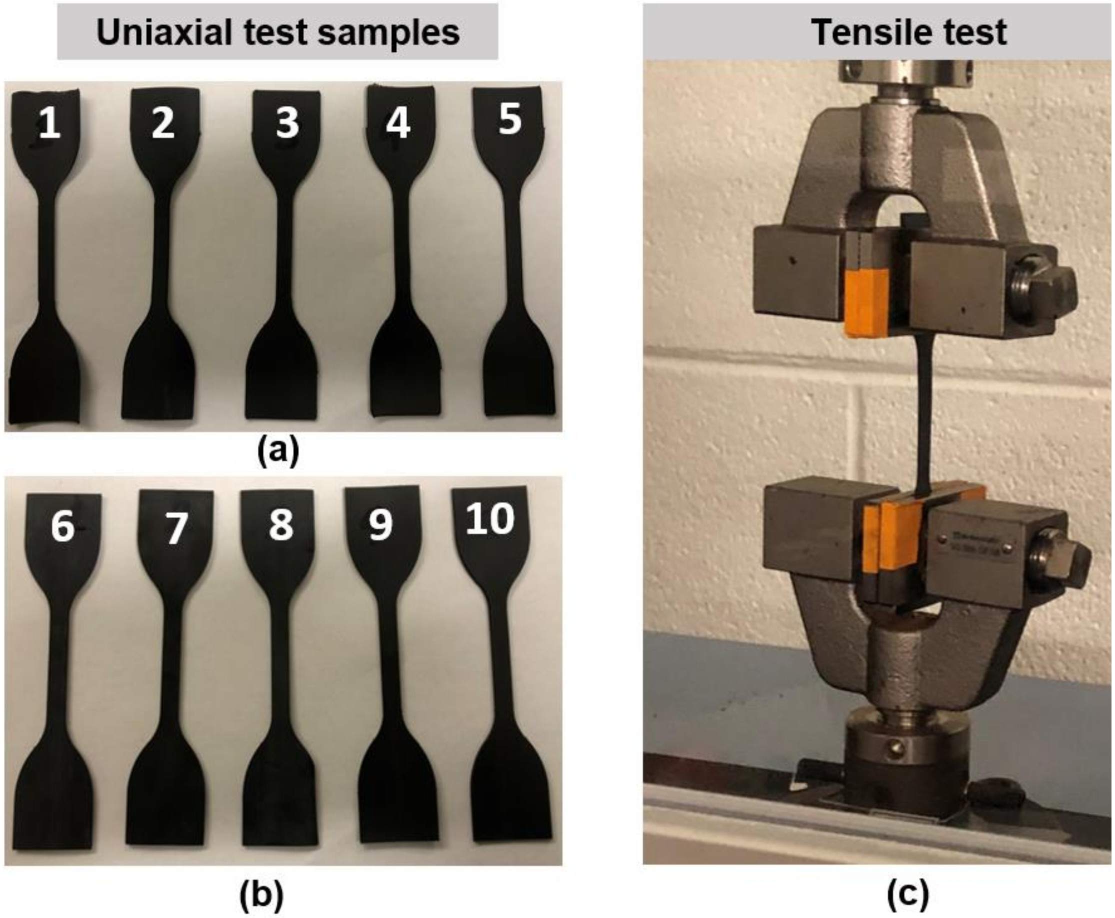

Figure 4.3 (a) Dumbbell test specimens cut from unshrunk polyolefin heat shrink. (b) Dumbbell test specimens cut from fully shrunk polyolefin heat shrink. (c) The specimens were stretched using a Shimadzu tensile test machine with a loading rate of 500 mm/min.

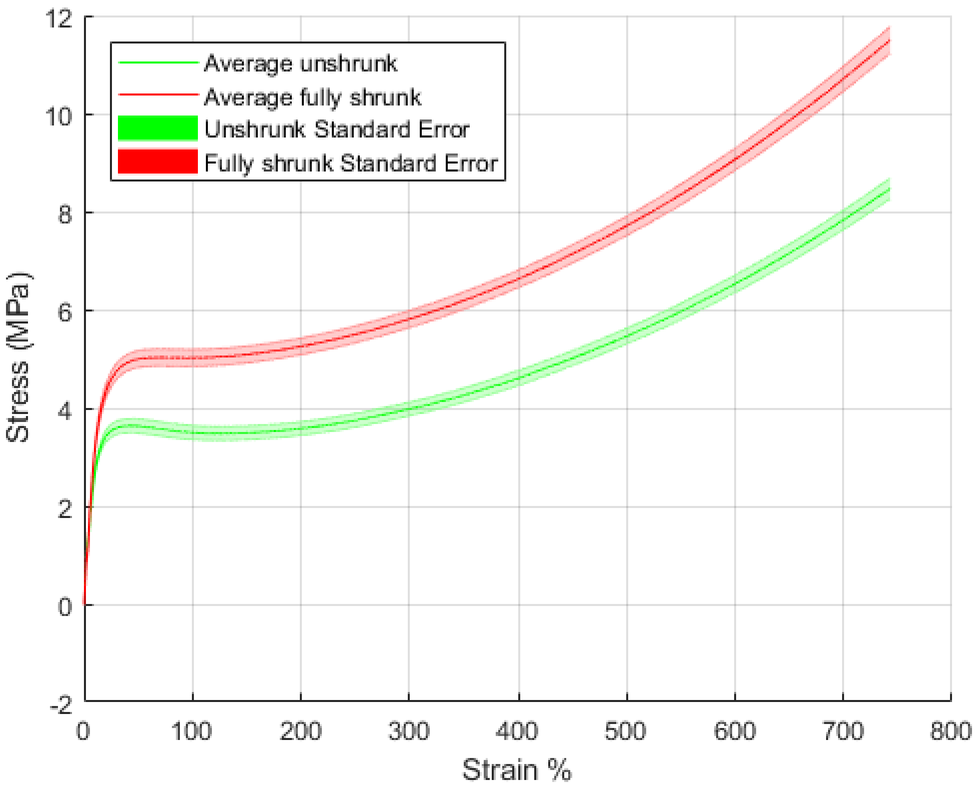

Figure 4.4 Averaged stress-strain curves obtained from the tensile tests for ten dumbbell-shaped specimens (five unshrunk and five fully shrunk). The standard errors are indicated by the shaded areas.

4.2.3 Hyperelastic material model

A hyperelastic material model is the standard approach for capturing the non-linear behavior of polymers, including polyolefins like the material of the Q2-4X tubing. Hyperelastic materials are a class of materials that can undergo deformations of 30%, or more, and sustain negligible plastic deformations [28]. Furthermore, a hyperelastic model only applies to the elastic range of the material. With the Q2-F4X tubing the experimentally determined elastic range exceeded 50% strain. Therefore, to be conservative only the tensile test data up to 50% strain will be used to obtain the hyperelastic material model.

In this research, the commercial software Ansys will be used for the FEA modelling and simulation. Ansys supports various standard hyperelastic material models. The Mooney-Rivlin two-parameter material model in Ansys was fitted to the average of the fully shrunk and unshrunk tensile test data. The thickness was set to the average of the fully shrunk and unshrunk values. The fitted parameters are: $C_{10} = -9.24\times10^{5}\ \mathrm{Pa}$, $C_{01} = 4.87\times10^{6}\ \mathrm{Pa}$ and $D_1 = 0$.

4.3 Importing the CAD model and Selecting Suitable Mesh Settings

The CAD model of the OSPA was created using Autodesk Inventor. To reduce the simulation time, the CAD model details which did not affect the actuator's simulated behavior were modified in the CAD model before it was imported into the FEA software. These modifications were done to speed up the convergence of the FEA solution. The sawtooth grooves and air inlet hole in the end caps were removed, as shown in Figure 4.5a and 4.5b. The shapes of the internal support ribs were modeled as a flat plate with a middle hole and with the same thickness as the real support ribs, as illustrated in Figure 4.5c.

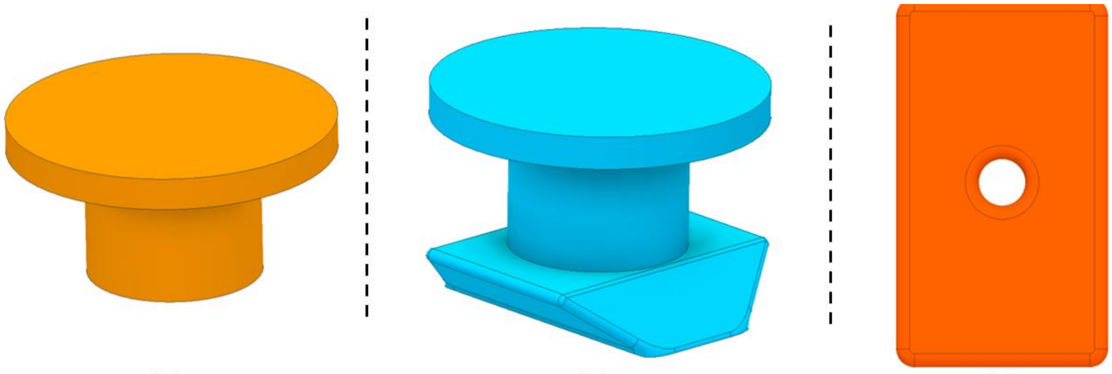

Figure 4.5 Modified CAD model used for FEA simulation. (a) Bottom end cap without the sawtooth grooves. (b) Top end cap without the sawtooth grooves and air inlet hole. (c) Simplified support rib.

The imported CAD model is edited with the help of Ansys DesignModeler, which is one of the CAD tools existing in Ansys Workbench. In particular, the accordion pattern OSPA is symmetric about the YZ and XZ planes. This allowed the model used for the FEA to be simplified from the full model shown in Figure 4.6a to the quarter symmetry model shown in Figure 4.6b without loss of accuracy. This simplification significantly sped up the computation time since it reduced the size of the FEA problem by 75%.

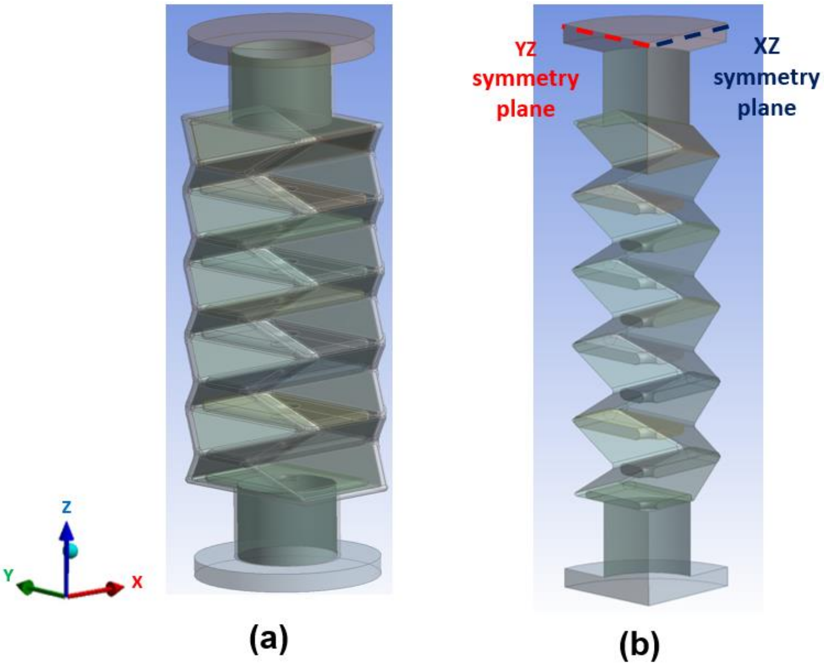

Figure 4.6 (a) The imported full 3D CAD model. (b) Quarter symmetry CAD model.

The locking phenomena is another issue that had to addressed when developing the FEA model. It is a common problem in FEA of thin-walled structures when using solid elements for meshing [29]. To accurately capture the folding behavior and membrane effect of the thin accordion pattern walls of the OSPA while avoiding the locking phenomena, two choices were available. The first option was to increase the number of elements through the thickness of the thin-walled structure to at least three elements. The second option was to use shell elements.

The main disadvantage of the first method is that it would significantly increase the number of model elements (up to around 200,000 for the quarter model) and that would have caused the simulation time to dramatically increase, so we choose the shell element. To use shell elements, a surface was first created from the solid model of the OSPA (shown in Figure 4.7b) using Ansys DesignModeler. The wall thickness was then assumed to be uniform and was adjusted to match the average measured wall thickness of the fabricated OSPA which was 1 mm.

Two element types were used to mesh the model in Ansys. Tetrahedral elements with ten nodes (SOLID187) were used for the end caps and support ribs, as shown in Figure 4.7a, while shell elements (SHELL181) were used for meshing the walls of the OSPA as shown in Figure 4.7b. After performing a mesh independence study, the number of elements was set to 28,495.

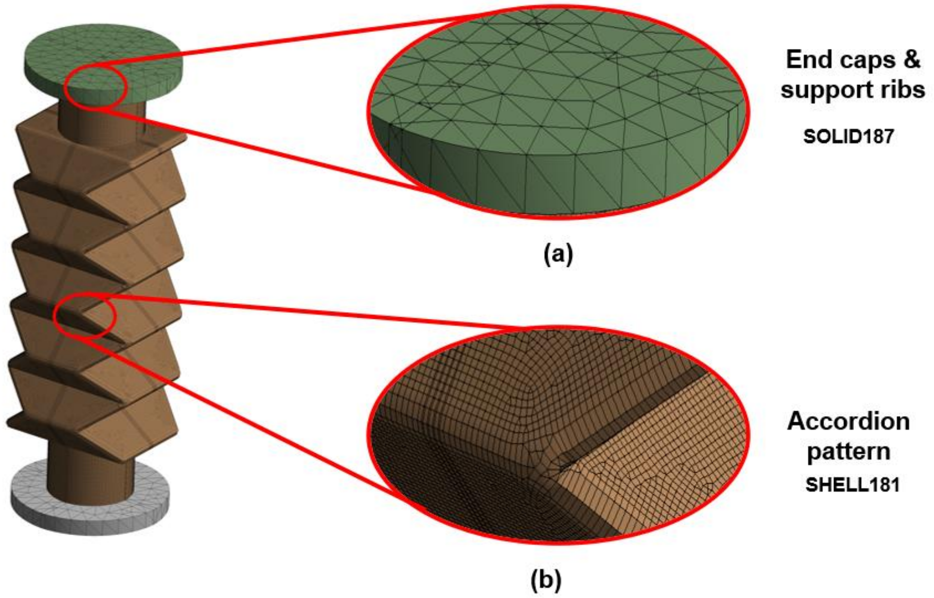

Figure 4.7 Two element types were used to mesh the model. Tetrahedral elements with ten nodes (SOLID187) were used for the end caps and support ribs. Shell elements (SHELL181) for the OSPA accordion pattern walls.

4.4 Contact definitions

The presence of non-linear contacts can cause FEA convergence problems. This was particularly challenging for the OSPA simulation since it involves many contact pairs, including: bonded contact between the top end cap and the accordion pattern wall; frictional contact between the outer surfaces of the wall, frictional contact between two successive support ribs; frictional contact between the inner surfaces of the wall; bonded contact between the bottom end cap and the accordion pattern wall; and frictional contact between the wall inner surface and the top and bottom surfaces of each support rib. These are shown in Figure 4.8 parts (a)-(f), respectively. The settings of the non-linear contacts were adjusted to support the convergence of the problem. The normal stiffness factor was set to 0.1. The coefficient of friction was set to 0.2 based on the recommendations given by Ansys for such complex contact cases.

4.5 FEA modelling for prediction of deformation and blocked force

The FEA model was created using the Static Structure module in Ansys Workbench 2020 R1 with the large deflection option selected. The FEA model can be used to predict the total deformation and the blocked force of the accordion pattern OSPA caused by applying an internal vacuum pressure.

To simulate the total deformation due to the folding behavior of the accordion pattern OSPA, the boundary conditions were fixed support at the bottom end cap, and a negative pressure was applied normal to the internal walls as a load. These boundary conditions are illustrated in Figure 4.9. Frictional contact pairs were defined as explained in Section 4.4. The solution of this FEA simulation predicts the deformation developed due to the application of the internal pressure, the resultant von Mises stress and the resultant von Mises strain. These results are shown for a pressure of -15 kPa in Figures 4.10, 4.11a and 4.11b, respectively.

As shown in Figure 4.10, the predicted maximum deformation is 51.6%. The results in Figure 4.11 show that the maximum stress and strain occur near the vertices. The predicted maximum strain of 28.8% is well below the conservative 50% limit established in Section 4.2.3 so folding the actuator should not plastically deform it in practice.

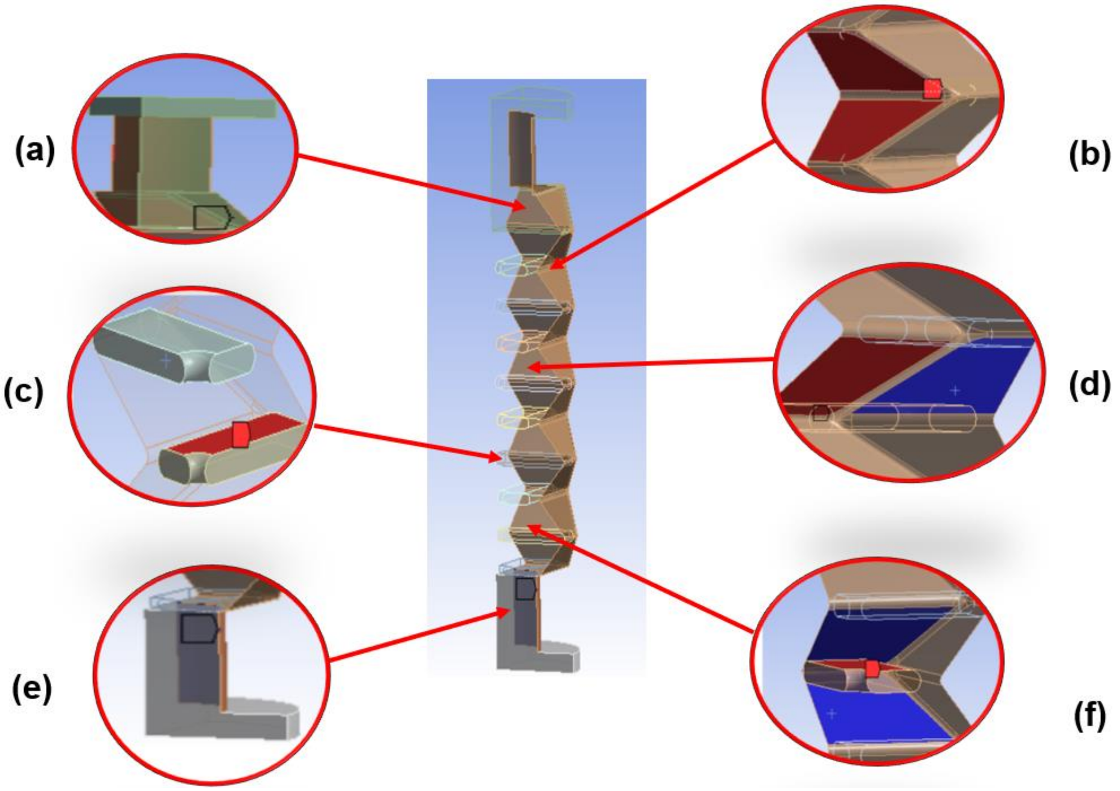

Figure 4.8 Contact definition between the different parts of the accordion pattern OSPA. (a) Bonded contact between the top end cap and the accordion pattern wall. (b) Frictional contact between the outer surfaces of the wall. (c) Frictional contact between two successive support ribs. (d) Frictional contact between the inner surfaces of the wall. (e) Bonded contact between the bottom end cap and the accordion pattern wall. (f) Frictional contact between the wall inner surface and the top and bottom surfaces of a support rib.

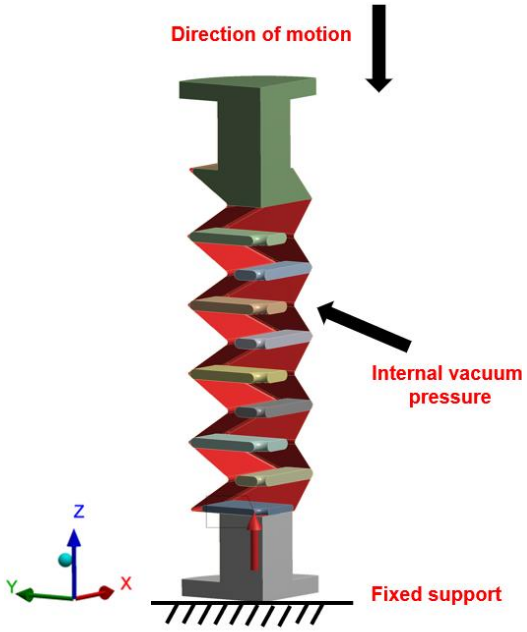

Figure 4.9 The boundary conditions for FEA of accordion pattern OSPA to predict the deformation are fixed support of the bottom end cap and a loading condition as negative pressure normal to the internal walls.

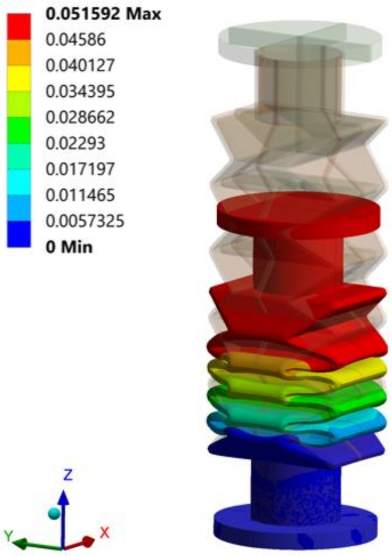

Figure 4.10 The deformed (folded) model of OSPA under the effect of internal vacuum pressure.

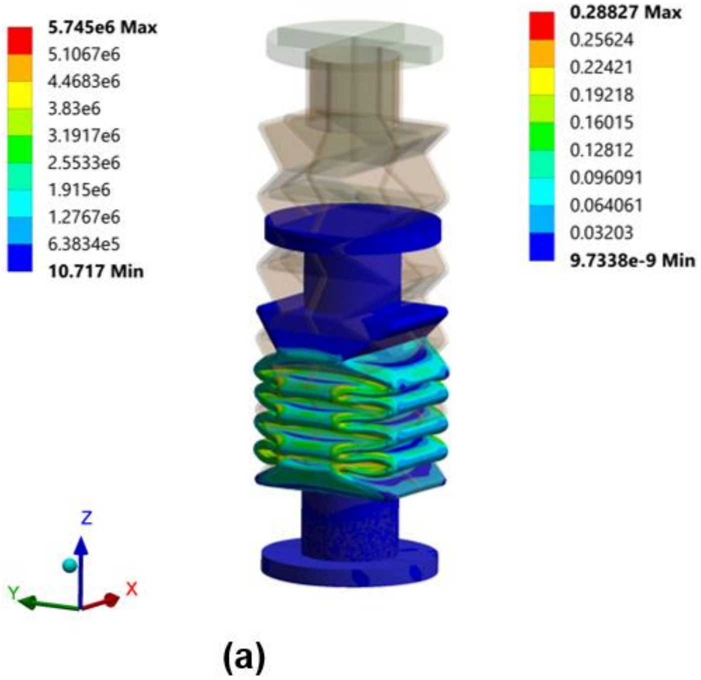

Figure 4.11 Predicted stress and strain distributions due to folding. (a) von Mises equivalent stress in Pa. (b) von Mises equivalent strain.

To simulate the blocked force of the accordion pattern OSPA, the boundary conditions were fixed support at the bottom and top end caps of the actuator, and a negative pressure normal to the internal walls of the OSPA was applied as a load. Frictional contact pairs were defined as explained in Section 4.4. The solution of this FEA simulation predicts the reaction force generated at the fixed supports due to the application of internal pressure, the resultant von Mises stress, and von Mises strain. The predicted stress and strain distributions are shown in Figure 4.12. Compared with the results in Figure 4.11, these stresses and strains are significantly smaller. Since the evaluated force is a reaction force at the support, the blocked force generated by the actuator is of equal magnitude and opposite direction. As shown in Figure 4.13, the reaction force at the fixed support is in the -Z direction, and thus the blocked force generated by the OSPA is in the +Z direction.

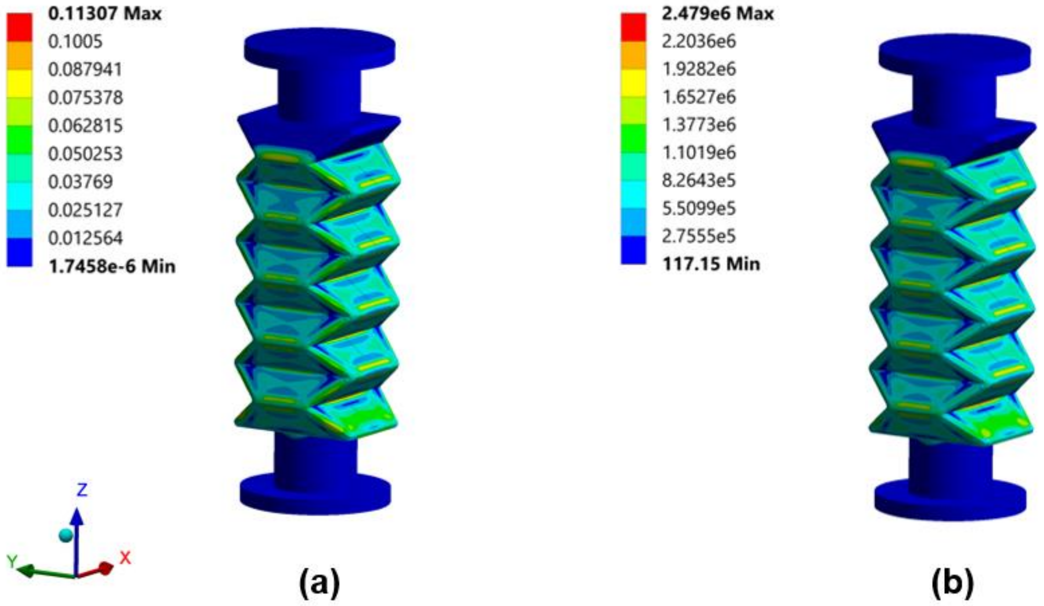

Figure 4.12 Predicted stress and strain distributions due to the blocked force with an internal pressure of -40 kPa. (a) von Mises equivalent strain. (b) von Mises equivalent stress in Pa.

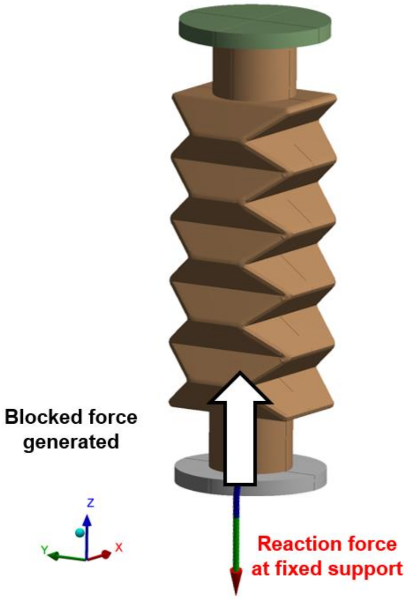

Figure 4.13 The white arrow shows the direction of the blocked force generated by the OSPA under the effect of internal vacuum pressure.

4.6 Validation of the FEA model.

To simulate isometric and isobaric testing of the OSPA a two-step simulation was developed. The boundary conditions applied in the first step were fixed support of the bottom end cap, and a fixed displacement of the top end cap, as shown in Figure 4.14a. To match the experiments, the displacement was varied from 0 to 40 mm in 10 mm increments. In the second simulation step, the displacement of the end caps was kept fixed, and a negative pressure normal to the internal walls of the OSPA was applied as shown in Figure 4.14b, ranging from -20 to -80 kPa. Frictional contact pairs were defined as explained in Section 4.4.

Comparisons between FEA and experimental results are presented in Figures 4.15 and 4.16. The equipment and procedure used to obtain the experimental results are presented in Chapter 5. The partially folded shape of the accordion pattern OSPA predicted by FEA and its actual deformed shape are qualitatively compared in Figure 4.15. The predicted, and real shapes are visually similar. A quantitative comparison of the predicted and experimental blocked force results for displacements of 0, 20 and 40 mm is shown in Figure 4.16. Two trends can be observed from these results. First, the deviations tended to decrease when the displacement increased. Second, the deviations increased as the blocked force increased. The maximum deviation of 6.9 N (or 5.7% of the range) occurred at -80 kPa and zero displacement.

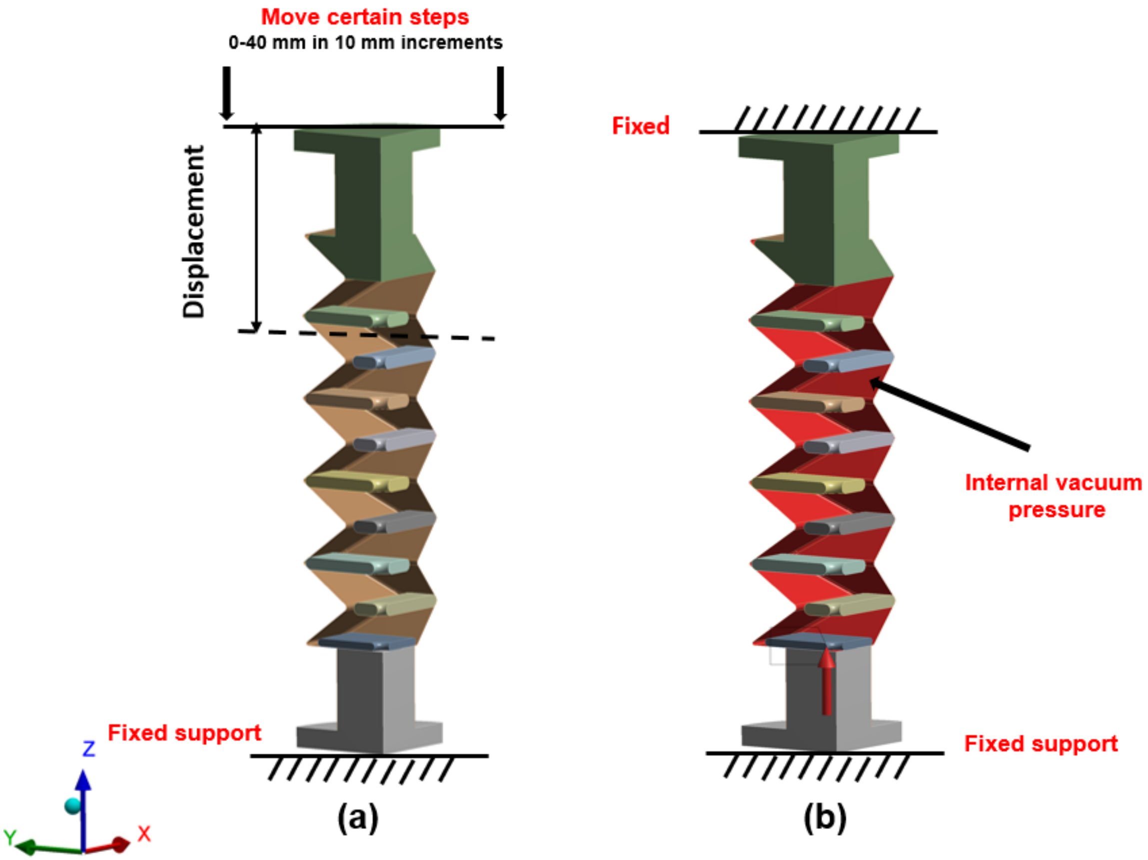

Figure 4.14 The boundary conditions for the two-step FEA simulation. (a) First step boundary conditions fixed support of the bottom end cap and a fixed displacement of the top end cap. (b) Second step boundary conditions fixed support of the bottom end cap, fixed displacement of the top end cap and loading condition as negative pressure normal to the internal walls.

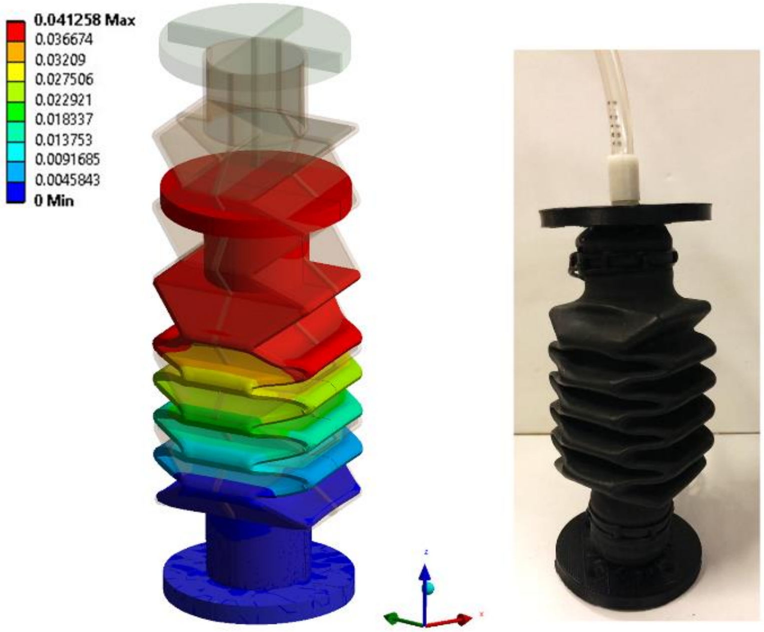

(a) (b)

Figure 4.15 Comparison of the partially folded shapes of the accordion pattern OSPA. (a) FEA prediction. (b) Experimental result.

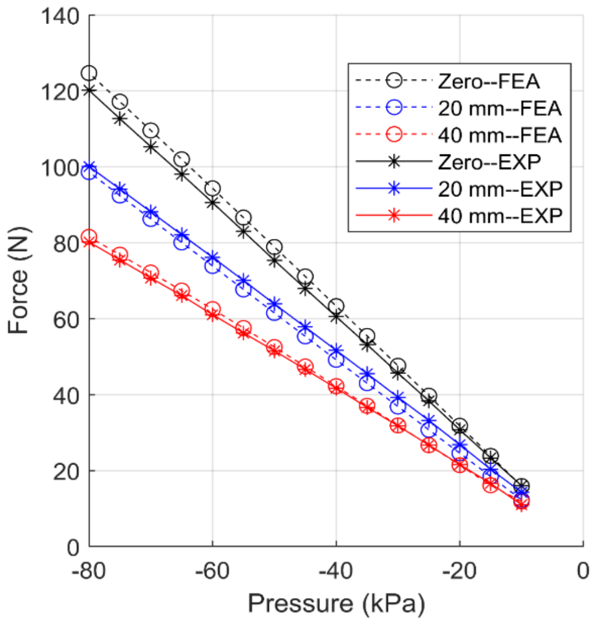

Figure 4.16 Comparison of the blocked forces predicted by FEA to the experimental results for displacements of 0, 20 and 40 mm.

4.7 Conclusions

The development of a detailed non-linear FEA model of the accordion pattern OSPA was presented. This model can be used to predict the folding behavior and blocked force of the OSPA when either vacuum or positive pressure is used. It includes a nonlinear hyperelastic model of the heat-shrink material's behaviour (obtained empirically by performing tensile tests), nonlinear frictional contacts and multiple element types. Exploiting the symmetry of the accordion pattern allowed the size of the FEA problem to be reduced by 75%, saving significant computation time. The developed model was validated experimentally. The maximum deviation between the blocked force simulation results and experimental measurements was 5.7%. This model will be used in the OSPA design optimization presented in Chapter 6.

Chapter 5. Experimental testing and OSPA characterization

5.1 Introduction

To allow comparisons with existing soft pneumatic actuators, the procedures and results of extensive tests performed on OSPA prototypes will be presented and discussed in this chapter. The hardware and software developed to perform these experiments is described first. Next, a series of isometric and isobaric tests are performed to evaluate the blocked forces produced by accordion pattern and Yoshimura pattern OSPA prototypes. Then the accordion pattern OPSA's contraction ratio vs. pressure and hysteresis when lifting various payloads are studied using isotonic contraction tests. Next, the actuator's potential service life is evaluated through lengthy cyclic fatigue testing under load. In the subsequent sections, the consistency of the fabricated prototypes and the fabrication method's scalability are investigated, followed by the chapter's conclusions.

5.2 Hardware and software development

The measurement setup shown in Figure 5.1 was designed, manufactured and assembled for performing isometric and isobaric tests of the OSPA prototypes. It uses a stepper motor driven linear actuator (Festo, ESBF-BS-32-200-10P) to change the length of the OSPA. Vacuum pressure is generated using two small vacuum pumps connected in series (AirPO, D2028 12V, mass 0.34 kg). The accumulator has a volume of 1 L (Festo, CRVZS-2-160236). Valve V1 is an on/off solenoid valve (MAC, 34B-AAA-GDFB-1BA). Valves V2 and V3 are proportional solenoid valves (Clippard, ET-P-05-25A0). The pressure is measured using an 0-345 kPa absolute pressure sensor with a ±1% accuracy (SSI Technologies, P51-50-A-B-I36-5V-R) and the force gauge has a range of 490 N with an accuracy of

±0.2% (Imada, DPS-110). A linear potentiometer (Novotechnik, T150) with a 150 mm range and ±0.075% linearity is used to measure the actuator's displacement. After low-pass filtering at 106 Hz, the signals are sampled at 1 kHz. The measurement and data collection are performed using custom written Matlab code running on a 64-Bit Windows PC (with an Intel i7 3770 3.4 GHz processor) equipped with a data acquisition system (DAQ) card (National Instruments, NI-6221).

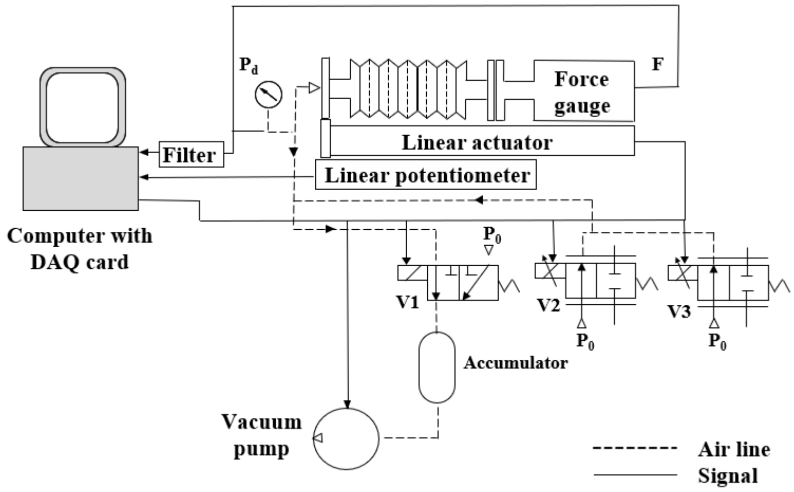

Figure 5.1 Measurement setup built for the isometric and isobaric testing. (a) Schematic (b) CAD model.

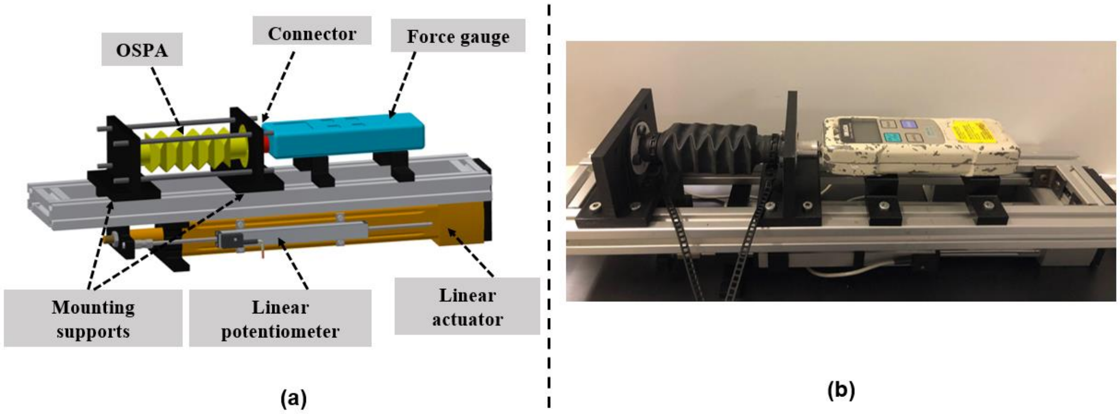

Figure 5.2 Measurement setup built for the isometric and isobaric testing. (a) CAD model. (b) the actual measurement setup.

The software algorithm for performing the isometric and isobaric testing is:

1- Close all valves and turn off the vacuum pumps.
2- Starting from zero, increase the displacement by 10 mm increments (using the linear actuator) up to the actuator's maximum value. For example, with the accordion pattern OSPA the displacement was stepped from zero to 40 mm.
3- At each displacement increment, the vacuum pressure is reduced by -5 kPa increments from -10 to -80 kPa.
4- To apply the vacuum pressure, the pump is turned on until the measured pressure reaches the desired pressure.
5- If the vacuum pressure becomes too large, the pump is turned off, and the valves are opened until the pressure returns to the desired pressure.
6- The measured force and pressure during one measurement cycle are saved.
7- Each measurement cycle for a certain displacement and pressure is repeated three times by repeating steps from 4 to 6.
8- Next, a new desired vacuum pressure is set as by returning to step 2.

9- After completing the vacuum increments in step 2, a new displacement increment is applied, and steps 3 to 7 are repeated.

10- After completing the measurements at the maximum displacement, the pump is turned off, and all valves are opened to allow the pressures to return to atmospheric pressure.

A 2nd measurement setup was developed to perform isotonic contraction and cyclic fatigue tests of the OSPA prototypes. A CAD image of the mechanical components is shown in Figure. 12. The OSPA moves vertically, and constant force loads are generated by attaching different payload masses (up to 8.6 kg). A linear potentiometer (Novotechnik, T100) with a 100 mm range and ±0.075% linearity is used to measure the OSPA's displacement. For safety, the moving components are mounted inside a clear acrylic tube. Custom parts were 3D printed from PLA to attach the OSPA and other components. The vacuum pumps, pressure sensor, valves, data acquisition card, and PC used for the isometric testing were also used with this setup. For the cyclic fatigue tests, we used a vacuum pump with a higher flow rate of 40L/min to reduce the testing time (VN-C4 12V 42W, 85KPa, Flow 40L/min, mass 0.488 kg).

The software algorithm of the isotonic contraction and cyclic fatigue testing is:

1- At the beginning of a test, the user sets the payload's value in the code to match the payload connected to the actuator.

2- The desired value of the vacuum pressure is set to -80 kPa.

3- All valves are closed, and the pump is turned off.

4- To apply the vacuum pressure, the pump is turned on until the measured pressure reaches the desired pressure.

5- If the vacuum pressure becomes too large, the pump is turned off, and the valves are opened until the pressure returns to the desired pressure.

6- The measured displacement and pressure during each cycle are saved.
7- Each measurement cycle for the desired displacement and pressure is repeated the desired number of times by repeating steps from 4 to 6.
8- After the last cycle has completed, the pump is turned off, and all valves are opened to allow the pressures to return to atmospheric pressure.
9- Tell the user to manually change the payload mass, and then begin the next test by returning to step 1.

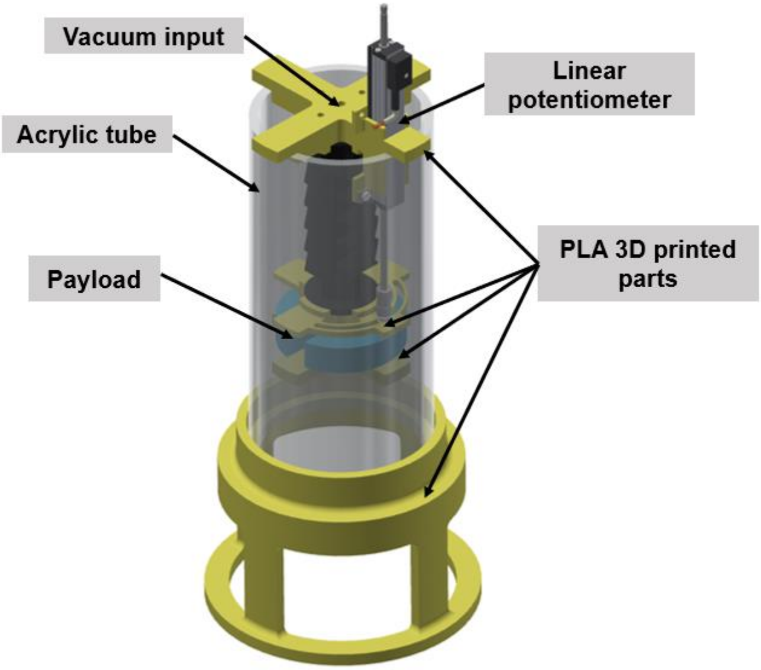

Figure 5.3 CAD model of the measurement setup built for the isotonic contraction and cyclic fatigue testing.

5.3. Isometric and isobaric testing

The test procedure consisted of keeping the OSPA prototype's displacement constant at a target value while the pressure was slowly decreased through a series of target pressure values. Since the OSPA's max stroke is around 40 mm, the displacement targets were 0, 10, 20, 30, and 40 mm. The pressure targets were from -10 kPa to -80 kPa in increments of -5 kPa. 100 samples were sampled at 1 kHz at each target point and averaged to reduce noise.

5.3.1 Blocked force measurement of accordion pattern OSPA

In this section, we evaluate the performance of an accordion pattern OSPA with the geometric parameters illustrated in Chapter 3 by performing isometric and isobaric tests. Each test was repeated three times, and the forces averaged. The average forces from the isometric tests are plotted vs. pressure in Figure 5.4a. These forces are also known as "blocked forces." The results show that the relationship between the blocked force and pressure is close to linear over the OSPA's stroke. The isobaric force vs. displacement curves are plotted in Figure 5.4b. These show that the force decreases as the displacement increases and that the reduction is roughly linear, except at the displacement of 40 mm, where a larger decrease can be observed. The reason for the larger decrease at 40 mm is the increased value of stiffness of the accordion OSPA at this max displacement. A maximum force of 124 N was produced at zero displacement with a -80 kPa pressure.

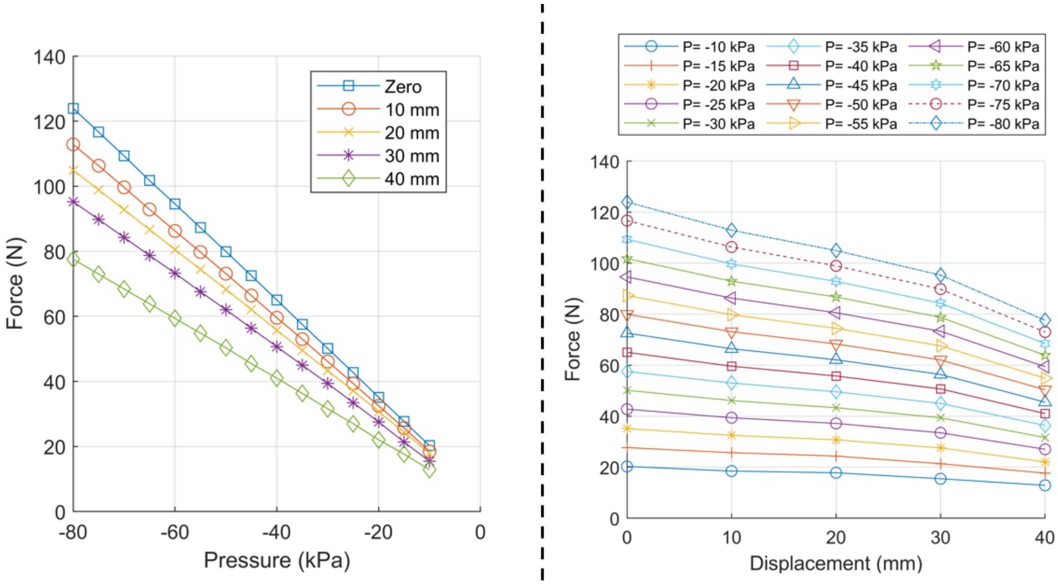

(a) (b)

Figure 5.4 Experimental results for the accordion pattern OSPA.(a) Isometric plots of force vs. pressure. (b) Isobaric plots of force vs. displacement.

5.3.2 Blocked force measurement of Yoshimura pattern OSPA

In this section, the performance of a Yoshimura pattern OSPA prototype will be evaluated by performing the isometric and isobaric testing, as shown in Figure. 5.5a. The design of the origami portion of the actuator consists of a repeating base unit with an isosceles triangular shape. Our design has the following dimensions: $\alpha = 1.33$ rad., $a = 44$ mm, $b = 27$ mm, and $t = 1$ mm, as shown in Figure. 5.5b, its overall length (including the end caps) is $L = 140$ mm, and its effective length is $L_{eff} = 90$ mm.

Each test was repeated three times, and the average blocked forces are plotted vs. pressure in Figure. 5.6a. The results show that the relationship between the blocked force and pressure is close to linear over the OSPA's stroke. The isobaric force vs. displacement curves are plotted in Figure 5.6b. These show that the force decreases as the displacement increases and that the reduction is roughly linear. A maximum force of 115 N was produced at zero displacement with a -80 kPa pressure. By comparing Figures 5.4 and 5.6, it can be seen that the blocked force generated from the accordion pattern OSPA is greater than Yoshimura pattern OSPA, so for the rest of our experimental testing will be performed on the accordion pattern OSPA.

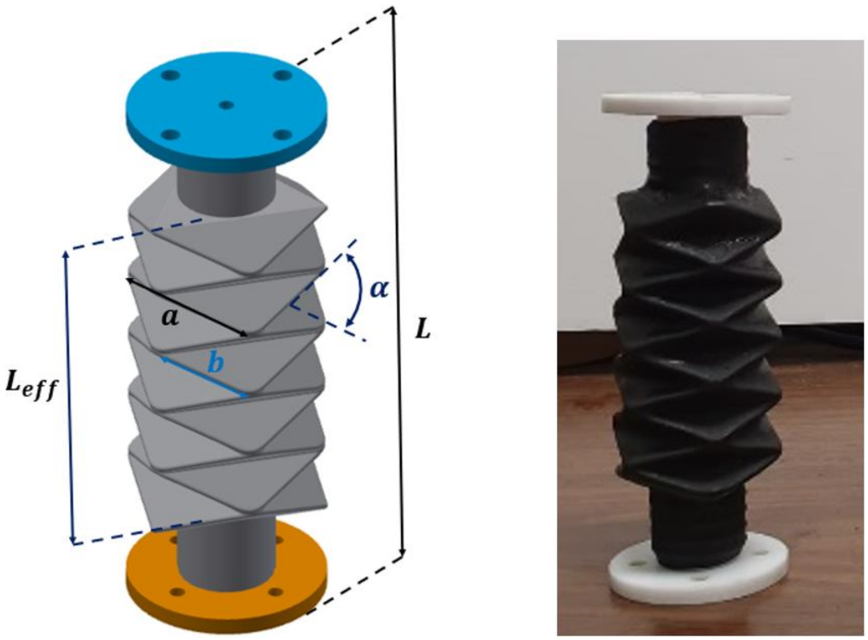

(a) (b)

Figure 5.5 (a) Main geometric parameters of the Yoshimura pattern OSPA design. (b) Yoshimura pattern OSPA prototype used for testing.

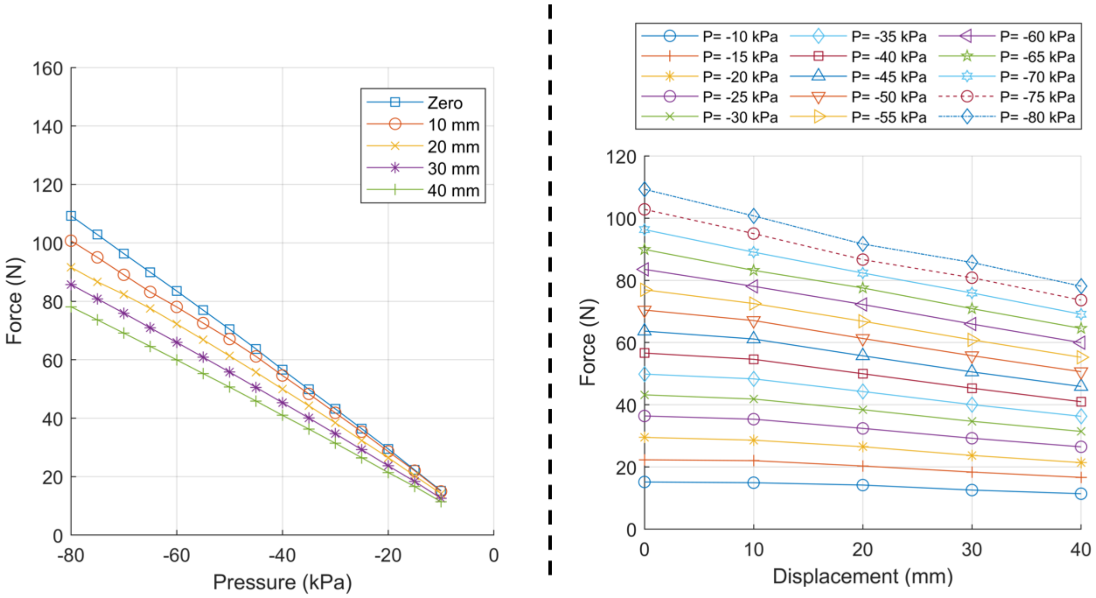

(a) **(b)**

Figure 5.6 Experimental results for the Yoshimura pattern OSPA. (a) Isometric plots of force vs. pressure. (b) Isobaric plots of force vs. displacement.

5.4 Isotonic testing

The test procedure for each isotonic contraction test begins with attaching a payload mass to the tested OSPA; payloads masses of 2.0, 3.3, 4.0, 5.3, 6.5, 7.7 and 8.6 kg were used. After that, the pressure was slowly decreased until it reached -80 kPa while the actuator's displacement was measured simultaneously. The displacement was then converted to contraction ratio by dividing by the OSPA's length at zero pressure.

The isotonic contraction tests were repeated five times for each payload and the results averaged. Pictures of the contraction tests with payloads of 2.0 and 8.6 kg are shown in Figure. 5.7a and 5.7b, respectively. These pictures show that the actuator can lift the 8.6 kg payload but with a reduced displacement compared to the 2.0 kg payload test. The contraction ratio vs. pressure curves for upwards motions with each payload are plotted in Figure 5.8. The curves show that the contraction ratio depends nonlinearly on both the payload and pressure. In particular, with payloads of 5.3 kg or less, the contraction ratio can reach about 46%, while at higher payloads, the maximum contraction ratio decreases significantly.

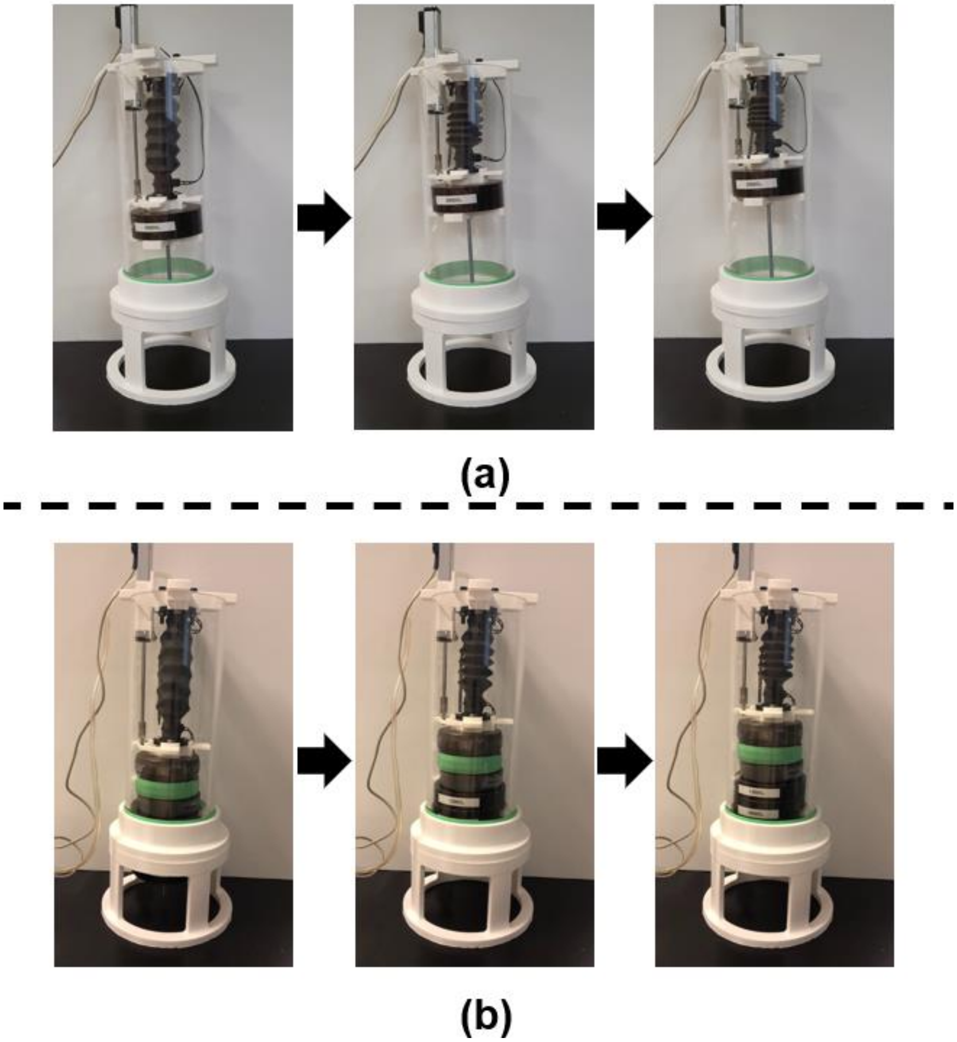

Figure 5.7 (a) Isotonic contraction of the accordion pattern OSPA with a payload of 2 kg. (b) Isotonic contraction with a payload of 8.6 kg.

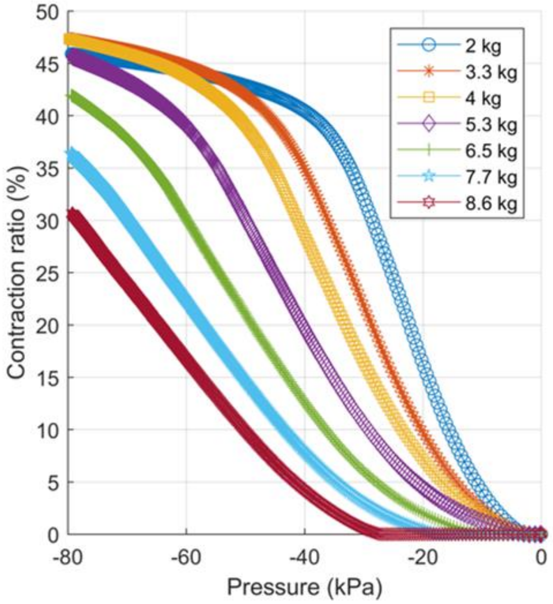

Figure 5.8. Isotonic contraction test results for the accordion pattern OSPA. (a) Contraction ratio vs. pressure for upwards motions with payloads of 2.0, 3.3, 4.0, 5.3, 6.5, 7.7 and 8.6 kg.

5.5 Hysteresis

To demonstrate the actuator's hysteresis, the contraction ratio vs. pressure curves are plotted for upwards and downwards motions in Figure. 14b. Maximum hysteresis values of 18.5%, 12.9% and 7.4% occurred with payloads of 2.0 kg, 5.3 kg and 8.6 kg, respectively. The first reason for the hysteresis is the stiffness of the heat shrink origami bellow. The second reason for hysteresis is the interaction between the origami bellow and the internal support ribs.

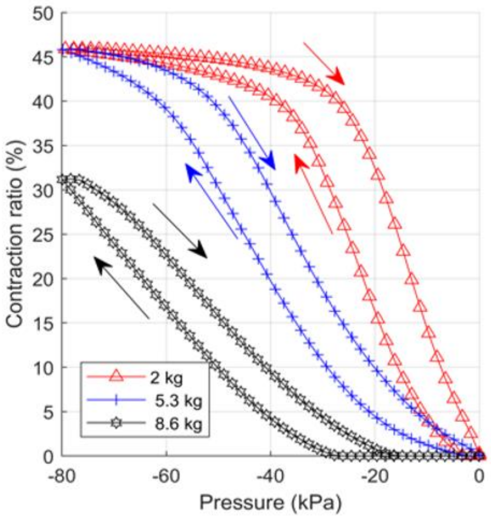

Figure 5.9 Contraction ratio vs. pressure for upwards and downwards motions with 2.0, 5.3 and 8.6 kg payloads, demonstrating the actuator's hysteresis.

5.6 Fatigue testing

Since in real applications an actuator must be able to perform its function repeatedly, a lengthy cyclic fatigue test was performed. For this test a 2 kg payload was used. A single cycle consisted of the OSPA raising and lowering this payload as the pressure was slowly decreased from -2 kPa to -75 kPa and then slowly increased back to -2 kPa. The test included 150,000 of these cycles and lasted for almost one month. The OSPA was visually inspected during and after the test ended, and no defects such as cracks or holes were observed. The pressure vs. time and displacement vs. time plots for the first five cycles and the last five cycles (i.e. cycles 149,996 to 150,000) are shown in Figures. 15a and 15b, respectively. These plots demonstrate that the OSPA's performance was consistent over this lengthy experiment, with the most noticeable differences occurring during the pressure and displacement transients.

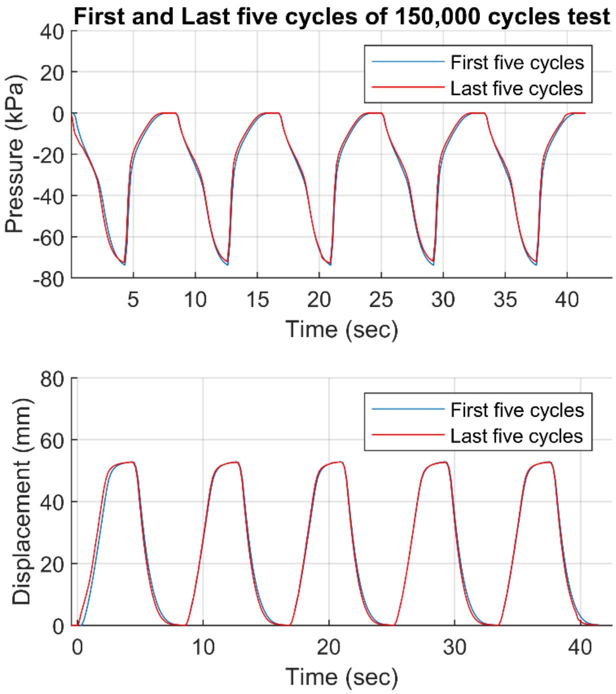

Figure 5.10 Results from the vertical cyclic fatigue test with 2 kg payload. Pressure and displacement vs. time for the first and last 5 cycles of the 150,000 cycles test.

5.7 Consistency testing

To evaluate the consistency of the fabrication method, the measurement setup and testing procedure presented in Section 5.1.1 was used to test a 2nd accordion pattern prototype. (The two prototypes are shown side by side in Figure 5.11). The blocked force vs. pressure results obtained for the 2nd prototype are plotted in Figure 5.12. Comparing Figures 5.4 and 5.12, the results for the two actuators are very similar except that the 2nd prototype produced slightly less force. The root-mean-square deviation between the force values is 3.3 N, and the maximum deviation is 4.8 N. This maximum deviation is 3.8% of the max blocked force at -80 kPa and zero displacement. This small difference may be due to minor leakage occurring with the second actuator.

Figure 5.11 The accordion pattern OSPA used for testing. Two fabricated prototypes.

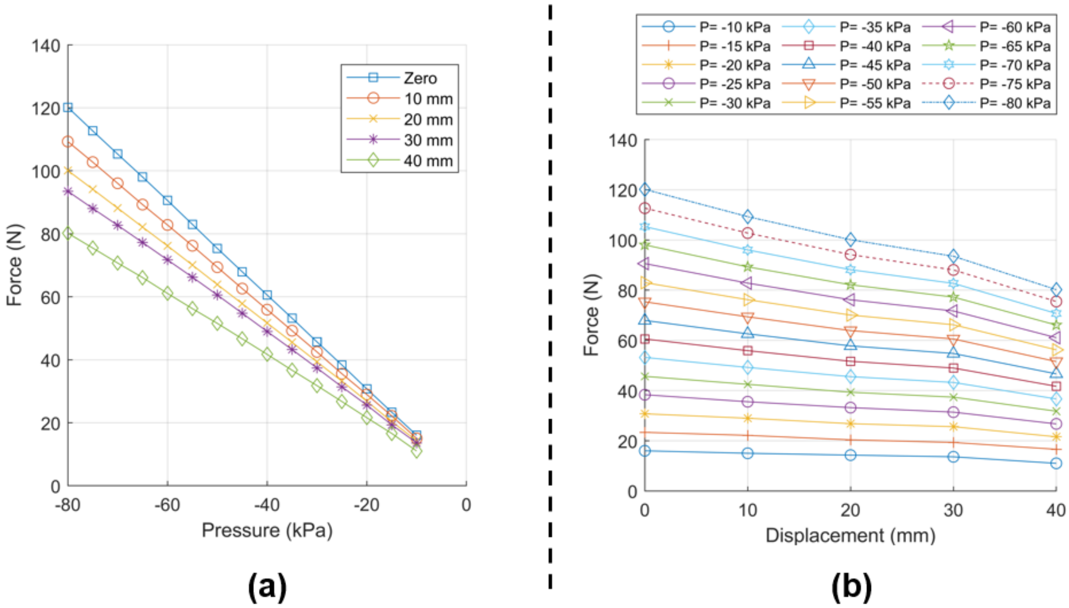

Figure 5.12. Blocked force vs. pressure results obtained from isometric tests performed with the 2nd prototype of the accordion pattern OSPA.

5.8 Scalability

One of the desirable characteristics of OSPA is the actuator can be scaled by scaling the panel parameters. So, scaling an OSPA for a specific application is straightforward. To illustrate the scalability of the accordion OSPA, we have fabricated several actuators using the method from Chapter 3. The fabricated actuators, as shown in Figure 5.13, have *D* values of 25.4 mm, 38.1 mm, 50.8 mm, 76.2 mm and 101.6 mm. The reason why these numbers were selected is the heat-shrink tubing (Qualtek, for example) is available in these standard diameters. The 101.6 mm actuator was fabricated from a heat-shrink tubing from another supplier (SUMITUBE® B2 (4X)) and has weight of 320 g. The vacuum source used with this actuator was the high flow vacuum pump (VN-C4, 12 V, 42 W, 85 kPa, 40L/min flowrate). The actuator can lift and hold payloads up to 44 kg, as illustrated in Figure 5.13. This confirms that the accordion pattern OSPA has a high force-to-weight ratio as it can lift a load more than 124 times its own weight.

Figure 5.13 Accordion pattern OSPAs scaled fabricated from different diameter heat-shrink tubing.

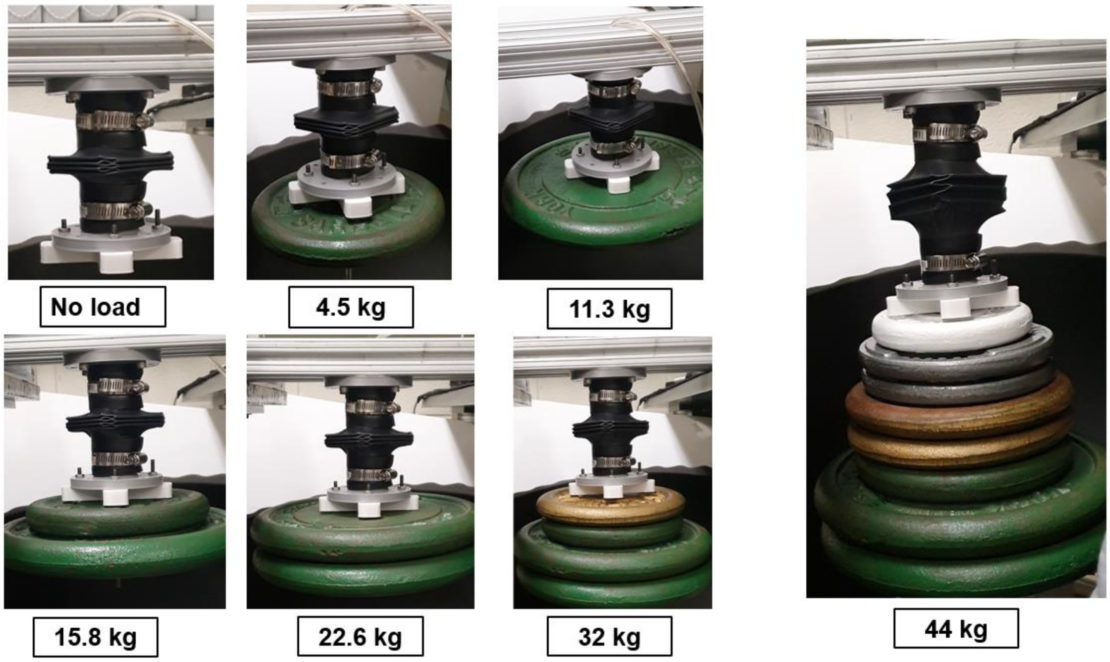

Figure 5.14 Testing the D = 101.6 mm accordion pattern OSPA lifting different payloads.

5.9 Comparison of the OSPA Prototypes with Related Pneumatic Actuators

To provide context for this research, a comparison study has been made between the OSPA prototypes and related pneumatic actuators. The results are listed in Table 5.1. The first two actuators are made by the company Festo. Their design is based on McKibben muscles and they are the only brand of soft pneumatic actuators sold commercially. Actuators 3-5 and 8 are the only OSPA in the literature that report fatigue test results. Actuators 6-8 are the OSPA prototypes designed and fabricated in this research. The comparison is based on eight performance metrics (occupied volume, mass, work, work to volume ratio, work to mass ratio, maximum force, maximum displacement, fatigue life) plus cost.

Fairness of the comparison was considered when choosing and calculating these metrics. The work is used in addition to the maximum force since it combines the force output and displacement into one metric. As long as the actuator produces enough work, a mechanism can be used to amplify its force and attenuate its displacement, or vice-versa, as required by the application. Regarding the operating pressures, it is well known that using a higher pressure will increase the force and work output of any pneumatic actuator. OSPA numbers 3 and 4 were tested at pressures of 10 kPa and 25 kPa, respectively. OSPA numbers 6-8 were tested at a pressure of -80 kPa. Actuators 1, 2 and 5 can operate at pressures with magnitudes larger than 80 kPa. To improve the fairness, the work and maximum force were determined at a pressure of 100 kPa with those actuators. Regarding the occupied volume, an actuator typically has components at both ends for mounting/attaching it. Those end pieces increase the actuator's occupied volume. Since actuators 3 and 4 did not use end pieces, the occupied volume was calculated for all actuators without the end pieces included. Lastly, the effective lengths of actuators 1 and 2 were chosen to match the effective lengths of actuators 6-8.

In terms of the performance metrics, actuator 1 takes up the least amount of space, but its work to volume (WTV) and work to mass (WTM) ratios are poor. Actuator 2 produces the largest maximum force, but its combination of large mass and small displacement place it close to the bottom in terms of WTV and WTM ratios. Actuator 3 is the lightest and has much better WTV and WTM ratios, but suffers from a very short fatigue life. Actuator 4 has the worst overall performance. Although actuator 5 produced the most work, it is significantly heavier than all of other actuators. Of the three OSPA prototypes created in this research (actuators 6-8), the smaller diameter of actuator 6 obviously reduced its occupied volume and mass, but its WTV and WTM ratios are the worst. The performance of the Yoshimura pattern OSPA (actuator 7) was intermediate. The larger accordion pattern OSPA (actuator 8) was significantly better than all of the other actuators in the OSPA category (i.e., actuators 3-8) in terms of WTV ratio, WTM ratio and maximum force. Regarding cost, actuators 1-2 are the most expensive. Actuator 2 costs 54 times more than the lowest cost actuator, actuator 6. In terms of fatigue life, actuators 1-2 are the best as they can last from 100,000 to 10 million cycles, as reported in [1]. However, it should be noted that actuator 8 has the longest service life of the OSPAs. Moreover, actuator 8 did not suffer from failure or leakage after the reported number of cycles. The fatigue experiment was stopped for due to time limitations and to increase the life of the vacuum pump. It can be concluded from this discussion that actuator 8 is the best overall performer.

Table 5.1 Comparison of the OSPA with related pneumatic actuators in terms of performance metrics and cost.

No.	Actuator Description	Occupied Volume (m^3)	Mass (kg)	Work* (J)	Work to Volume Ratio (J/m^3)	Work to Mass Ratio (J/kg)	Max. Force (N)	Max. Displacement (%)	Fatigue life (cycles)	Cost ($)
1	Festo fluidic muscle [30] DMSP-10-90N-RM-CM P = 100 kPa	2.83×10^{-5} [a]	0.067	0.063	2,210	0.94	84	2	>100,000	208.35
2	Festo fluidic muscle [30] DMSP-20-90N-RM-CM P = 100 kPa	11.3×10^{-5} [b]	0.185	0.619	5,480	3.35	295	6	>100,000	264.72
3	Extensor by Martinez et al. [1] P = 10 kPa	3.38×10^{-5} [c]	0.008	0.465	13,800	56.1	9.81 [d]	72.3	50	<10
4	Version B by Schmitt et al. [14] P = 25 kPa	4.48×10^{-5} [e]	0.025 [f]	0.164	3,660	6.71	40	32.7	30	unknown
5	Rotary actuator by Yi et al. [15] P = 100 kPa	43.4×10^{-5} [g]	0.300	12.2	28,100	40.6	18.5 Nm	33.3 [h]	10,000	unknown
6	Accordion OSPA (D = 36 mm) P = -80 kPa	4.61×10^{-5}	0.037	1.02	22,000	27.7	57.3	29.6	untested	4.88
7	Yoshimura OSPA (D = 50.8 mm) P = -80 kPa	9.88×10^{-5}	0.084	3.7	37,600	44.2	109	44.5	untested	7.95
8	Accordion OSPA [31] (D = 50.8) P = -80 kPa	10.9×10^{-5}	0.072	4.14	37,800	57.5	124	46.0	>150,000	7.84

*The work equals the area under the force vs. displacement curve at the specified pressure.

a. The occupied volume was calculated by multiplying the muscle's length of 90 mm by its maximum pressurized diameter of 20 mm [32].

b. The occupied volume was calculated by multiplying the muscle's length of 90 mm by its maximum pressurized diameter of 40 mm [32].

c. Due to the lack of information in [1], the shape was approximated a hexagonal prism with a side edge of 10 mm and a height of 130 mm based on Figure 5 in [1].

d. The maximum tested force was 9.81 N based on Figure 5 in [1]

e. The maximum volume was calculated using equation (3) and the values in Table I [14].

f. Due to the lack of information in [14], the mass was estimated from the two material's average densities multiplied by the estimated volume.

g. Due to the lack of information in [15], the volume was estimated as the volume of a hollow cylinder with the dimensions from Table I in [15] .

h. The percent maximum displacement was calculated by dividing the joint's range of motion by 2π .

5.10 Conclusions

An extensive series of tests have been performed on the OSPA prototypes using two custom-made measurement setups. These included isometric, isobaric, isotonic contraction, and cyclic fatigue tests. The blocked force, contraction ratio, service life, consistency and scalability have been characterized.

Two accordion pattern OSPA were fabricated using the same mold and materials to evaluate the proposed fabrication methods consistency. The root-mean-square deviation between the forces produced by those two prototypes was only 3.3 N which demonstrates their consistent performance. The scalability has been proven by fabricating actuators by fabricating and testing OSPA with *D* values ranging from 25.4 to 101.6 mm using heat-shrink tubing from two suppliers. The largest prototype lifted a 44 kg payload and has force-to-weight ratio a 124.

The test results allowed a detailed study comparing the OSPA prototypes to related pneumatic actuators to be completed. The study included eight actuators — two commercially available soft pneumatic actuators and all OSPA from the literature that reported fatigue test results. The comparison was based on eight performance metrics, plus cost. Although the 2nd commercially available actuator produced the largest force, its small displacement and relatively large mass caused it to have poor WTV and WTM ratios. The costs of those non-OSPA actuators were also found to be much larger than the OSPA. Of the six OSPA, the accordion pattern OSPA and Yoshimura pattern OSPA (both with D = 50.8 mm) ranked 1st and 2nd in terms of WTV ratio. The accordion OSPA also had the best WTM ratio, maximum force and durability. Its performance demonstrates that powerful, lightweight, and durable actuators can be easily produced by the proposed fabrication method. While it cannot match the durability of the commercial actuators, it withstood a lengthy cyclic fatigue test of 150,000 cycles under the effect of a 2 kg payload, which is a unique achievement compared to previous work and shows the potential of the new OSPA to be used in real-life applications.

Chapter 6. Design Optimization and Validation of Accordion OSPA

6.1 Introduction

The performance of the accordion OSPA can be altered by changing its geometric parameters defined Section 3.2.1. As shown in the previous chapter, FEA can be utilized to accurately model and simulate the accordion pattern OSPA. In this chapter, the developed FEA model will be used to optimize the parameters of the accordion pattern OSPA. The objective of the constrained optimization problem is to maximize the actuator's output work. The optimization process is explained in detail. Finally, the optimal design point is validated by fabricating and testing an actuator with the optimized geometric parameters.

6.2 Optimization Workflow

The optimization workflow follows these steps:

Step 1: The geometric design parameters are introduced by creating a parametric CAD model for the OSPA.

Step 2: The design parameters are imported into the FEA simulation software. This allows the CAD model to be automatically controlled by the FEA software.

Step 3: The lower and upper limits of each parameter are chosen as explained in Section 6.3. Then, a sufficient number of design points are generated using design of experiment (DOE) based on the combination of defined parameters. Finally, each individual design point is evaluated by running FEA to determine the corresponding output work.

Step 4: The response surface (RS) method is used to mathematically fit a model to the DOE points' calculated work values. This step is done to create a relationship between the design parameters and the work output.

Step 5: The chosen optimization algorithm looks for the optimum point on the generated response surface. The advantage of the RS method is that, unlike direct optimization methods, it does not need to run the FEA simulation many times.

Step 6: The optimum point generated by the optimization algorithm is verified by solving the FEA using the optimal design parameters.

The optimization tool chosen for this research is Ansys DesignXplorer (DX). Ansys DX is part of the integrated platform Ansys Workbench. This integration makes the optimization process more reliable, customizable and user-friendly since the external interactions of different engineering tools and external third-party codes for the optimization process are eliminated. In the remaining sections, each step of the workflow will be explained in detail.

6.3 Accordion Pattern Geometric Parameters and Constraints

A fully parametric CAD model for the accordion pattern OSPA has been developed in Autodesk Inventor based on the equations from Section 3.2.1 defining the accordion pattern's basic unit [33]. The CAD model's parameters are linked to all the parts of the accordion pattern OSPA (i.e., 3D accordion shape, support ribs, and end caps). The 3D CAD model is imported to the Ansys Design Modeler using the Autodesk Inventor plugin. When Ansys DX changes one or more parameters the CAD model is updated automatically.

The accordion pattern OSPA geometric parameters are the number of units, the accordion pattern's initial folding angle α, the actuator thickness t, the ratio between outer and inner diameter diameters $d_{ratio} = D/d$, and the actuator's diameter D. As shown in Section 5.8, increasing the actuator's diameter will increase its blocked force and therefore its work output. So, in the optimization problem D is kept fixed at 50.4 mm. Furthermore, doing this will facilitate the validation step as suitable heat-shrink tubing is readily available. OSPA with more units will require more FEA computational time compared to OSPA with fewer units since the mesh size increases with the number of units. With this in mind, an accordion pattern OSPA with three units is selected for the optimization process.

The geometric constraints were selected to avoid geometric modeling failures and non-converging simulations in FEA. The CAD model parameters considered in this optimization problem and their ranges are listed in Table 6.1. When d_{ratio} increases, the size of the actuator's panels increases. Under the effect of higher vacuum pressures, larger payloads, and larger initial folding angles, larger panels tend to bend instead of folding at the hinges, which causes convergence problems with FEA. An example of this is given in Figure 6.2. To avoid this failure the upper bound on d_{ratio} was set to 2.4. When the initial folding angle and the payload are large, the internal support ribs tend to slip from their original locations at the accordion pattern's internal valleys. If this happens the actuator will fail to fold, and the FEA simulations will not converge. This problem was avoided by setting the upper bound on α to 110º.

Table 6.1 The selected 3D CAD parameters of the accordion actuator and their ranges.

No.	Parameter name	Parameter type	symbol	Lower Bound	Upper Bound
1	Diameter ratio	Continuous	d_{ratio}	1.8	2.4
2	Initial folding angle	Continuous	α	70º	110º
3	Thickness	Continuous	t	0.7 mm	1.7mm

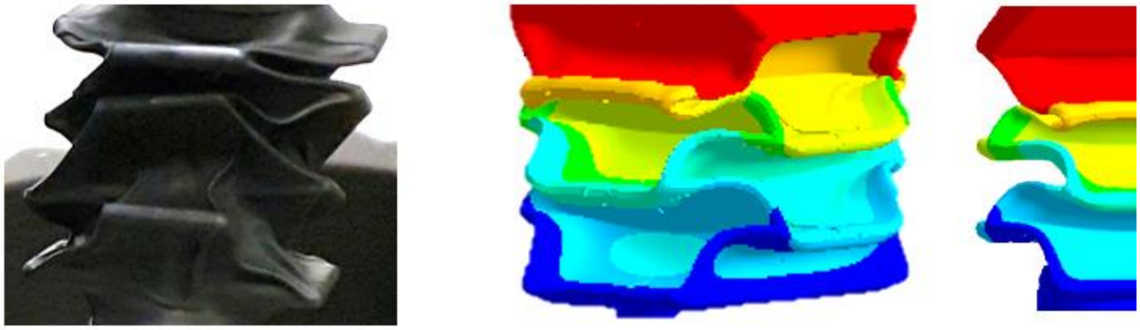

(a) (b)

Figure 6.1 The effect of increasing the d_{ratio} value beyond 2.4. (a) Actual actuator with $d_{ratio} > 2.4$. (b) FEA simulation for the same case.

6.4 Two-part FEA Simulation Procedure

To find the optimal design parameters for the OSPA, a procedure involving two FEA simulations has been developed. In the 1st FEA simulation, the maximum blocked force (i.e., the blocked force at zero contraction) is predicted for a vacuum pressure of -80 kPa at each of the design points generated by the DOE technique. Note that a design point is defined as: $X = [\alpha, d_{ratio}, t]$. The 2nd FEA simulation predicts the maximum stroke at each of those design points t for a vacuum pressure of -80 kPa and 75% of the maximum blocked force from the first simulation applied as a load. The work done by the actuator is calculated by multiplying the 75% of blocked force by the maximum stroke of the actuator. This scenario was created to achieve a fair comparison between different designs. The FEA workflow is illustrated in Figure 6.3.

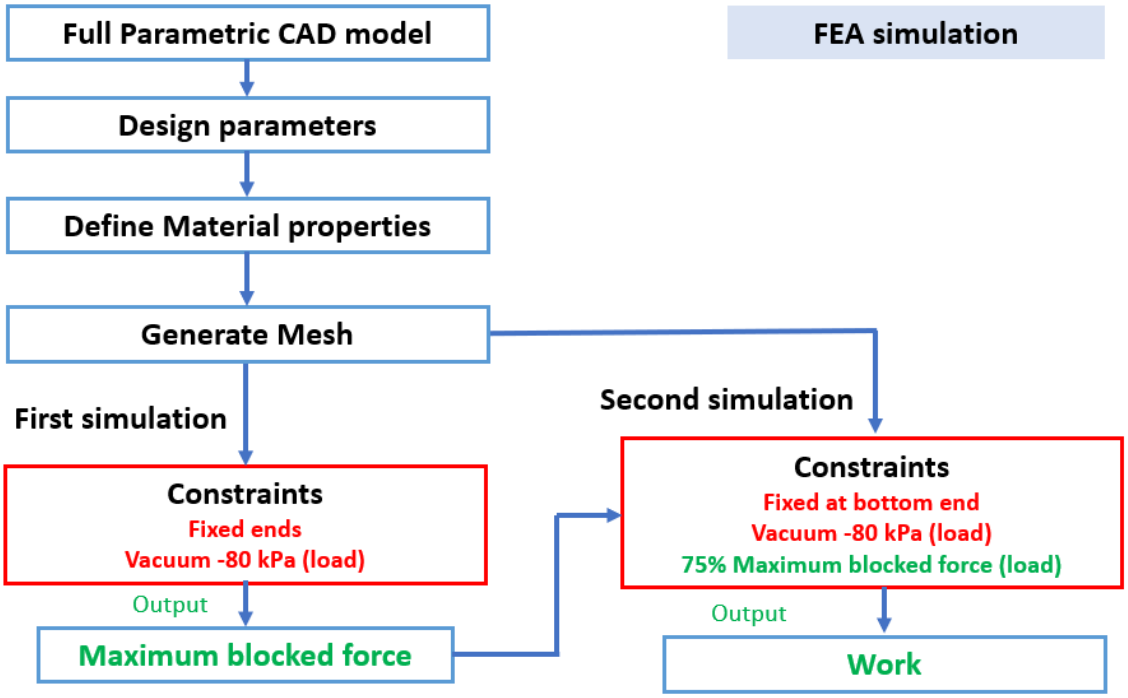

Figure 6.2 Two-part FEA workflow.

6.5 Optimization

6.5.1 Optimization problem definition

The optimization objective is to maximize the accordion pattern OSPA's work output (W) by selecting its optimum geometric parameters. W is evaluated by multiplying the blocked force by the actuator's maximum stroke in the second FEA simulation. The constraints of the optimization problem correspond to the geometric constraints of the accordion OSPA. Furthermore, limiting the value of the von Mises strain ($\varepsilon_{vonMises}$) was included as a constraint to follow the FEA software's recommendation that the hyperelastic material model should only be used in the range of the imported test data [28]. The constrained optimization problem can then be formulated as follows:

$$X_{opt} = \underset{X}{\arg\max}\, W$$

$$W = \int_0^{y_{out}} \overrightarrow{F_{out}} . \overrightarrow{dy} \tag{6.1}$$

$$X = [\alpha, d_{ratio}, t]$$

Subject to:

$$70° \le \alpha \le 110° \qquad 0.7 \text{ mm} \le t \le 1.7 \text{ mm}$$

$$1.8 \le d_{ratio} \le 2.4 \qquad \varepsilon_{vonMises} \le 0.5$$

6.5.2 Optimization details

The following features of Ansys DX were used for the optimization process. DOE is a technique used to scientifically determine the set of design points [34]. There is a wide range of DOE techniques in the literature. They all have one common characteristic: they try to locate the sampling points such that the space of random input parameters is explored in the most efficient way. In other words, they try to obtain the required information with the minimum number of sampling points. Placing the points in efficient locations will not only reduce the required number of points, but also increase the accuracy of the response surface that is derived from the results at those sampling points. The Latin hypercube sampling (LHS) DOE method was selected since it is an advanced form of Monte Carlo sampling that avoids clustering samples. In an LHS design, no point shares a row or column of the design space with any other point [34]. The main advantage of this method that it saves computation time by avoiding the creation of duplicate points. The LHS created the 15 points listed in Table 6.2. The output work values and maximum von Mises strain for each of these points (predicted by the FEA simulation procedure described in Section 6.4) are also listed in this table. The values in the last column are ¼ of the output work due to the quarter symmetry model used with the FEA simulation.

The accuracy of a RS depends on several factors: the complexity of the variations of the output (in this research the work done by the actuator), number of sampling points, and the chosen RS method. The Kriging method was selected for obtaining the RS since it is known to provide an improved response quality and fit higher-order variations of the output parameter [34][35].

Using the post-processing tools available in Ansys DX, the effects of the geometric parameters d_{ratio}, α and t on the work output are illustrated in Figures 6.4 - 6.6. Figure 6.4 shows there is a negative correlation between t and W. This occurred since increasing t increases the actuator's stiffness which then increases the amount of pneumatic energy required to fold the hinges. Figure 6.5 shows there is a positive correlation between d_{ratio} and W. The reason is a larger d_{ratio} increases the areas of the panels and this increased the output force. Finally, there is a nonlinear relationship between the initial folding angle, α, and W. The nonlinearity comes from the nonlinear relationship between α and the actuator's maximum stroke. The maximum stroke has a positive correlation for α values up to about 98° since the angles are small enough to allow folding of the accordion pattern without significantly bending the panels. In contrast, a negative correlation occurs for α values over about 98° since the larger angles cause the flexible panels to bend instead of folding.

An optimization algorithm is used to find the optimum point on the RS. Several optimization algorithms are included in Ansys DX. A multi-objective genetic algorithm (MOGA) is an iterative method that can optimize problems with continuous input parameters. It was chosen as the optimization algorithm due to its improved efficiency for global optimum search compared to gradient-based algorithms [36].

Table 6.2 Design points generated by the LHS DOE and the corresponding maximum strain and ¼ work values computed by the FEA simulation procedure.

Design Point No.	**Parameter 1** α (º)	**Parameter 2** d_{ratio}	**Parameter 3** t (mm)	**Max. strain** $\max\left(\varepsilon_{vonMises}\right)$	**¼ Work** $\frac{1}{4}W$ (J)
1	92.6	2.26	1.27	0.37	0.50
2	100.6	2.10	1.33	0.33	0.30
3	71.3	2.14	0.87	0.34	0.41
4	98	1.82	1.60	0.22	0.08
5	74	1.90	0.93	0.37	0.28
6	108.6	1.86	0.80	0.49	0.44
7	95.3	2.34	1.53	0.30	0.32
8	106	2.22	1.47	0.30	0.27
9	82	1.94	1.20	0.35	0.27
10	79.3	2.18	1.67	0.25	0.22
11	87.3	2.02	1.07	0.40	0.42
12	76.6	2.30	1.00	0.36	0.53
13	90	2.06	1.13	0.40	0.44
14	103.3	2.38	0.73	0.46	0.80
15	84.6	1.98	1.40	0.28	0.21

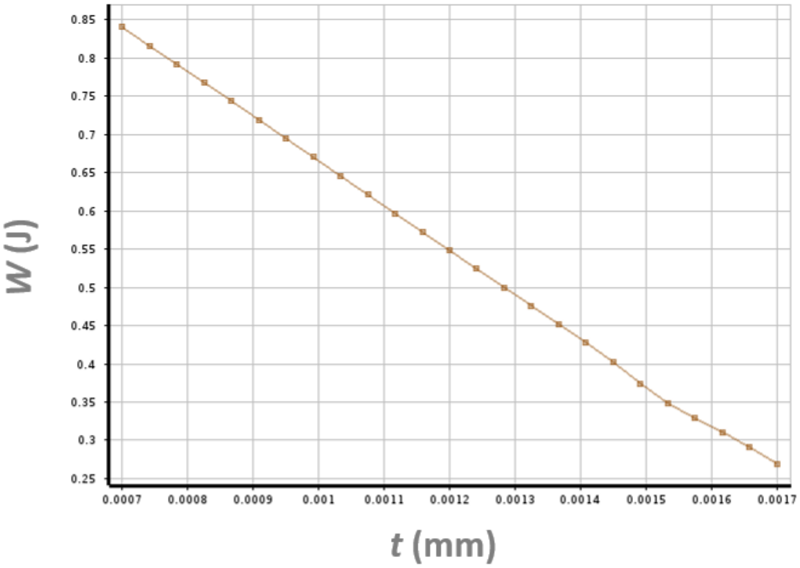

Figure 6.3 The effect of varying the actuator thickness on the output work while the other variables are fixed at the optimum point. Note: The vertical axis shows ¼ of the work due to the quarter symmetry model used with the FEA.

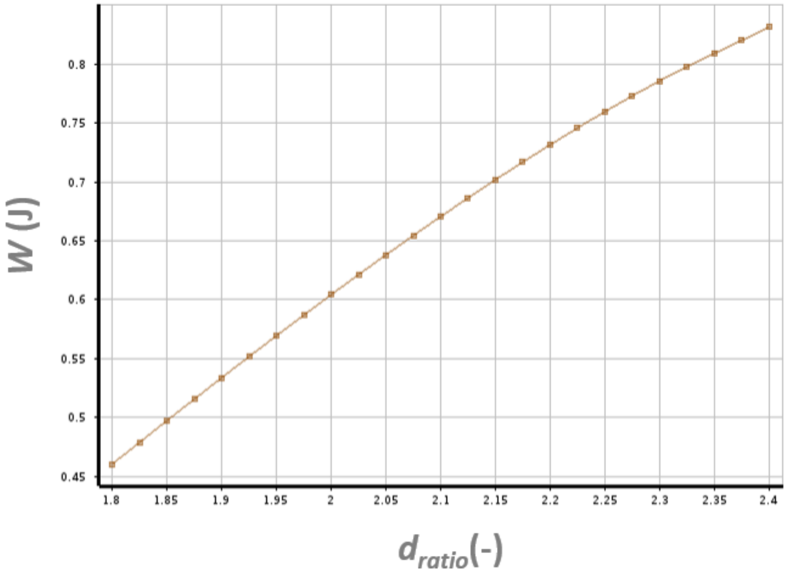

Figure 6.4 The effect of varying the actuator diameter ratio on the output work while the other variables are fixed at the optimum point. Note: The vertical axis shows ¼ of the work due to the quarter symmetry model used with the FEA.

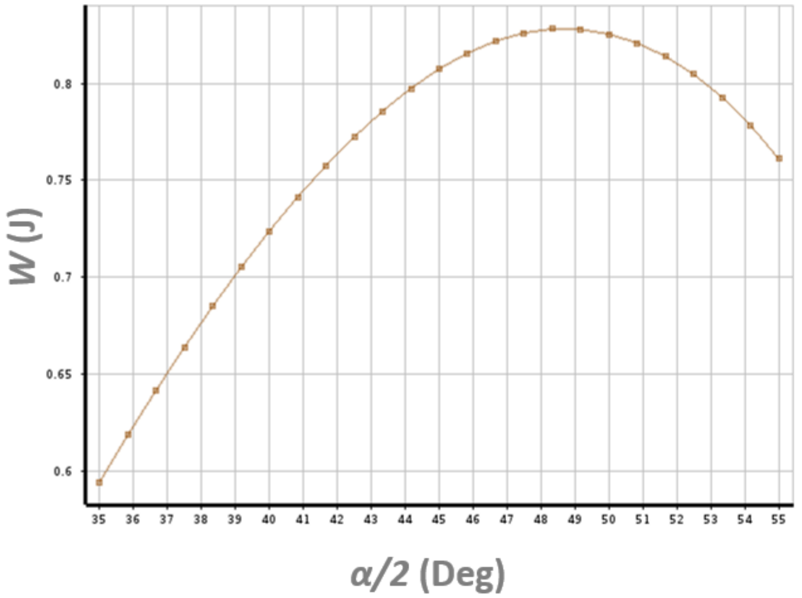

Figure 6.5 The effect of varying actuator folding angle on the output work while the other variables are fixed at the optimum point. Note: The vertical axis shows ¼ of the work due to the quarter symmetry model used with the FEA.

6.6 Optimization Result Verification and Validation

The geometric parameters at the optimum design point X_{opt} were $\alpha = 96°$, $d_{ratio} = 2.39$, $t = 0.842$ mm. The optimum value of the work equaled 3.36 J. On a Windows 10 laptop with a 2.6 GHz, 6 core, Intel i7 CPU and 16 GB RAM, the total computation time for the optimization process was about 300 minutes. To check the RS, the optimum point was verified by running the FEA simulation procedure of an OSPA with $X = X_{opt}$. The difference between the RS point and the work at Xopt was only 1.1%, which demonstrates the accuracy of the RS.

As mentioned in Section 2.5, validation of the optimization result(s) for an OSPA has not been reported in the prior literature. In this research, two three-unit accordion pattern OSPAs were fabricated to validate the optimum design point.

The 1st OSPA was fabricated with the non-optimized parameters from Section 3.4. The 2nd OSPA was fabricated with the optimum geometric parameters $\alpha = 96°$ and $d_{ratio} = 2.39$. Unfortunately, setting t to a specific value such as 0.842 m is not possible with the proposed fabrication method. The isotonic test setup explained in Section 5.4 of this work was utilized to test both actuators under the effect of a 10 kg payload. The test was repeated five times using a vacuum of -80 kPa. The output work values for the two OSPA were calculated by multiplying the average value of the actuator's stroke by the 98.1 N payload weight. Moreover, simulations for both optimized and non-optimized accordion OSPAs have been completed with a 10 kg payload.

The results are presented in Table 6.3. The simulation results indicate that the work from the optimized actuator has been improved by 55%, while the experimental tests show an improvement of 53%. While the improvement percentages are very similar, the values of the predicted stroke and work are much larger than the experimental values. The reasons for the differences include the approximate value used for the actuator’s wall thickness, the assumption of uniform wall thickness, and errors in the simulated actuator’s stiffness caused by errors in the material models and the friction forces between the internal support ribs and the actuator’s walls.

In addition, the blocked forces for both actuators were experimentally tested using the isometric and isobaric test setup described in Section 5.2. The blocked force of the actuator has been increased from 117 N for the non-optimized actuator to 134 N for the optimized actuator. These results further demonstrate how the developed optimization process improved the performance of the three-unit accordion pattern OSPA.

Table 6.3 Output work values generated from FEA simulation and experimental testing of the three-unit accordion pattern OSPAs.

Actuator	Payload (kg)	Stroke (mm)	Work (J)
Optimum actuator - FEA	10	31	3.0
Non-optimum actuator - FEA	10	20	2.0
Optimum actuator - Exp.	10	27	2.6
Non-optimum actuator - Exp.	10	17	1.7

6.7 Conclusions

An efficient and effective model-based design optimization workflow has been developed for OSPA fabricated by the method proposed in Chapter 3. The optimization objective is to find the design point that maximizes the OSPA's output work, where the design point consists of the parameters α, d_{ratio} and t. The workflow's efficiency comes from its use of DOE to explore the input space with a small number of points, fitting a RS to those points by Kriging and finding the optimum design point on the RS using the MOGA algorithm. A parametric CAD model and a two-part FEA simulation procedure are used to predict the OSPA's output work under isotonic conditions. The workflow was implemented for the accordion pattern OSPA using Ansys Workbench. Running on a common laptop, the total computation time to obtain the optimum design point was about 300 minutes.

As mentioned in Section 2.5, validation of the optimization result(s) for an OSPA has not been reported in the prior literature. In this chapter, experiments on two accordion OSPA prototypes were used to validate the optimum design point. Although the experimentally measured work values were much smaller than the FEA predictions, the improvement percentages of the optimized design relative to the non-optimal one were similar. The simulation results predicted that the work from the optimized actuator would be improved by 55%, while the experimental tests showed an improvement of 53%.

Chapter 7. Conclusions

7.1 Summary

In this thesis, the design, fabrication, modeling, and optimization of OSPA were investigated. A novel fabrication method of OSPA was presented to address the limitations of the existing fabrication methods. The proposed method can fabricate an actuator in minutes by thermally forming commonly available heat-shrink tubing to a 3D printed reusable multi-piece mold. Accordion pattern and Yoshimura pattern OSPAs have been fabricated by the proposed method. It was also used to create a soft-ended actuator. Moreover, a modified fabrication method for creating small-diameter actuators was proposed and demonstrated.

An FEA model for the accordion pattern OSPA was developed to predict the actuator's folding behavior and blocked force. A detailed CAD model of the accordion pattern OSPA was utilized. The mechanical behavior of the OSPA's heat-shrink material was modeled through tensile testing. The model's accuracy for predicting the folding behaviour and blocked force was validated through experimental testing.

To evaluate the performance of the OSPA prototypes and allow comparisons with existing soft pneumatic actuators, a series of isometric, isobaric, and isotonic contraction tests were performed to evaluate the blocked forces and contraction ratio vs. pressure. The contraction ratio decreased with the increase of the payload. The measurements illustrated that the contraction ratio depends nonlinearly on both the payload and pressure. The consistency of the fabricated prototypes and the fabrication method's scalability were also investigated. The tested actuators' performance demonstrates that powerful, lightweight, and durable actuators can be easily developed by the proposed fabrication method.

The performance of the accordion OSPA can be altered by changing its geometric parameters. A FEA model based on a fully parametric CAD model was used to optimize the accordion pattern OSPA. The objective of the constrained optimization problem was to maximize the actuator's output work. DOE, RS and MOGA were used to find the optimal design point of the OSPA. A two-part FEA simulation procedure was developed to predict the OSPA’s output work under isotonic conditions. The workflow was implemented using Ansys Workbench. The optimal design point was validated by fabricating and testing an actuator with the optimized geometric parameters.

7.2 Achievements

The achievements of this research can be summarized as follows:

1. A subset of the design, modelling and fabrication research has been published in an IEEE journal paper [31].
2. The proposed fabrication method is more systematic and faster than existing OSPA fabrication methods. The fabrication time is less than 10 min excluding the 3D printing time. The fabrication method does not require specialized equipment and can be used to fabricate actuators based on a wide range of origami patterns (including actuator designs that cannot be produced by folding).
3. OSPA prototypes based on the accordion and Yoshimura patterns have been fabricated successfully with a range of diameters. The prototypes can produce pushing forces by applying positive internal pressure or pulling forces by utilizing a vacuum pump.
4. To address the fabrication method's limited ability to produce small diameter actuators, a modified fabrication method is proposed that replaces the reusable mold with a dissolvable PVA mold.
5. Actuators with soft-ends can be fabricated by the proposed method.

6. A detailed non-linear FEA model of the accordion pattern OSPA was developed to predict the performance of the accordion pattern OSPA, including the folding behavior and blocked force when either vacuum or positive pressure is used. The non-linear behavior of the polyolefin heat shrink was captured through a Mooney-Rivlin two-parameter hyperelastic material model. The symmetry of the accordion pattern was exploited to reduce the size of the FEA problem by 75%, saving significant computation time. The developed model was validated experimentally. The maximum deviation between the blocked force simulation results and experimental measurements was 5.7%, which demonstrates the accuracy of the developed model.
7. An extensive series of tests have been performed to evaluate the performance of the OSPA prototypes using two custom-made measurement setups. These included isometric, isobaric, isotonic contraction, and cyclic fatigue tests. The blocked force, contraction ratio, service life, consistency, and scalability have been characterized.
8. The OSPA prototypes have better durability than existing OSPA. An accordion pattern OSPA could withstand a lengthy cyclic fatigue test of 150,000 cycles under the effect of a 2 kg payload, which is a unique achievement compared to previous work.
9. The proposed fabrication method can be used to fabricate an actuator with consistent performance. The root-mean-square deviation between the force values of the two tested accordion pattern OSPA was 3.3 N.
10. The fabrication method’s scalability has been proven by fabricating accordion pattern OSPAs with diameters ranging from 25.4 to 101.6 mm. The 101.6 mm diameter OSPA lifted a 44 kg payload and has a force-to-weight ratio of 124.
11. A detailed study comparing the OSPA prototypes to related pneumatic actuators to be completed. The study included eight actuators — two

commercially available soft pneumatic actuators and all OSPA from the literature that reported fatigue test results. The comparison was based on eight performance metrics, plus cost. Although the 2nd commercially available actuator produced the largest force, its small displacement and relatively large mass caused it to have poor WTV and WTM ratios. The costs of those non-OSPA actuators were also found to be much larger than the OSPA. Of the six OSPA, the accordion pattern OSPA and Yoshimura pattern OSPA (both with D = 50.8 mm) ranked 1st and 2nd in terms of WTV ratio. The accordion OSPA also had the best WTM ratio, maximum force, and durability. The comparison results show the OSPA's potential to be used in real-life applications.

12. An efficient and effective model-based design optimization workflow has been developed for OSPA fabricated by the proposed method. The optimization objective is to find the design point that maximizes the OSPA’s output work. The workflow’s efficiency comes from its use of DOE to explore the input space with a small number of points, fitting a RS to those points and finding the optimum design point on the RS using the MOGA algorithm. Running on a common laptop, the total computation time to obtain the optimum design point was about 300 minutes.
13. Validation of the optimization result(s) for an OSPA has not been reported in the prior literature. In this thesis, experiments on two accordion OSPA prototypes were used to validate the optimum design point. The blocked force of the optimized accordion pattern OSPA increased by 15%. Although the experimentally measured work values were much smaller than the FEA predictions, the improvement percentages of the optimized design relative to the non-optimal one were similar. The simulation results predicted that the output work of the optimized actuator would be improved by 55%, while the experimental tests showed an improvement of 53%.

7.3 Actuator limitations

The primary limitations of the proposed OSPAs are:

1. The proposed OSPAs can not be used with high-temperature applications (greater than 100°) due to the polyolefin heat shrink's material characteristics and the softening temperature of the ABS end caps.
2. Using vacuum as the source of power limits the output blocked force of the actuator, as the maximum ideal vacuum is only 100 kPa and the output force is directly proportional to the pressure value.
3. There is a limitation on the minimum diameter of the actuators that can be fabricated by the proposed method. When the diameter of the actuator decreases, heat shrink with a thinner wall thickness will need to be used for the hinges to fold properly. However, using thinner heat shrink will weaken the actuator, so smaller pressures will have to used, and smaller blocked forces will be produced.
4. The actuator’s wall thickness is variable because of the nature of the heat shrinking process. Measuring this thickness variation without destroying the actuator is very difficult with current measurement technology. The inability to measure this variation limits the accuracy of any OSPA model.

7.4 Recommendations for future work

- Improving the accuracy of the hyperplastic material model of the polyolefin heat-shrink by performing biaxial and planar tests; and studying its effect on the FEA simulation results.
- Fabricate and test OSPAs based on other origami patterns like the Kresling pattern and the Miura-ori pattern to compare the performance of different patterns OSPAs. The main challenge is generating the 3D CAD model of

these complex origami patterns.

- Taking advantage of other origami patterns to design OSPA that can directly provide rotary motion.
- Modifying the top end cap transition section's design as this transition section reduces the actuator's range of motion.
- Investigating alternate designs and materials for the internal support ribs. The ribs used in our prototypes allowed them to operate at higher vacuum pressures and produce larger forces, but they also reduced the prototypes' range of motion. If these ribs can be made thinner, without sacrificing strength, then equally strong OSPA with larger contraction ratios can be produced using our fabrication method.
- Reducing the fabrication time of the modified fabrication method based on the dissolvable mold. This can be achieved by altering the design of the end caps to reduce the dissolving time of the mold.
- Applying different control techniques to the proposed accordion pattern OSPA.
- Create an extension type actuator by switching to a positive pressure supply. This will have the advantage of overcoming the vacuum pressure limit, but the potential for failure by buckling will have to be considered in the actuator’s design.
- Fabricating and testing a pair of actuators connected by a cable to a pulley in an agonist-antagonist arrangement to produce a bidirectional rotary actuator.

References

[1] R. V. Martinez, C. R. Fish, X. Chen, and G. M. Whitesides, “Elastomeric origami: Programmable paper-elastomer composites as pneumatic actuators,” *Adv. Funct. Mater.*, vol. 22, no. 7, pp. 1376–1384, 2012, doi: 10.1002/adfm.201102978.

[2] Q. Qiao, J. Yuan, Y. Shi, X. Ning, and F. Wang, “Structure, design, and modeling of an origami-inspired pneumatic solar tracking system for the NPU-phonesat,” *J. Mech. Robot.*, vol. 9, no. 1, p. 011004, 2017, doi: 10.1115/1.4035086.

[3] H. Sane, P. Bhovad, and S. Li, “Actuation performance of fluidic origami cellular structure: A holistic investigation,” *Smart Mater. Struct.*, vol. 27, no. 11, p. 115014, 2018, doi: 10.1088/1361-665X/aadfac.

[4] M. Yu, W. Yang, Y. Yu, X. Cheng, and Z. Jiao, “A Crawling Soft Robot Driven by Pneumatic Foldable Actuators Based on Miura-Ori,” *Actuators*, vol. 9, no. 2, p. 26, 2020, doi: 10.3390/act9020026.

[5] M. Schenk, A. D. Viquerat, K. A. Seffen, and S. D. Guest, “Review of inflatable booms for deployable space structures: Packing and rigidization,” *J. Spacecr. Rockets*, vol. 51, no. 3, pp. 762–778, 2014, doi: 10.2514/1.A32598.

[6] J. Butler *et al.*, “Highly compressible origami bellows for harsh environments,” *Proceedings of the ASME Design Engineering Technical Conference*, vol. 5B-2016. Aug. 21, 2016, doi: 10.1115/DETC2016-59060.

[7] M. Schenk, S. G. Kerr, A. M. Smyth, and S. D. Guest, “Inflatable Cylinders for Deployable Space Structures,” *First Conf. Transform. 2013*, no. September, pp. 1–6, 2013, [Online]. Available: http://www.markschenk.com/research/files/schenk2013-

Transformables.pdf.

[8] M. Schenk, A. D. Viquerat, K. A. Seffen, and S. D. Guest, “Review of inflatable booms for deployable space structures: Packing and rigidization,” *J. Spacecr. Rockets*, vol. 51, no. 3, pp. 762–778, 2014, doi: 10.2514/1.A32598.

[9] S. Liu, W. Lv, Y. Chen, and G. Lu, “Deployable prismatic structures with rigid origami patterns,” *J. Mech. Robot.*, vol. 8, no. 3, pp. 1–11, 2016, doi: 10.1115/1.4031953.

[10] L. Paez, G. Agarwal, and J. Paik, “Design and Analysis of a Soft Pneumatic Actuator with Origami Shell Reinforcement,” *Soft Robot.*, vol. 3, no. 3, pp. 109–119, 2016, doi: 10.1089/soro.2016.0023.

[11] J. G. Lee and H. Rodrigue, “Origami-Based Vacuum Pneumatic Artificial Muscles with Large Contraction Ratios,” *Soft Robot.*, vol. 6, no. 1, pp. 109–117, 2019, doi: 10.1089/soro.2018.0063.

[12] S. Li, D. M. Vogt, D. Rus, and R. J. Wood, “Fluid-driven origami-inspired artificial muscles,” *Proc. Natl. Acad. Sci.*, p. 201713450, 2017, doi: 10.1073/pnas.1713450114.

[13] M. Schenk, J. M. Allwood, and S. D. Guest, “Cold Gas-Pressure Folding of Miura-ori Sheets Cold Gas-Pressure Folding Process,” 2011, pp. 1–6.

[14] F. Schmitt, O. Piccin, L. Barbe, and B. Bayle, “An Origami-Inspired Flexible Pneumatic Actuator,” *IEEE Int. Conf. Intell. Robot. Syst.*, pp. 436–441, 2018, doi: 10.1109/IROS.2018.8593423.

[15] J. Yi *et al.*, “Customizable Three-Dimensional-Printed Origami Soft Robotic Joint with Effective Behavior Shaping for Safe Interactions,” *IEEE Trans. Robot.*, vol. 35, no. 1, pp. 114–123, 2019, doi: 10.1109/TRO.2018.2871440.

[16] C. Tawk, G. M. Spinks, M. In Het Panhuis, and G. Alici, “3D Printable Linear Soft Vacuum Actuators: Their Modeling, Performance Quantification and Application in Soft Robotic Systems,” *IEEE/ASME Trans. Mechatronics*, vol. 24, no. 5, pp. 2118–2129, 2019, doi: 10.1109/TMECH.2019.2933027.

[17] E. T. Filipov, K. Liu, T. Tachi, M. Schenk, and G. H. Paulino, “Bar and hinge models for scalable analysis of origami,” *Int. J. Solids Struct.*, vol. 124, pp. 26–45, 2017, doi: 10.1016/j.ijsolstr.2017.05.028.

[18] S. Li and K. W. Wang, “Fluidic origami: A plant-inspired adaptive structure with shape morphing and stiffness tuning,” *Smart Mater. Struct.*, vol. 24, no. 10, p. 105031, 2015, doi: 10.1088/0964-1726/24/10/105031.

[19] P. Boyraz, G. Runge, and A. Raatz, “An overview of novel actuators for soft robotics,” *High-Throughput*, vol. 7, no. 3, pp. 1–21, 2018, doi: 10.3390/act7030048.

[20] P. Moseley, J. M. Florez, H. A. Sonar, G. Agarwal, W. Curtin, and J. Paik, “Modeling, Design, and Development of Soft Pneumatic Actuators with Finite Element Method,” *Adv. Eng. Mater.*, vol. 18, no. 6, pp. 978–988, 2016, doi: 10.1002/adem.201500503.

[21] G. Runge, J. Peters, and A. Raatz, “Design optimization of soft pneumatic actuators using genetic algorithms,” *2017 IEEE Int. Conf. Robot. Biomimetics, ROBIO 2017*, vol. 2018-Janua, pp. 393–400, 2018, doi: 10.1109/ROBIO.2017.8324449.

[22] G. Dämmer, S. Gablenz, A. Hildebrandt, and Z. Major, “PolyJet-printed bellows actuators: Design, structural optimization, and experimental investigation,” *Front. Robot. AI*, vol. 6, no. MAY, pp. 1–10, 2019, doi: 10.3389/frobt.2019.00034.

[23] P. Polygerinos, Z. Wang, K. C. Galloway, R. J. Wood, and C. J. Walsh, “Soft robotic glove for combined assistance and at-home rehabilitation,” *Rob. Auton. Syst.*, vol. 73, pp. 135–143, 2015, doi: 10.1016/j.robot.2014.08.014.

[24] I. De Falco, M. Cianchetti, and A. Menciassi, “A soft multi-module manipulator with variable stiffness for minimally invasive surgery.,” *Bioinspir. Biomim.*, vol. 12, no. 5, p. 056008, Sep. 2017, doi: 10.1088/1748-3190/aa7ccd.

[25] Z. Zhang, X. Wang, S. Wang, D. Meng, and B. Liang, “Design and modeling of a parallel-pipe-crawling pneumatic soft robot,” *IEEE Access*, vol. 7, pp. 134301–134317, 2019, doi: 10.1109/ACCESS.2019.2941502.

[26] C. B. Manufacturing, C. R. Specimens, and T. Determina-, “Standard Test Methods for Vulcanized Rubber and Thermoplastic Elastomers —,” pp. 1–14, 2009, doi: 10.1520/D0412-16.2.

[27] “Ansys Innovation Courses: Hyperelasticity.” https://qualtekusa.com/wp-content/uploads/specsheets/Q2F4X.pdf (accessed Jan. 28, 2021).

[28] “Q2-F4X high shrink ratio, highly flexible flame retardant polyolefin tubing shrink ratio 4:1.” https://courses.ansys.com/index.php/courses/hyperelasticity/ (accessed Jan. 29, 2021).

[29] E. Wang, “Thin-wall structure simulation.” https://support.ansys.com/staticassets/ANSYS/staticassets/resourcelibrary/confpaper/2006-Int-ANSYS-Conf-22.pdf.

[30] “DMSP/MAS, Fluidic Muscle.” https://www.festo.com/rep/en_corp/assets/pdf/info_501_en.pdf (accessed Oct. 15, 2020).

[31] A. Zaghloul and G. M. Bone, “3D Shrinking for Rapid Fabrication of Origami-Inspired Semi-Soft Pneumatic Actuators,” *IEEE Access*, vol. 8, pp. 191330–191340, 2020, doi: 10.1109/access.2020.3032131.

[32] D. Villegas, M. Van Damme, B. Vanderborght, P. Beyl, and D. Lefeber, “Third-generation pleated pneumatic artificial muscles for robotic applications: Development and comparison with Mckibben muscle,” *Adv. Robot.*, 2012, doi: 10.1080/01691864.2012.689722.

[33] J. Butler *et al.*, “Highly compressible origami bellows for harsh environments,” *Proc. ASME Des. Eng. Tech. Conf.*, vol. 5B-2016, p. V05BT07A001, 2016, doi: 10.1115/DETC2016-59060.

[34] E. Tyflopoulos and M. Steinert, “Topology and parametric optimization-based design processes for lightweight structures,” *Appl. Sci.*, vol. 10, no. 13, 2020, doi: 10.3390/app10134496.

[35] M. A. Moghimi, K. J. Craig, and J. P. Meyer, “Optimization of a trapezoidal cavity absorber for the Linear Fresnel Reflector,” *Sol. Energy*, vol. 119, pp. 343–361, 2015, doi: 10.1016/j.solener.2015.07.009.

[36] “Ansys® Academic Research Mechanical, Release 2021.R1, Help System, DesignXplorer User’s Guide, ANSYS, Inc.” .